TKK-Institute of Photogrammetry and Remote Sensing
Publications

1/2005

Espoo 2005

# THE CIRCULAR IMAGING BLOCK IN CLOSE-RANGE PHOTOGRAMMETRY

Jussi Heikkinen

Dissertation for the degree of Doctor of Science in Technology to be presented with due permission of the Department of Surveying, Helsinki University of Technology for public examination and debate in Auditorium M1 at Helsinki University of Technology (Espoo, Finland) on the 15th of December, 2005, at 12 o'clock noon.

Helsinki University of Technology
Department of Surveying
Institute of Photogrammetry and Remote Sensing

Distribution:
Helsinki University of Technology
Institute of Photogrammetry and Remote Sensing
P.O. Box 1200
FIN-02015 TKK
Tel. +358 9 4513901
Fax. +358 9 4513945
E-mail:Publications@foto.hut.fi



Image on the front cover:


ISBN 951-22-7965-7 (printed)
ISBN 951-22-7966-5 (PDF)
ISNN 1796-0711

Otamedia Oy
Espoo 2005

# ABSTRACT

Photogrammetric 3D measuring procedure needs careful planning, especially in the close-range case, in order to fulfill requirements with respect to accuracy and reliability of measurements. In the special case of indoor environment, where imaging is to be taken inside the object space, some difficulties concerning the imaging procedure can be expected. In these environments a special attention has to be paid to the arrangement of sensible imaging geometry, which will guarantee the precision of observations and the reliability of estimates. Sometimes, the division of the measuring task into smaller sub-tasks cannot be avoided. This, however, requires more planning in respect of data registering in order to get the sub-models into the same coordinate system.

In this research the issue stated above is studied and a solution to the problems is searched and found via adjusting the imaging procedure suitable to this special case. Great attention is paid to the geometrical aspect of imaging for 3D measurements and robustness of the solution. In this research a new **Circular Imaging Block** method has been developed for measuring tasks in the inside scene environment. The new method is based on constrained imaging and least squares estimation. One objective of the research has been to simplify the planning stage of the photogrammetric measuring procedure in special circumstances. The controlled imaging procedure improves the opportunity to assess the accuracy of measurements beforehand, and diminishes the need of assistance with an unexperienced user to design and accomplish the imaging. Also, the number of undesirable coordinate transformations can be decreased, since all measurements from one imaging station will be in one and the same coordinate system.

Results from real-world experiments verify that an adequate level of accuracy of measurements for object reconstruction in general is attainable with this method. Also, tests indicate that the level of reliability, which is expected in typical close-range measuring cases, can be reached. The advantages of the method can be encapsulated as the straightforwardness of imaging, no need of control data, and the use of assisted automatic procedures in image measurements.

***Keywords:*** *photogrammetry, close-range, estimation, image block, block adjustment, accuracy, reliability*

# PREFACE

This work is a result of development in number of years to create and test new ideas in the field of photogrammetry. This work started in the postgraduate school "Metsät paikkatietojärjestelmissä" (Forests in GIS) and was funded by "Metsämiesten säätiö", which I warmly thank. I was able to continue the work as a part of research project funded by the Ministry of Agriculture and Forestry of Finland, to whom I am very grateful. Also, I would like to express my appreciation to foundations Jenny and Antti Wihuri Foundation and Maanmittausalan Edistämissäätiö, which have given financial support to finish my thesis. The financial support and resources to carry out the research have been essential to complete this work. Specially, I would like to express my gratitude to Prof. Henrik Haggrén who has arranged for me these opportunities and also supervised my work at the Institute of Photogrammetry and Remote Sensing. Also, I would like to thank Prof. Clive S. Fraser and Prof. Thomas Luhmann for reviewing the manuscript and for their constructive suggestions for improvements.

I have mainly carried out this research as a one-man project. Nevertheless, I have received unselfish help from my colleagues at the institute and for this I would like to express my gratitude. Especially, I would like to thank Veli-Matti Salminen, who assisted me to build the motorised imaging system and special targets for the experiments. Also, I am grateful to Jaakko Järvinen who carried out the geodetic reference measurements for the experiments. No complaints were heard even the mensuration lasted into the late hours. I would like to express my deepest appreciation to Keijo Inkilä, with whom I had many fruitful discussions concerning the estimation theory.

The love to science what I have felt is much due to Jan Heikkilä who guided me and my fellow students in my early studies. "Try to reach your limits and stretch them even further" were instructions we learned. This attitude has helped me ever since, so thank you Jani.

I want to give my warmest thanks to all the people and instances, mentioned above or not, who have advanced this research, friends and relatives for not asking too many times "When do you get the thesis completed?"

Above all, I sincerely would like to express my gratitude to my dear wife Anita, who encouraged and supported me throughout this work. You have been my testing field of new ideas and theory, a few benefits of sharing the same professional background.

Espoo, August 2005

Jussi Heikkinen

# Contents

# List of Figures

# List of Tables

# LIST OF SYMBOLS AND ABBREVIATIONS

## Symbols

| | |
|---|---|
| $v$ | residual vector |
| $A$ | parameter coefficient matrix |
| $x$ | unknown parameter vector |
| $l$ | vector of adjusted observations |
| $P$ | weight matrix |
| $N$ | normal matrix |
| $\sigma_0^2$ | reference variance |
| $\Sigma_{ll}$ | variance-covariance matrix of observations |
| $Q_{ll}$ | cofactor matrix of observations |
| $p_i$ | weight of $i^{th}$ observation |
| $\sigma_{ii}^2$ | variance of $i^{th}$ observation |
| $u$ | number of unknown parameters |
| $r_e$ | redundancy of estimation |
| $n$ | number of observations |
| $\hat{\sigma}_0^2$ | posterior estimate of reference variance |
| $\Sigma_{\hat{x}\hat{x}}$ | estimated variance-covariance matrix of unknown parameters |
| $\Sigma_{vv}$ | variance-covariance matrix of residuals |
| $\hat{x}$ | estimated unknown parameter vector |
| $\bar{\sigma}_c$ | mean standard deviation of object point coordinates |
| $\sigma_a$ | standard error of incident angles |
| $q$ | strength of the network geometry |
| $S$ | scale number |
| $k$ | number of additional images |
| $d$ | mean object distance |
| $\Delta x, \Delta y, \Delta z$ | shift of projection centre coordinates |
| $\omega_L, \omega_R$ | rotation angle of x-axis of left and right image respectively |
| $\Delta\omega, \Delta\varphi, \Delta\kappa$ | rotation angle difference among rotation angles |
| $x_i, y_i$ | image coordinates |
| $F_{B_j}$ | constraint of base vector length |
| $B_j$ | length of the individual base vector |
| $B_m$ | mean length of the base vector |
| $X_j^L$ | projection centre X-coordinate of left image of $j^{th}$ image pair |
| $X_j^R$ | projection centre X-coordinate of right image of $j^{th}$ image pair |
| $Y_j^L$ | projection centre Y-coordinate of left image of $j^{th}$ image pair |
| $Y_j^R$ | projection centre Y-coordinate of right image of $j^{th}$ image pair |
| $Z_j^L$ | projection centre Z-coordinate of left image of $j^{th}$ image pair |
| $Z_j^R$ | projection centre Z-coordinate of right image of $j^{th}$ image pair |
| $\gamma_{x_j}$ | angle difference of x-axes of left and right image; $j^{th}$ image pair |

| | |
|---|---|
| $\gamma_{y_j}$ | angle difference of y-axes of left and right image; $j^{th}$ image pair |
| $\gamma_{z_j}$ | angle difference of z-axes of left and right image; $j^{th}$ image pair |
| $\gamma_{x_m}$ | mean angle difference of x-axes of image pairs |
| $\gamma_{y_m}$ | mean angle difference of y-axes of image pairs |
| $\gamma_{z_m}$ | mean angle difference of z-axes of image pairs |
| $r_{ij}^L$, $r_{ij}^R$, i=1,2,3; j=1,2,3 | rotation matrix elements of left and right image |
| $g_{\gamma_{x_j}}$, $g_{\gamma_{y_j}}$, $g_{\gamma_{z_j}}$ | constraint of orientation angle differences |
| $r$ | radius of camera plane rotation in image sequence |
| $P_{obj}$ | object point |
| $P_{prj}$ | projection centre point |
| $p_{img}$ | image point |
| $\lambda$ | scale factor between 3D and 2D image spaces |
| $R$ | orthonormal rotation matrix |
| $c$ | camera constant |
| $X_{obj}, Y_{obj}, Z_{obj}$ | object point coordinates |
| $X_0, Y_0, Z_0$ | projection centre coordinates |
| $\omega, \phi, \kappa$ | rotations of the camera coordinate axes x,y and z respectively |
| $x_l, y_l$ | linear distortion corrected camera centred image coordinates |
| $x_p, y_p$ | principal point coordinates |
| $a$ | correction term of affinity |
| $b$ | correction term of orthogonality |
| $\theta$ | angle between skew y-axis and corrected one |
| $x', y'$ | radial distortion corrected image coordinates |
| $x'', y''$ | decentring distortion corrected image coordinates |
| $r_c$ | radial distance of image point from the principal point |
| $r_0$ | radial distance from the point of best symmetry |
| $k_1, k_2, k_3$ | parameters of radial distortion |
| $p_1, p_2$ | parameters of decentering distortion |
| $x_{corr}, y_{corr}$ | corrected camera centred image coordinates |
| $r_{cl}$ | linear distortion corrected radial distance |
| $P_i$ | projection centre point of $i^{th}$ image in image sequence |
| $\eta$ | normal vector of rotation plane |
| $B$ | observation coefficient matrix |
| $C$ | constraint coefficient matrix |
| $\omega_0, \phi_0, \kappa_0$ | camera rotation angles of the first image in circular image block |
| $\alpha_i$, i=1,2,...,$n_1$ | plane rotation angle of $i^{th}$ image in circular image block |
| $R_{\omega_0,\phi_0,\kappa_0}$ | rotation matrix of camera with respect to coordinate system |
| $R_{\alpha_i}$ | plane rotation matrix |
| $R_{\omega_i,\phi_i,\kappa_i}$ | camera rotation matrix of $i^{th}$ image |
| $a_{ij}$, i=1,2,3; j=1,2,3 | rotation matrix $R_{\omega_i,\phi_i,\kappa_i}$ elements |
| $\beta_i$, i=1,2,...,$n_2$ | plane rotation angle of $i^{th}$ image in second circular image block |
| $d_{ij}$ | 3D distance of object points $p_i$ and $p_j$ |
| $d\omega$ | deviation of $\omega_0$ angles |
| $d\phi$ | deviation of $\phi_0$ angles |

| | |
|---|---|
| $d\kappa$ | deviation of $\kappa_0$ angles |
| $dr$ | deviation of radius |
| $d\bar{\alpha}$ | mean deviation of $\alpha_i$ angles |
| $\rho$ | correlation coefficient |
| $g_l(i,j)$ | gray-level value of pixel in (i,j) location of template image patch |
| $g_r(i,j)$ | gray-level value of pixel in (i,j) location of target image patch |
| $\bar{g}_l, \bar{g}_r$ | mean gray-level values of template and target image patches |
| $f(x,y)$ | gray-level observation from template image |
| $e(x,y)$ | random noise in template and target image |
| $g(x,y)$ | tranformation function for the target image |
| $a_0, a_1, a_2, b_0, b_1, b_2$ | affine transformation parameters used in LSQ-image matching |
| $x_0, y_0$ | initial template location for LSQ-image matching |
| $g^0(x,y)$ | initial tranformation function for the target image |
| $r_s$ | shift component in linear radiometric transformation |
| $r_t$ | scale factor in linear radiometric transformation |
| $\alpha_l$ | line direction in parametric 2D line presentation |
| $d_l$ | line distance parameter in parametric 2D line presentation |
| $dx$ | distortion correction term of x-coordinates |
| $dy$ | distortion correction term of y-coordinates |
| $\Delta x$ | correction vector of unknown parameters |
| $\theta_i$ | additional parameter, transversal tilt angle |
| $\nu_i$ | additional parameter, tilt angle of optical axis |
| $R_{\alpha_i,\theta_i}$ | plane rotation matrix, with additional $\theta_i$ angle |
| $R_{\alpha_i,\nu_i,\theta_i}$ | plane rotation matrix with additional $\nu_i$ and $\theta_i$ angles |
| $\nabla\hat{v}$ | effect of observational error on the residual |
| $\nabla l$ | observational error |
| $R_e$ | redundancy matrix |
| $Q_{\hat{v}\hat{v}}$ | estimated cofactor matrix of residuals |
| $q_{\hat{v}_i\hat{v}_i}$ | variance of $i^{th}$ residual |
| $\sigma_{l_i}$ | standard deviation of $i^{th}$ observation |
| $\hat{w}_i$ | standardized residual |
| $H_0$ | null hypothesis |
| $H_a$ | alternative hypothesis |
| $r_i$ | local redundancy number connected with $i^{th}$ residual |
| $\delta_i$ | non-centrality parameter |
| $\delta_0$ | statistically derived non-centrality parameter |
| $\alpha$ | significance level of statistical test |
| $\beta$ | power of the statistical test |
| $\delta_0'$ | controllability factor |
| $\nabla_0 l_i$ | size of gross error not exceeding the limit of rejection |
| $\lambda_i$ | sensitivity factor |

**Abbreviations**

| | |
|---|---|
| 3D | Three dimensional |
| 2D | Two dimensional |
| CCD | Charge Coupled Device |
| ICP | Iterative Closest Point |
| CDM | Conceptual Data Model |
| NRC | National Research Council of Canada |
| RMSE | Root Mean Square Error |
| MER | Mars Exploration Rover |
| NASA | National Aeronautics and Space Administration Agency |
| IMU | Inertial Measurement Unit |
| LSQ | Least Squares |
| ZOD | Zero-order design |
| FOD | First-order design |
| SOD | Second-order design |
| TOD | Third-order design |
| PAL | Phase Alternating Line (video standard) |
| NTSC | National Television System Committee (video standard) |
| LAPACK | Linear Algebra PACKage |
| RMSD | Root Mean Square Difference |
| RMSDX | Root Mean Square Difference of x-coordinates |
| RMSDY | Root Mean Square Difference of y-coordinates |
| RMSDZ | Root Mean Square Difference of z-coordinates |

# 1 BACKGROUND

The concept of *a model* can be understood in various ways, depending on the context in which it is mentioned. The model itself can be considered to be a description of a phenomenon written in the form of a mathematical formula. A model can also be regarded as a product of a planning or design process. It might be a model of a manufacturing process or it can express the shape and size of a designed object, building or artifact. In this thesis, the word *model* denotes a geometrical realization of an existing object, or group of objects, and their relationships in three dimensional space. The term *object reconstruction* can be considered to be a synonym for the word *modelling* in this sense.

Object reconstruction or geometrical modelling can be said to consist of determining the geometrical properties of an existing object and its relation to its surroundings at a given instant in time. In this thesis, the modelling process is confined to a static object, or objects, and their geometric relation to each other.

An object model consists of the geometrical properties of the object, its relation to other objects, its attributes connected with expressing its properties, its material, color properties and functionality etc. related to certain applications. The focus of this thesis is on acquiring three-dimensional coordinate information about an object from a sequence of photographs. In a image-sequence analysis, often a static camera pose is assumed and the movement of objects is the target of interest, whereas, here, the object is assumed to be static while the camera is moved between consecutive exposures.

In contrast to research objectives in the field of computer vision, here the focus of research in object reconstruction has been on the accuracy and precision of estimates. The automation of measurements and sensor-orientation determination has been of only secondary interest. The flexibility of the measuring system is, however, the concern of the research, but not at the cost of accuracy. The concept of *accuracy* is understood here as the quality of the results, while *precision* is understood as a quality of the measuring system itself. Accuracy represents the goodness of results in respect to some standards, while precision quantifies the suitability of observation to be used in a mathematical model. Sometimes, accuracy is presented as a relative number of estimated object coordinate accuracy in respect to the maximum dimension of the object, for example $1 : 10000$. This kind of representation of the accuracy number is quite common, especially in close-range photogrammetry.

The main focus throughout the thesis will be on examining a specific method of obtaining three-dimensional geometric information on an object or objects. The research is limited to close-range photogrammetric measuring methods; all measurements are therefore expected to be made using terrestrial-based, rather than airborne, methods.

The image-based 3D measuring method developed in this research project is a novel method designed for use in special conditions for the purpose of object reconstruction. This special case means that imaging is to be taken inside the object space and the goal is to reconstruct the surrounding object(s). This type of imaging case will be denoted in this thesis as a *inside scene imaging* from now on. The method developed in this research is called *"Circular Imaging Block"* -method. The method can be considered to be an additional method to close-range photogrammetric measuring methods, especially designed for inside scene imaging case. The 3D measurements made by applying this method are based on image observations from sequence of images. The sequence is taken symmetrically with respect to one navel point and the location of the sequence will be referenced as *imaging station*. This is to draw a distinction between it and *camera station* that is a location of a camera, where a single image is taken.

The following review in Section 1.3 of photogrammetric measuring methods is a cross-section of current methods designed to acquire 3D information for the purpose of object reconstruction. The review is especially concerned with the acquisition process related to this work in the field of close-range photogrammetry, not about object modelling itself.

## 1.1 Structure of the thesis

In this thesis the specific close-range photogrammetric problem regarding imaging geometry design is discussed. The subject is treated from an imaging design point of view in specific inside scene object reconstruction cases. In Chapter 1 a closer look is taken at the techniques for providing measurements for object reconstruction. More attention is paid to those methods that are applied in inside scene environments.

Chapter 2 gives an overview of the mathematical background of the estimation theory of photogrammetric measurements. In addition, the theory and concept of photogrammetric network design is discussed. Also, research work dealing with constraints in close-range photogrammetric measurements is reviewed.

In Chapter 3 the description of the *"Circular Imaging Block"* -method is provided. In this chapter the mathematical background of the developed method and assumptions made are revealed. The mathematical consideration is based on theory presented in Chapter 2.

The subject of Chapter 4 concerns the simulation tests accomplished in order to demonstrate the network design options with the presented method.

The test arrangements of the accomplished real-world experiments and the acquired reference data are presented in Chapter 5. The presentation also includes a description of the techniques used in the image observation acquisition.

In Chapter 6 the refinement of the presented method is given. The improved mathematical model and the obtained results of computations are analysed from

the point of view of measuring accuracy and the reliability of the measurements. A brief review of reliability analysis is provided for clarification of the techniques used.

The feasibility of the developed method is discussed in Chapter 7. A few aspects of the usage of the developed method are highlighted and a comparison with panoramic imaging is made. The discussion concentrates on the applicability of the method in an inside scene imaging case. In addition, suggestions for further development and direction of research are given.

In Chapter 8 conclusions are drawn and some recommendations are given.

## 1.2 The objectives of the thesis

In this thesis, the problem of close-range network design in special conditions will be studied at a deep level. The aim of the research is to find and develop a new measuring method, which is based solely, on image information, to provide 3D measurements in inside scene imaging case. This research will concentrate on method development, in order to provide a flexible measuring system for users not necessarily having a background in photogrammetry. The geometrical characteristics of the measuring conditions, for which the measuring system is to be designed, are considered to be difficult from the photogrammetric network design point of view. A solution to the problem of meeting the inside scene object reconstruction needs, where the imaging will be carried out from inside outwards, will be sought.

The starting point for the research is to simplify the close-range photogrammetric design process in this particular measuring case. The solution will be sought through overdetermination with redundant image information and by regulating the way the imaging is accomplished. The *á priori* information of imaging will be used in the form of constraints in the image block adjustment. As a consequence of the simplification of the imaging design, some degradation of accuracy in object reconstruction compared to an optimal solution can be assumed. Therefore, the following question is posed:

> *Can a circular imaging block be robust enough and provide object measurements for the purpose of photogrammetric object reconstruction?*

The answer to this question will be sought using methods involving least square estimation and accuracy assessment. The reliability of estimates and quality of measurements will be defined by means of statistical testing.

## 1.3 A review of close-range photogrammetric measuring methods for object reconstruction

In close-range photogrammetry, measuring tasks can be planned according to the required accuracy of the object model, the required completeness of the model, presentation of the model, and properties of the object itself. To a large extent, the purpose of the measurements dictates which method is appropriate for the task. Is time the restricting element for mensuration or can the measurements be made on an off-line basis? What is the usage of the resulting object model? Will it only be used for visualization or will any measures be derived from the model? Are we interested in the location of a few distinct points on the surface of the object and their relative position in respect to a time span, or is it more important to create a realistic-looking comprehensive model of an object that compromises ultimate geometric accuracy?

**Archaeological documentation:** Sometimes the model required does not have to be in 3D. It is fairly common on archaeological sites that images are taken as a basis for 2D sketches and so 2D is sufficient. Occasionally, it also means stereo pairs or rectified images of the relics of antiquity or mosaics are required. The use of photogrammetry in archaeology is quite often restricted to obtaining photographs with a known image scale for documentation purposes. Seldom has the complete geometrical model of the site been regarded as necessary, although recently some interest has been aroused in reconstructing 3D models of archaeological sites as part of the documentation process (Ogleby 2001; Koistinen et al. 2001; Pollefeys et al. 2003). A three-dimensional visualized model of the current structure of the site has been recognized by archaeologists as giving an additional tool for interpreting the site. The sub-models of the artifacts or their stereo pairs are also made in order to store them into a database (Chikatsu and Anai 1998).

**Virtual reality models:** Recently, it has, perhaps, mostly been virtual-reality models that have inspired researchers all over the world to develop methods for object model reconstruction. Virtual models are required in the construction industry for facility-management purposes and in the mining industry for autonomous vehicle or machinery interaction, also known as teleoperating (El-Hakim et al. 1997, 1998; Sequeira et al. 1999). However, perhaps the largest potential can be seen in the entertainment industry and, especially, in the gaming industry.

Creating a virtual object model does not necessarily require any real measurements to be made, but can be accomplished from scratch even though it has been realized that demand for real-world-based, rather than synthetically-generated content models is rapidly increasing. This is because real-world data have the potential to generate realistic looking models in a more automatic and faster manner than their graphic-based counter-parts, which are also more labor-intensive to produce (El-Hakim et al. 1998). In many cases, the virtual model is a combination of actual measurements with real-world image texture and partial graphical ma-

nipulation by the operator with synthetic texture. This is especially the case with virtual models of archaeological sites created where only remains of the monuments are present. The complete structure of the site has to be collected from other sources, from literature, for example (Ogleby 2001).

The geometric content of the model does not have to be complete for all applications where virtual models are used. For applications where some measures are to be derived from the model, the consistency of the model with respect to scale and derived features has to be controllable. Quite often, detailed parts of the model are first modelled in very rough or generalized form, while real-world image data are used for surface texture in order to compensate for the inconsistency of the geometric model. This is quite a powerful technique and an acceptable approach if the model is used for visualization only.

**Object reconstruction:** The measurements to be carried out for reconstructing an object model can be accomplished by using a variety of instruments. The model can be based entirely on photogrammetric measurements or measurements might be carried out using a hybrid method involving different types of sensor data. Recently, the latter seems to be the most popular method among the latest research projects (Ng et al. 1998; El-Hakim et al. 1997, 1998; Brenner and Haala 1998; Ogleby 2001). In many projects, the combination of laser scanner and video imaging is used (El-Hakim et al. 1997, 1998; Ng et al. 1998), but there are other combinations, such as a tacheometer and still video images (Ogleby 2001), airborne laser scanner data, 2D map data and aerial and terrestrial images (Brenner and Haala 1998). Also, a fully image-based approach to object reconstruction has been suggested (Seales and Faugeras 1995), where a stationary object is reconstructed from an image sequence. The camera movement is estimated on the basis of common features on the images and on object points determined from silhouette points.

**Laser scanning:** Laser scanning is a powerful technique for extracting 3D geometric information of objects. Here, the laser scanner is understood to be a device which automatically collects 3D information from an object surface in a systematic pattern. It is essential to notice that data are collected in two directions and usually stored in a form of a grid. This clarification is to make a distinction between laser-based devices that collect data only in one direction while data in the other direction is obtained through the movement of the device itself or of the object. Common to all these devices is the accomplishment of the collection of data points at a very high rate (hundreds or thousands of points per second), although, differences can be seen between 3D laser scanners in regard of their operating range and the technique they are based upon. Commonly, these devices can be divided into three categories with respect to operating range: 1) *short-range*, 2) *mid-range*, 3) l*ong-range*.

With regard to the technique laser scanners are based upon, instruments can be divided into devices based on *triangulation techniques* and devices based on *time-of-flight*. The first category comprises a combination of a laser-beam projector and

a imaging sensor device. The distance measurement in these devices is based upon angle observations with respect to the base distance of the laser and imaging sensor. The 3D point coordinates are solved based on measurements of pan- and tilt-angular sensors and derived point distance value. These devices typically fall into the category of short-range devices, but there are also devices that can be considered to be in the mid-range category.

The devices based on *a time-of-flight* technique emit a laser pulse and the time passed until the reflected pulse arrives back at the receiver is measured. In some devices, the phase difference of emitted and received pulses are measured and a more accurate estimate for time difference can be calculated.

In general, devices based on triangulation can be considered to be more accurate than laser scanners based on a time-of-flight technique. Single-point accuracy can be even $0.1mm$ in the best case with triangulation-based devices, but accuracy will drop abruptly when the object distance increases. At a distance of ten meters, the accuracy can degrade to several millimeters (Boehler and Marbs 2002). With time-of-flight scanners, the accuracy of distance measurement is quite constant, regardless of object distance. However, a single 3D point accuracy is not constant since measurement is a function of distance and angular observations. The accuracy with these devices is typically tens of millimeters in relation to a single-point location. Unlike triangulation-based devices, these scanners are able to measure up to a few hundred meters.

In comparing commercial scanner brand types, differences can be found in the way they operate. In addition to operating range, scanning speed and angular resolution, there are attributes that are scanner-type related. Also, the maximum field of view, where a single scanning session is bound to be conducted, does vary. There are scanner types that allow the scanning of nearly a full sphere, while with other devices the scanning is restricted to a field of view of the size of $40°$ in one direction. The use of a narrow field of view in scanning a large complex object will generally lead to multiple scanning sessions in order to cover the whole object. Separate scannings must partly overlap to be able to merge data sets into a single object model. This increases the number of scanning sessions even more. Data merging and data registering, has become a challenge that has inspired many researchers to find a feasible method in order to preserve object consistency in object reconstruction.

With *time-of-flight* based devices, the accuracy of measured distance is nearly constant within a few tens of meters, but there is no possibility of evaluating the accuracy of an individual 3D point observation. This is because it is hard, or even impossible, to track the precise location, where the laser beam is reflected from. Sometimes, special 3D regular targets are used in order to estimate the accuracy of a set of 3D point observations. This can be considered to be a drawback of laser scanning methods, in comparison to over-determined image-bundle measurements. In investigating laser scanning accuracy, it has been noticed that the measurement noise increases exponentially with the angle between the sur-

face normal and laser beam (Sequeira et al. 1999). The same phenomenon of reduced scanning accuracy has been discovered while comparing measurements achieved by laser scanning with digital photogrammetric measurements (Lichti et al. 2002). This knowledge of inaccuracy of observations on the surface near the coplanar-to-ranging beam has been exploited in range data registration (Sequeira et al. 1999). In the case of overlapping data, only those points from the scanning that have a better viewing angle with respect to the surface normal they belong to have been included into the model.

In most of the cases, the object cannot be modelled from one viewpoint only, so several instrument stations are needed. To estimate coordinate transformation, data sets must overlap. Because of the nature of laser scanning, no point-to-point correspondences can be established, so data sets have to be examined in order to find depth discontinuities for 3D feature extraction. In overlapping areas, the same 3D features have to be identified in both data sets. Transformation can be then based on minimizing the point distances in the overlapping area with an *Iterative Closest Point* (ICP) or equivalent algorithm (Ng et al. 1998; Sequeira et al. 1999). The problem with combining the data in the way described is that there is no controllability of the transformation and its accuracy unless the coordinate transformation is established in another way. To solve this problem, special 3D-targets have been developed. Targeting as in photogrammetry increases the need for careful planning of the mensuration task; this reduces the flexibility of the measuring method. Some laser scanning devices provide the 2D reflectance image of a scanning grid. Few reports have been given where this image has been used successfully to help in the determination of transformation between separate scans. Also, an approach has been suggested where a discrete orthoimage is calculated from image data and an interpolated orthoimage grid is compared with intensity values received from laser device (Wendt 2004). In the Olympia project, the digitalization of the statue of Zeus was established by attaching a laser scanner to the arm of a coordinate measuring device (Ogleby 2001). This guaranteed that the points clouds coexisted in the same coordinate frame. Unfortunately, this kind of approach can only be used with fairly small objects.

The uncertainty of sub-model registration based purely on laser measurements has been the reason for looking for other alternatives. In some research projects, the solution has been to combine different measuring techniques in order to achieve a better overall accuracy of the model. In combining laser range data and digital images, laser scanning is used to get most of the geometric data of the scene, while images are used only for achieving a natural texture for the model (Sequeira et al. 1999). However, there are projects, where image data are also used for getting geometric data for data fusion, or even for extracting the object structure along with laser data. In cases where photogrammetric measurements have been registered together with range data, a better and more precise coordinate system for the control network has been obtained (Guidi et al. 2002; El-Hakim et al. 2002; Beraldin et al. 2002). But there are also papers reporting the combination of tacheometer measurements and laser scanning, or of all three techniques, in

the same project (Balzani et al. 2002; Borg and Cannataci 2002). The general tendency has been to use more precise techniques to create a common coordinate system for measurements, and model only dominant features with photogrammetric methods, leaving more detailed modelling to be carried out with laser scanning.

**Image-based object reconstruction:** In most accurate close-range photogrammetric measurements up to $1 : 100000 - 1 : 1000000$ imaging is based on a multi-station convergent camera constellation (Fraser 1992). This requires a great deal of expertise in photogrammetric network design. Usually, all points to be measured are pre-targeted with retroreflecting or high-contrast targets. The reconstructed object model will then be based on these defined object points. Typically, these points themselves are distinctive points of the object model, or they are distributed on the object surface to best describe the shape of the object model. The measuring tasks requiring such accuracy are usually unique tasks not to be carried out regularly, unless it is about periodic inspection; for example in object deformation measurements. The targeting can also be carried out by projecting structured light onto the object surface or by using natural points in measurements. This slightly degrades the achieved accuracy, but enables the measurements to be made on a regular basis.

Some research has been conducted, especially in the field of computer vision, to utilize perspective properties as vanishing points in order to resolve camera orientation with respect to the object. The idea is based on the assumption of parallel and orthogonal lines or of a symmetric pattern on the object structure. This approach does not suit the reconstruction of all types of object, but there have been encouraging results, especially in the field of architectural photogrammetry (van den Heuvel 1998, 2003).

Image-based modelling from an image sequence has been of interest to many researchers seeking to recover the shape of real objects, especially in the field of computer vision. In some research activity, the motion of the object or camera is expected to be rigid (Seales and Faugeras 1995) e.g., the object is rotated around one rotation axis or the camera motion is assumed to follow a defined track.

One research line that deserves a closer look is an approach where á priori information about a camera or scene is totally disregarded and object reconstruction is performed automatically. In the research of a Belgium group from Leuven (Pollefeys et al. 2004, 2003, 2000), the focus has been on automatic reconstruction and the methodology used is probably unfamiliar to many photogrammetrists. The image sequence is assumed to be taken with a hand-held camera and the movement of the camera is allowed to be quite arbitrary. The modelling approach is based on the idea of first recovering the motion of camera and, after that, determining the object parameters of certain feature points. The feature point selection is based on using the interest operator in order to find good feature points for tracking in the image sequence. The camera motion estimation and main structural recovery is accomplished in projective space. The estimation is initialized first with an image pair, which is selected to have an appropriately wide separ-

ation of image view, i.e., a good base ratio. The coordinate frame is initialized and other images of the sequence are included gradually in the computation, while the object structure is updated accordingly. In this stage, only a basic camera model is assumed. After including all images of a sequence, and once their subsequent epipolar geometry is resolved, a bundle adjustment is performed, while intrinsic camera parameters are also taken into account. The adjustment is made in projective space; in order to transform object structure into metric space, constraints on the camera intrinsic parameters are imposed. A more-dense object structure is reconstructed from rectified stereo image pairs of subsequent images. The results of image matching are dense disparity maps and these are then combined into a global depth map by linking points from separate stereo models. In the final stage, from this depth map, a surface model in the form of a triangular mesh is created. Multiple image views ensure that the texture from images mapped on to the surface model creates a visually realistic looking model of the object structure. The basis of this research has been to create an image-based object reconstruction method, where no strict restrictions for imaging are assigned. The emphasis has been on the exploitation of automatic procedures. Aspects of imaging geometry on the accuracy of the object model have not been a big concern in research. The focus seems to have been on the development of rapid methods of object reconstruction to provide visual models from images. The resulting object models constructed with this method have been very impressive. The research work is also encouraging with respect to the development of automatic reconstruction methods.

### 1.3.1 Special case: Inside scene imaging for object modelling

Especially in the indoor environment, the imaging strategy plays a very important role. This was noticed by Dr. Foramitti who constructed an imaging system for architectural photographic recording in the early 1970's in Austria. The objective of his imaging system was to provide an image sequence in a sensible order to record architectural details of a scene for documentation(Foramitti and Ackler 1976). The imaging system consisted of a bar attached onto a tripod and a camera attached to the end of the bar. By turning the bar around the tripod and tilting the camera, he could photograph the structures in an inside scene environment. However, no photogrammetric measurements were accomplished. His invention was made in the 1970's and the photographs were analog images; the instrumentation of analogue photogrammetric stereo-plotters, used in those days, restricted the use of heavily tilted photographs for photogrammetric mensuration.

The complexity of inside scene imaging and object reconstruction has inspired many researchers since Foramitti to search for new ideas and methods to achieve realistic and accurate models of the indoor environment. Some of these efforts have concentrated on the modelling part, such as in research by Haggrén and Mattila (Haggrén and Mattila 1997), where the concept of modelling was represented as an object-space-driven approach . The indoor scene was modelled

with the help of an object-model library and the pose and orientation of the images were defined with respect to object models. The modelling was done interactively and the coordinate system was established during the modelling process. The research focused on modelling only a part of the scene. Free-net adjustment was accomplished afterwards in order to reduce the possible deformations of object space during the process of interaction.

A similar philosophy of object reconstruction was adopted by Khalil and Grussenmeyer (Khalil and Grussenmeyer 2002) in an approach to object modelling from a single image. Their starting point for the study was to solve the image exterior orientation on the basis of a determination of vanishing points. So the idea is basically the same as that in the work of Van den Heuvel in the field of architectural photogrammetry (van den Heuvel 1998). The system design of the study involves the concept of a *Conceptual Data Model* (CDM) in the reconstruction of indoor scenes. Information is represented in a data model on three levels; *geometric*, *topological*, and *semantic*. Information on the coplanarity and parallelism of objects stored in a relational database are then exploited in the modelling of the object scene. In this method, three distance measures are required to calculate the scale factors to the axes of a local coordinate system.

A more ambitious project to produce an accurate model in an indoor environment has been set up by the National Research Council of Canada (NRC) (El-Hakim et al. 1997, 1998). There has been developed an autonomous mapping system designed especially for reconstructing a model of a corridor or tunnel-type indoor scene. The system is carried out using a hybrid method by combining different types of sensor data. The system consists of wheel encoders, a laser range sensor and 8 CCD cameras. The cameras are fixed into a frame, while cameras point sideways to cover an image strip of a half circle. The range sensor is mounted on a pan and tilt unit, so it can cover the same area as the CCD sensors. All data is gathered autonomously. However, some assistance is required on image feature acquisition. The pose of the system is resolved on the basis of information from all sensors. For object reconstruction only, the image and range data are used. The system is unique, since all data is employed in a common network adjustment to solve the pose and orientation of the mapping unit and the object model simultaneously. The accuracy achieved in experiments is $1:20000$ which is admirable in such an environment of high complexity. However, pre-calibration of the system with help from a calibration frame is necessary in order to solve the relative location and orientation of individual sensors. This information is then used as á priori knowledge in the network adjustment process to stabilize the computation.

**Panoramic imaging:** The use of panoramic images in object reconstruction has been of interest in many papers recently. Panoramic images can be considered to be ideal media for acquiring images in inside scene environment. The idea of panoramic images has been known for over a century, but using this concept for measurements in close-range photogrammetry has only recently been of interest.

Panoramic images can be obtained by merging multiple central projective frame images into a single panoramic image or by using cameras especially designed to acquire the intensity information with panoramic projection.

In order to acquire panoramic image information from multiple central projective frame images, it is necessary to have a single projection centre that all images share. This can be accomplished by estimating mathematically the possible eccentrical difference between projection centres and taking into account this effect in constructing the panoramic image (Wester-Ebbinghaus 1982; Hartley 1993; Luhmann and Tecklenburg 2002), or by trying to place the camera in a rotational mount piece so that no eccentrical difference exists between image perspective centres (Pöntinen 1999; Kukko 2004).

In the case of special panoramic cameras, the imaging is based on a single array sensor. The panoramic image is constructed while applying plane rotation for the vertically aligned sensor and acquiring the intensity information during rotation. The spatial resolution of the image is then dependent on a minimum rotational resolution in the horizontal direction, while, in the vertical direction, the resolution is limited by the number of sensor elements in the array. The sensor array is assumed to be perpendicular to the axis of rotation, but there have been reports of this assumption having been found to be incorrect (Schneider and Maas 2005). Also, there have been observations of uneven rotation of the sensor in the direction of rotation and of violations of a planarity constraint (Parian and Gruen 2004). By applying correction values based on calibration, it has been possible to reduce the error of the single observation from $10$ to $0.2$ pixels (Schneider and Maas 2005).

However, object reconstruction, based upon the image ray intersection, cannot be achieved from a single panoramic image. The image observations from a panoramic image can be equated with the horizontal and vertical angle observations from the theodolite. Consequently, to be able to measure 3D point location by means of image ray intersection, at least two panoramic images have to be created with a difference in location. In order to have observational redundancy, three panoramas are the minimum. Before object reconstruction, images have to be relatively oriented or oriented with respect to a chosen coordinate system. With the use of photogrammetric bundle adjustment, the orientations can be computed in a rigorous way. Luhmann and Tecklenburg have noted in their investigation that generally $5 - 7$ tie points are sufficient for a complete room(Luhmann and Tecklenburg 2002).

For object measurements, the corresponding image-point observations have to be made in the same way as when using central projective frame images. However, in contrast to frame images, the epipolar line, where correspondent points should coexist, is not a straight line but a sinusoidal curve. This is due to the presentation of the panoramic image projected on the surface of a cylinder. The benefit of panoramic images in inside scene measurements by imaging outwards from inside is their coverage of full $360°$. This means that an object point can

possibly be seen in all panoramic images of the project. However, the image scale can vary largely from image to image. This is why, in many research projects, an image management and browsing system has had to be created in order to find all possible images where the object point can be seen (Luhmann and Tecklenburg 2004; Chapman et al. 2004). In very complex environments, the image management system is a system component that is clearly crucial in getting the task accomplished (Chapman et al. 2004).

The accuracy achieved in object reconstruction by using panoramic imaging has generally been quite adequate for the requirements of an object model. By using four panoramas constructed from a sequence of central projective images for object measurements, the root mean square error (RMSE) has been of a size of $3 - 5mm$, when object dimensions have been $25m \times 25m \times 8m$ (Luhmann and Tecklenburg 2004) and $45m \times 45m \times 20m$ (Schneider and Maas 2005). A similar accuracy range of $RMSE \approx 3mm$ has been reported with the use of special panoramic cameras (Schneider and Maas 2005). Even though, with panoramic imaging, almost the whole scene can be covered, depending on the structure of object scene, there can still be occluded areas where no image information is obtained. In order to recover from this shortcoming, an image adjustment system has been developed, where central projective frame image observations are adjusted simultaneously with panoramic image observations (Schneider and Maas 2005).

Panoramic imaging has also aroused interest in the computer vision community. Panoramic imaging is sometimes called *omnidirectional imaging* in computer vision literature. Research work has been undertaken in the development of construction methods of panoramic images as well as in 3D object reconstruction. The main objective of research in these research projects has concentrated on various ways to recover the camera movement during imaging. The ultimate goal of the research has been to resolve the camera rotation in an automatic way (Kang and Szeliski 1997; Jiang et al. 2005). In object reconstruction, a 3D mesh has been generated according to all possible pixel locations where the correspondent image point has been found on other panoramic images. Also, here, automation of the process has played the main role in investigations. Unlike with research work in the photogrammetric community, the geometry of imaging regarding object reconstruction has not been an important part of the research.

**Stereo panoramic imaging:** Some variation from the strict panoramic imaging rule has been suggested where imaging does not share a common projection centre. The aim of research in that case has been to create a stereo system with a panoramic viewing capability (Peleg and Ben-Ezra 1999). The construction of stereo panoramas is achieved from two image sequences. Each image sequence is obtained by rotating the camera around a static axis along a circular path. The looking direction of the camera is tangential to the circular path during imaging. The second image sequence is created in the same way, except for the opposite tangential viewing direction of the camera. The aim is to create a panorama im-

age that consists of image strips from both image sequences. For the purpose of stereo viewing, the image is projected onto a planar surface as a stereo pair with a chosen viewing direction.

Another approach exploiting similar imaging geometry is called *omnivergent stereo* (Seitz et al. 2002). The idea of imaging two image sequences is the same as that found in the work of Peleg and Ben-Ezra. Also in this work, the aim has been to reduce redundant image information and only store those image rays tangential to the circular path. Along with basic image construction, the *spherical omnivergent image* model, where collected image rays are stored according to their horizontal and vertical angle direction values, is presented. By storing image ray information so that image rays with the same horizontal angle are stored in the same image column, and image rays with equal vertical angles are stored on same row, the epipolar line will go along the scan-line and the correspondence of image points can be found on the same row. This is a benefit when using standard stereo matching algorithms for object reconstruction. In addition, an approach acquiring two images is presented for creating omnivergent stereo: *centre-strip* stereo, based on a single image strip collection (equivalent to the work of Peleg and Ben-Ezra), and *dual-strip* stereo, exploiting image acquisition from two symmetrical off-centre slit images. In both *panorama stereo* and *omnivergent stereo,* ideal imaging conditions are assumed in research and no discrepancy of expected imaging geometry is considered. Also, the quality of the obtained object point coordinates is not examined.

One research project, or more like a mission, to be mentioned is the *Mars Exploration Rover* (MER) mission that has connections to the reported research area (Maki et al. 2003; Bell et al. 2003). In early 2004 the MER mission landed a pair of rovers on the surface of planet Mars. The mission was launched by the *National Aeronautics and Space Administration Agency* (NASA). Altogether $10$ cameras are placed on each rover to explore the Martian surface. From the $10$ cameras two stereo camera pairs are the target of interest concerning this research; namely the *Navcam* and *Pancam* stereo cameras. The stereo cameras are mounted on a mast $1.54m$ above the surface in a pan- and tilt-unit of the rover. The *Navcam* cameras are within a distance of $200\,mm$ apart and the *Pancam* cameras have $300\,mm$ separation in camera bar. The imaging system resembles the imaging system used in the earlier Mars missions of *Mars Pathfinder* and *Viking*.

The primary objectives of the *Navcam* camera system is to acquire an "end of the day" panorama of the local terrain after a rover traverse. This terrain model is used in planning the route of the rover in the next stage. The stereo image system can produce a stereo view covering the whole $360°$ in order to obtain a terrain model of the scene. A typical *Navcam* panorama consists of a sequence of $10$ stereo pairs, spaced apart by $36°$. In order to acquire a terrain model, images are reprojected to epipolar images and an image correlation technique is used to produce disparity maps of the scene. The disparity maps obtained from separate stereo images are then combined using angular information gained from the angular

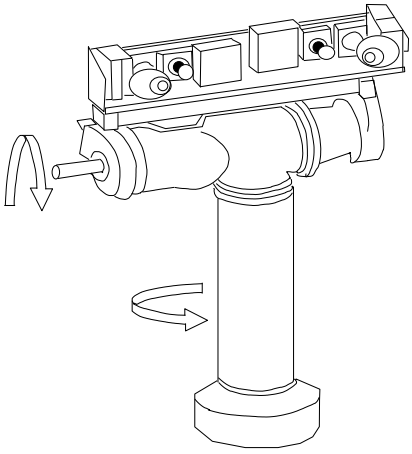

**Figure 1.** Imaging geometry of panoramic imaging created in Mars Exploration Rover (MER), redrawn from (Maki et al. 2003).

actuators of the pan-tilt-unit. However, if image mosaics of the scene are to be created, tie point measurements between images need also to be made. The rover is equipped with a *Inertial Measurement Unit* (IMU), and in combination with information obtained from rotation and orientation of the rover wheels, this takes care of positioning of the rover in respect to previous locations. When needed, the position information is updated based on image measurements of objects, seen from both imaging sites.

The imaging system used for 3D object measurements, where measurements are based on image observations made from image sequences of camera pair attached to a rotating bar, is depicted in Figure (1), which exhibits the imaging geometry. The imaging geometry is comparable to imaging accomplished in *omnidirectional stereo* and *panorama stereo.* The imaging system of *Mars Exploration Rover* cannot be considered to belong under the title of indoor imaging, but surely demonstrates the imaging conditions of inside scene environment, defined earlier in this section.

To summarise, in this Chapter a review of photogrammetric close-range measuring methods aiming to 3D object reconstruction have been made. Especially, more close look on methods applicable to inside scene environment is taken. The reader is encouraged to bear in mind the imaging geometry presented in Figure (1) and described in the last part of the section dealing with stereo panoramic imaging, since it resembles the imaging procedure used with circular imaging blocks. A comparison of the developed method with methods presented here in this section is to be made later in Chapter 3.

# 2 INTRODUCTION

## 2.1 Bundle block estimation

The reconstruction of an object purely on the basis of image information needs to be performed with proper imaging geometry in order to obtain a consistent and undistorted object model. Sometimes, especially for visualization, it is enough to get a model that resembles a real object. In cases where many sub-object models have to be merged into a larger and more complicated model, there is a risk of major problems if the consistency of model geometry has not been dealt with properly. Preferably, the whole model should be homogeneous in terms of accuracy of measurements. This, however, is quite difficult to achieve. In order to get an appropriate solution, imaging has to be planned carefully.

In photogrammetric literature, special attention has been paid to the problem of achieving a good imaging network (Fraser 1982, 1984; Mason 1995; Fraser 1996). For some applications, requirements for accuracy can be very strict. There have been reports of image-based object measurements achieving an accuracy of one part in one million with respect to the size of the object (Fraser 1992). In such cases, many planning iterations may be needed to achieve an optimized network. The accuracy of a final 3D model depends upon:

1. the accuracy of image observations,
2. the geometry of imaging network,
3. the number of observations, and
4. the correctness of camera model.

The effect of image observation accuracy is apparent on object-parameter determination. How the geometry of intersecting image rays has an effect on object accuracy can also be clearly shown with error propagation. An increase in the number of observations above the number that is necessary to solve the object parameters does not only improve the accuracy of object measurements, but also gives us a tool with which to estimate the precision of our measurements without any exterior reference. By applying a correct camera model, the occurrence of systematic errors on object model coordinates can be prevented.

The reconstruction of an object model can be accomplished from multiple stereo image pairs. From each stereo image pair, object points can be measured and a sub-model representing a partial object created. Usually the goal is to reconstruct the object as a whole and this initiates a need to have all sub-models transformed into the same coordinate system. A rigid body, conformal transformation

is often used for transferring the sub-models into a common coordinate system. Unfortunately, this kind of approach generates quite a number of sub-models and therefore some kind of image handling system is required to manage the whole measuring project. Also, more effort has to be put into the search for corresponding object features for the purpose of coordinate transformation. These numerous sub-blocks are difficult to handle in the same project and their orientation can be quite arbitrary in object space.

In stereo measurements, an object point is measured on both images. Sometimes, the relative position and orientation of the image pair have been resolved beforehand and the determination of model coordinates is to compute the intersection point of two image rays in 3D space. In an ideal stereo pair case, corresponding image rays will intersect in one unambiguous 3D point location. The disadvantage of the stereo measurement approach is that it does not provide real quality information of object point determination. Some feed-back of the quality of the relative orientation of an image pair is available in the form of $y$-paralax, though. Also, stereo imaging is not geometrically the most accurate imaging configuration, even though it is widely used. In close-range photogrammetric measurements, the multistation convergent configuration has been found to be the optimal solution for imaging geometry (Fraser 1984, 1996).

As previously mentioned in this section, the number of observations has an effect on object model accuracy. In an *overdetermined* case, there are more image observations of each object point than the minimum requirement. Due to random noise on image observations or possible systematic error, the corresponding image rays from multiple images do not necessary intersect at the same point. So the problem is to solve the 3D point location, where the observations have the best fit. In the field of geodesy and photogrammetry, the solution to the problem has been solved with the *Least Squares (LSQ) Estimation* model (Slama 1980). Object point coordinates can be solved by minimizing the weighted squared sum of observation errors in the image space. The image orientation values are also commonly solved in the same adjustment. The problem is then to find the best fit of the bundle of image rays with respect to each other and possibly with respect to the pre-known object points or features. This estimation model is called the *bundle adjustment* method (Brown 1976). Adjustment methods have been widely used, first in aerial photogrammetry applications (Brown 1976) and later in close-range photogrammetric measurements (Wester-Ebbinghaus 1978; Fraser 1984). Recently, the computer vision community has also adopted the bundle method in their computation models (Pollefeys et al. 2004). By using the bundle estimation method in an overdetermined case, it is possible to assess the precision and reliability of measurements, plus the quality of measurements, without any exterior reference data.

The estimation model can be represented in the form of least squares in the following way:

$$v = Ax - l \tag{1}$$

The functional model can be derived as an observation equation, Equation (1), where the discrepancy between the linear function of parameter values $x$ and observations $l$ is presented as a residual vector $v$. The matrix $A$ is a coefficient matrix of unknown parameter vector of this linear function. This observation equation is an explicit function where observations can be expressed as a linear combination of parameters. This, however, cannot be constructed in every case; when it cannot be, observations and parameters have to be adjusted in the same adjustment by using a general adjustment model (Mikhail 1976).

The objective of this LSQ estimation is to minimize the sum of squares of weighted residuals. If the first derivate of Equation (2) with respect to the unknown parameter vector $x$ is computed and set to zero, we end up with Equation (3). This will guarantee the minimum criteria and the solution for unknowns $x$ can be computed. In the literature, it is common to denote the symmetric squared matrix $A^T P A$ in Equation (3) as $N$ and the vector $A^T P\, l$ as $t$ (Mikhail 1976). The symmetric squared matrix $N$ is often designated the *normal matrix*.

$$v^T P v = (Ax - l)^T P\, (Ax - l) \tag{2}$$

$$\begin{aligned} x &= (A^T P A)^{-1} A^T P\, l \\ &= N^{-1} t \end{aligned} \tag{3}$$

,where

$$P = \sigma_0^2\, \Sigma_{ll}^{-1} = Q_{ll}^{-1} \tag{4}$$

The weight matrix $P$ in Equation (4) is an inverse of the cofactor matrix. The cofactor matrix $Q_{ll}$ is a variance covariance matrix of image observations $\Sigma_{ll}$ scaled by the reference variance of the adjustment. This information is hardly ever available and has to be created on the basis of prior experience. Since the image observations are assumed to be independent, the matrix will be reduced to a diagonal matrix, whose diagonal elements are in a form of

$$p_i = \frac{\sigma_0^2}{\sigma_{ii}^2} \tag{5}$$

where $\sigma_0^2$ is the reference variance of adjustment and $\sigma_{ii}^2$ is the variance of the equivalent observation. Often the reference variance $\sigma_0^2$ is selected as the variance of image observations, in which case the weight of a single image observation is unity, or unit weight. If only image observations are included in the adjustment, the weight matrix $P$ will then be the identity matrix. However, other types of observation can be included in the estimation as well. They can have different variance properties as image observations and also image observations can have different variance values, depending on whether the observation is from a targeted point or a natural object point. Then the identity matrix will not be adequate as a weight matrix for the adjustment.

The equivalence of the matrix presentation of the bundle model can be found with the four factors presented previously in this section.

1. The weight matrix $P$ includes the observation accuracy information.
2. The coefficient matrix of unknown parameters $A$ contains the effect of imaging geometry. The distribution of object points and features, as well as the relative position and orientation of image bundles, have a strong effect on the structure of the matrix $A$. That is why the matrix $A$ is often called the *design matrix*.
3. The redundancy $r_e$ of the adjustment can be calculated from the number of observations and number of rows $n$ in the matrix $A$ (in the assumption of explicit equations) compared to the number of unknown parameters $u$ , i.e., size of vector $x$. So redundancy is $r_e = n - u$.
4. The precision of the camera model can be evaluated from camera calibration measurements or, if the interior orientation parameters of the camera are included as unknowns, the precision values can be derived from the parameter variance-covariance matrix $\Sigma_{xx}$, as discussed below.

The possibility of assessing the quality of measurements is one major advantage of using LSQ estimation. Object space uncertainty can be evaluated by deriving the observation uncertainty $\Sigma_{ll}$ by use of error propagation into the variance-covariance of unknown parameters $\Sigma_{xx}$. The uncertainty of the object feature parameters is also dependent upon the geometry of the imaging network. Accordingly, the estimate of variance-covariances of parameters is a function of the design matrix $A$ and weight matrix $P$ in the form of the inverse of the normal matrix $N$ scaled by the posterior estimate of the reference variance of unit weight $\widehat{\sigma}_0^2$. It is given as

$$\Sigma_{\hat{x}\hat{x}} = \widehat{\sigma}_0^2 N^{-1} \tag{6}$$

The variance-covariance matrix of unknown parameters $\Sigma_{\hat{x},\hat{x}}$, Equation (6), can be used in the evaluation of adjustment results. The trace $tr(\Sigma_{\hat{x},\hat{x}})$ has a direct

relation to Root Mean Square (RMS) values and is therefore used in the assessment of results, as well as in the simulation of the imaging network design (Fraser 1982). The quality of observations can be reviewed by examining the variance-covariance matrix of residuals $\Sigma_{vv}$. Methods to detect blunders, or outliers, are commonly based on residual variances and covariances.

This compact presentation of the bundle method is very general and is designed to motivate the adoption of the method in image-based measuring configurations. A more detailed description can be found in the literature (Mikhail 1976; Mikhail et al. 2001).

## 2.2 Concept of Photogrammetric Network Design Problem

In photogrammetric measurements, the accuracy of 3D measurements depends highly on the camera configuration. The best result can be achieved in the case where images are exposed at the convergence angle of $90°$. This is not a strict requirement, but having an incident angle of intersecting image rays of $60° - 90°$ from two or multiple images (Fraser 1992), will almost result in isotropic precision in all three coordinate directions. Unfortunately, this is occasionally difficult to arrange in practice. In cases where the optimum geometry cannot be constructed, other criteria for the estimation model are used to achieve a stable solution. In aerial photography, the overlap of two images should be adequate to guarantee the accuracy of the model.

The achievable accuracy of a photogrammetric measuring system largely depends on the localization and distribution of the control points or control features to be used. The imaging device, its accuracy, and geometrical stability have to be known when planning the mensuration system. These all have an effect on the final measurement precision. Changing one component might have a great impact on some other component and in that way affects the accuracy of the whole measurement system. The standard procedure is to adjust the measurement conditions iteratively to meet the accuracy requirements. The design of the measurement system can be divided into ZOD, FOD, SOD and TOD levels of planning, according to Grafarend (Grafarend 1974) and Fraser (Fraser 1984).

- zero-order design (ZOD): the datum problem
- first-order design (FOD): the configuration problem
- second-order design (SOD): the weight problem
- third-order design (TOD): the densification problem

According to Fraser (Fraser 1984, 1996), in close-range photogrammetric networks, this classification is not really applicable and the ZOD- and SOD-level design are greatly simplified compared to stages in geodetic network design, where

the design classification was first presented (Grafarend 1974). The ZOD-level planning is about the fixing of seven appropriate object space parameters in order to remove the network's datum defect. The variance-covariance matrix of object space features $\Sigma_{\hat{x}\hat{x}}$ is highly dependent on the choice of this minimum control. Even though the shape of the network will remain unchanged, the changes can be seen in the numerical values of $\Sigma_{\hat{x}\hat{x}}$ as a result of this choice. However, the ZOD-level planning can be ignored when only the shape of the object is needed. It is also possible to solve the datum defect problem by applying numerical methods. The solution is found by constraining the minimum $\widehat{x}^T\widehat{x}$ of the linear equation system. One approach is based on inner constraints in adjustment. Alternatively, same solution can be achieved by using the singular value decomposition algorithm. The solution based on inner constraints has proved to be more feasible in practice (Fraser 1984; Mikhail et al. 2001), while the latter approach has had a mainly theoretical value (Inkilä and Laiho 1989).

The most demanding phase in close-range photogrammetric network design is probably planning the camera station configuration: the FOD level. As an indicator of point triangulation precision in a convergent, multi-station photogrammetric network, Fraser has presented a formula (Fraser 1984):

$$\overline{\sigma}_c = \frac{q}{\sqrt{k}} S\sigma = \frac{q}{\sqrt{k}}\, d\sigma_a \tag{7}$$

From Equation (7) we can see that the mean standard deviation of object point coordinates $\overline{\sigma}_c$ is dependent upon the

- image coordinate standard error $\sigma$;
- scale number $S$, which is a relation of mean object distance $d$ and camera constant; and
- a term $q$ expressing the strength of the network geometry.

The effect of the number of images $k$ on object point accuracy is inversely proportional to the square root of $k$, assuming that the additional images do not essentially improve the geometry of the network. If the observation accuracy is expressed in a form of standard error of incident angles $\sigma_a$, the scale number reduces to mean object distance $d$. Values of $q$ are expected to range from $0.4$ to $0.7$. The value $q = 1$ might be expected for a weakly convergent network. In photogrammetric projects redundant measurements are mostly used. The redundant measurements combined with the bundle of rays method provide the capability to estimate the precision and reliability of the measurement operation. This definitely gives us feed-back information from the network design problem. In the case of bundle estimation and convergent image geometry, where the object variance-covariance matrix $\Sigma_{\hat{x}\hat{x}}$ is expected to be diagonally dominant, the value

of $qS$ can be then expressed with a sub-diagonal matrix related to the 3D point parameter coefficients in the design matrix.

It can be noted that planning can be a time-consuming process and can require a good knowledge of how photogrammetric network design can be achieved successfully. However, research work has been carried out in order to simplify the process by implementing an expert system for network design (Mason 1995), where the convergent, multi-station photogrammetric network has been assumed. This basically means that we are able to pose the camera stations around the object, and images can be taken with convergent orientation. The placement of the camera stations may often be constrained by various factors such as: image scale, depth of field, incident angle and workplace environment (Mason 1995). The use of genetic algorithms for automating the photogrammetric network design process has also been proposed (Olague 2002).

In some applications where the precision requested is not so high and the imaging conditions are complicated, some other kind of approach for imaging design can be chosen. Sometimes, constructing a convergent image bundle is not even possible, especially in archaeological and architectural applications. This can also be the case in industrial applications (Fraser and Mallison 1992; Fraser 1996), where the problem of reconstructing the model of an inside scene often occurs. The reason why the image block is not created from inside scene is that, especially in concave corner areas, the imaging geometry is poor. The result of poor geometry combined with noisy observations is a deformed object model. In most cases, the problem has been solved by taking stereo images or creating sub-networks and reconstructing the sub-models from them. The whole model is then recreated by combining these models. This is done by solving the similarity or rigid conformal transformation between sub-models with the help of common object features. An alternative way to combine models is to use ICP or similar algorithms, where the distance between point sets is minimized. This approach, however, assumes that a substantial number of points are included in transformation estimation.

## 2.3 Constrained Imaging

In order to stabilize the adjustment process of the image block with poor imaging conditions, some improvements have been suggested. The improvements have mainly concerned the introduction of the prior knowledge of the imaging or object properties in an adjustment. Papers dealing with this issue have most commonly arrived at a solution that applies constraints in objects space (Youcai and Haralick 1999). Constraints have been established between object points revealing known relationships in object space. The exploitation of object information has been taken a little further by photogrammetric formulations, including parametric presentation of 3D linear features such as lines, circles, and ellipses. Other conic sections, as well as b-splines in bundle adjustment, have also been presented (Mulawa 1989; Mulawa and Mikhail 1988). Presentation binds together

the object feature parameters, image exterior orientation parameters and image observations. In this approach, a strong connection is created between object features and image ray bundles. Also, inter-feature relations, such as parallelism, perpendicularity, coplanarity, etc. have been included in the estimation model. The stabilizing effect of using linear features in place of points is based on better localization of features on images, more rigorous solutions of transformation between image space and object space, as well as improved redundancy in adjustment (McGlone 1995; Heikkinen 1994). Also, in the computation of exterior orientation based on a linear transformation model, the same approach has been followed (Ji et al. 2000).

Less effort has been put into making use of known information about imaging conditions. In some cases, pre-computed relative orientation of stereo image pairs has been included in the adjustment via weighted observations of orientation parameters. Usually, relative orientation parameter values are considered to be fixed, while only measured object points are taken into the computation of the common adjustment. But there are examples where a bundle adjustment has been exploited in an extensive way. In the National Research Council of Canada (NRC), an autonomous mapping vehicle has been developed where, together with image sensors, a range-sensor, as well as navigation-sensor data are included in common bundle adjustment. The relative position and orientation of image sensors with respect to the vehicle coordinate system is pre-calibrated and this information is then used as constraints in adjustment (El-Hakim et al. 1997, 1998).

In research conducted by King, auxiliary information of the imaging condition was included in the adjustment (King 1994). In his research, the bundle adjustment was computed with constrained stereo pairs. This type of case resembles the adjustment of independent models. According to the theory of independent models (Schwidefsky and Ackermann 1978; Slama 1980), the three dimensional similarity transformation is to be estimated among model and control point coordinates. In this computation model, stereo models are the computing units, while seven-parameter transformation is solved assuming only random noise in model coordinates. In King's investigation, image coordinates were the primary observations, not model coordinates, and the á priori information of the stereo case was taken into account as additional observations. In his model, camera relative rotations and the shift vector between two cameras were introduced in adjustment as additional observation equations. By assigning different weights for camera parameter observations, the restrictiveness of the stereo pair geometry case could be tuned. This is, in fact, the same as with extended independent models, where an additional parameter set is used in order to compensate the effect of systematic errors in stereo model coordinates. However, the set of unknown parameters in King's method was different.

Another solution for the adjustment of the block of stereo pairs that King presented is to use constraints between camera parameters. The constraints can

be assigned to projection centre coordinates as a constant shift ($\Delta$x,$\Delta$y,$\Delta$z) inside a stereo pair and constant rotation angle difference among rotation angles ($\omega_L - \omega_R = \Delta\omega$,$\Delta\varphi$,$\Delta\kappa$).

If LSQ-type estimation is to be applied, the constraints can be given as a constraint equation. Absolute constraint equations are more strict than weighted observations and using them leads up to an additional degree of freedom (Mikhail 1976; Mikhail et al. 2001). This works well if base vectors of all stereo pairs are collinear or parallel with each other. In order to allow the stereo pairs to have varying orientation, different kinds of constraints have to be defined.

$$F_{B_j} = B_j - B_m = 0 \tag{8}$$

$$B_j = \sqrt{(X_j^L - X_j^R)^2 + (Y_j^L - Y_j^R)^2 + (Z_j^L - Z_j^R)^2} \tag{9}$$

$$B_m = \frac{1}{n}\sum_{j=1}^{n} B_j \tag{10}$$

If a constraint of a base vector $B$ length is applied instead of a shift difference of projection centre coordinates, the varying orientation of stereo pairs can be allowed. King used this constraint in his work, but instead of using a constant value for base length, he allowed this value also to vary. By requiring the length of the individual base vector $B_j$ difference to mean length $B_m$ of base vector to be minimized, the constrained could be set as depicted in Equation (8-10).

Minimization of orientation-angle differences to mean difference values could not be used. This was because the rotation angles of the cameras were expressed with respect to the object space coordinate system. For the bundle of stereo pairs with fixed relative rotations, the convergence angles must be invariant for all stereo pairs, irrespective of the orientations of the camera axes with respect to the object space coordinate system. Assuming the orthonormal rotation matrix $R$, the convergent angles could be derived by computing the dot product of two coordinate axes and applying the inverse cosine of the product, as depicted in the following equation.

$$\begin{aligned}
\gamma_{x_j} &= \cos^{-1}(r^L_{11_j} r^R_{11_j} + r^L_{12_j} r^R_{12_j} + r^L_{13_j} r^R_{13_j}) \\
\gamma_{y_j} &= \cos^{-1}(r^L_{21_j} r^R_{21_j} + r^L_{22_j} r^R_{22_j} + r^L_{23_j} r^R_{23_j}) \\
\gamma_{z_j} &= \cos^{-1}(r^L_{31_j} r^R_{31_j} + r^L_{32_j} r^R_{32_j} + r^L_{33_j} r^R_{33_j})
\end{aligned} \tag{11}$$

The notation $r$ in the Equation (11) marks the rotation matrix $R$ element from the right $r_j^R$and left $r_j^L$ image of the $j^{th}$ stereo model, respectively.

$$
\begin{aligned}
g_{\gamma_{x_j}} &= \gamma_{x_m} - \gamma_{x_j} \\
g_{\gamma_{y_j}} &= \gamma_{y_m} - \gamma_{y_j} \\
g_{\gamma_{z_j}} &= \gamma_{z_m} - \gamma_{z_j}
\end{aligned}
\tag{12}
$$

In addition, King included the mean values of convergence angles into constraint equations following the same principle as that of projection centre coordinates, see Equation (12). As mean values are used in the constraint equation instead of constant values, the means need to be updated after every iteration in the least squares model estimation for this nonlinear case.

The methods described are examples of techniques that can be exploited when imaging geometry cannot be optimized. The reason for not having optimal geometry can be due to the structure of the object itself; the environment, which restricts the possible imaging stations, or the computational speed required. The ramifications of not taking care of stability in the reconstruction process can lead to a distorted object model.

# 3 CIRCULAR IMAGING BLOCK

In most accurate object reconstruction projects, the network design is based on convergent imaging and targeted object points. There are many cases when this is not possible. The imaging method presented here is designed for special conditions where the traditional approach in the network design problem (Fraser 1984; Mason 1995) meets its limitations, when, for example, visibility is somehow compromised, as with very complex object structures (Chapman et al. 2004; Leroux et al. 2002). The only solution to this problem is for the imaging to be accomplished inside the object space, not around the object, i.e., inside scene imaging.

The developed method is designed especially for inside scene imaging type of modelling cases. The applications for this imaging system are congruent with applications of methods presented in Section 1.3.1. This novel method is based on image measurements made from an image sequence, but differs from object reconstruction methods based on image sequences (Pollefeys et al. 2004, 2003, 2000) presented in Section 1.3, in the way imaging is accomplished. In the image sequence research, a hand-held camera was moved arbitrarily, whereas in this approach the camera is supposed to be moved in a more rigorous way. Here the sequence is assumed to cover the whole scene of 360°. Nonetheless, here, the question is not about panoramic imaging, where a single image of panoramic view is created. In this method, the measurements are based on image ray bundles of central projective images of a frame camera. The images in the sequence do not share a common projective centre like images in the creation process of a panoramic image from multiple-perspective images (Wester-Ebbinghaus 1982; Pöntinen 1999). The capability of measuring 3D objects is merely based on image observations made from images having a displacement of projection centres on subsequent images. All observations from the whole image sequence are expected to be handled in a common bundle adjustment. In the computation of object-point or feature parameters, the constrained relative position and orientation of images in sequence will also be resolved.

## 3.1 Introduction to the Circular Imaging Block Concept

The novel method of *"Circular Imaging Block"* utilizes the constraints between camera stations. The idea is to minimize the workload and need of photogrammetric expertise in photogrammetric network design. The number of parameters to be used in specifying the imaging geometry is reduced to just a few. This also gives rise to the possibility that non-photogrammetrists might design the photogrammetric network without any knowledge of accuracy aspects of the photogrammetric measurements and the theory of error propagation in the LSQ esti-

mation model. In order to achieve this goal, the imaging has to be accomplished in a specific way.

Earlier in traditional terrestrial photogrammetry, images were often constrained to be taken so that the set of camera stations would comply with normal stereo photography. This was partly because only analogue plotters were used for coordinate measurements in those days. The restriction of those devices forced the convergence of the images to be within fixed limits. Also, large image scale differences could not be accommodated. With analytical methods, the use of constraints between camera stations in bundle adjustment became more flexible. In practice, only the measured distances between camera stations were used as additional observations or constraints. However, constraints in the form of equal height of camera stations have also been applied, as well as lining up the set of camera stations with equal orientation. In the latter case, the arranged camera configuration of imaging could be introduced in computation by fixing one or two coordinates of the projection centres in adjustment. More often, these object space observations were only used in order to get better initial values for camera pose estimates.

### 3.1.1 Definition of Circular Imaging Block

In this research, not only constraints are applied between camera stations, but the chosen parameters to express camera pose rely on the assumption that images are taken in a pre-defined way. The imaging is especially designed to be used in applications where the measurement is meant to be made ”inside the object-space”. This means that object features whose position, size, and orientation, are to be measured are distributed around some pre-defined area, for example, the room of a building. Instead of taking multiple stereo pairs and combining these sub-models as a final model, in this approach only a few imaging stations are needed. At each imaging station, tens of images are to be taken, depending upon the distance of object features from the camera and the field-of-view of the used camera. In order to obtain three-dimensional measurements from a single imaging station, there must be an offset between the recorded images. This parallax can be achieved by moving the camera along a pre-defined trajectory between successive exposures. In this research, the trajectory is assumed to be a circle on an arbitrary plane. In practice, this can be arranged by fixing the camera at the end of a supporting bar. The other end of the bar is then positioned to provide a navel point for revolution. The navel point can be attached to, for example, a tripod, which has been the case in real-world experiments, as will be described in Section 5.3. The assumptions for the imaging are as follows:

- the bar is rotated only on a plane or on a conic surface where the peak point of the cone coexist with the navel point of revolution and the axis of revolution goes along with axis of the cone, yet taking care that only plane rotation is applied to the camera at the end of the bar.

- one point in a bar will be in a constant position, i.e., the navel point.
- the orientation of the camera with respect to the bar is constant throughout the imaging sequence.
- subsequent images must overlap so that tie points can be measured between images.
- sequence of images will cover $360^\circ$ so that tie points between the first and the last image in sequence can be measured.

The image block fulfilling these assumptions is called a "*Circular Imaging Block*", Figure (2). The minimum number of images required in sequence is dependent upon camera object distance and field of view. Also, the camera distance from the navel point and the orientation in respect to the bar have an effect on this minimum number. If using continuous imaging, for example, video imaging and making measurements on each frame of the video sequence, enough overlap between subsequent images can be guaranteed. This undoubtedly increases the redundancy of observations. The extra work caused by adding more images onto the image block is evident, but, by applying autonomous image measuring algorithms, the workload can be reduced substantially. The camera does not necessarily have to be a video or digital still camera; analogue film camera images can also be taken. However, the amount of image mensuration needed favors the use of digital images.

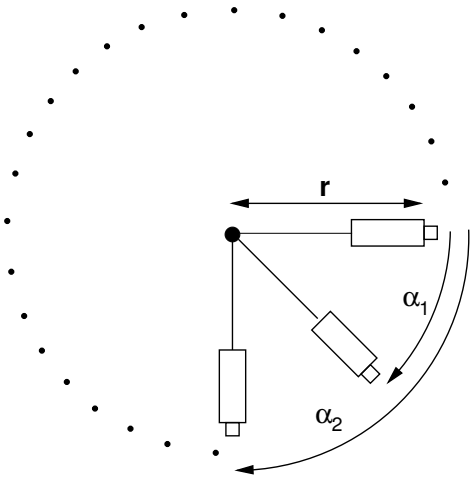


**Figure 2.** Initial imaging geometry of a circular imaging block according to definition.

This type of imaging design does not guarantee ideal measuring geometry, neither does it avoid all the possible occlusions. Usually, multiple image blocks, imaging stations, of this kind must be taken to satisfy the condition of reconstructing the whole object. Unlike the case with panoramic images, 3D measurements can be made from a single image sequence, displacement between projection centres do exist. This method provides measurements that are sufficient for

object reconstruction, or which are a good base to be used in a design of more precise measurements in complex modelling conditions.

Benefit of using circular imaging blocks include fast data acquisition and, also, in the case of video imaging, the recording of increased amount of data. The increased amount of data can be used for substituting the low quality of images to some extent. By using low-cost tape recording devices, the provision of sufficient storage space is rarely a problem. If a video camera is used, all images in a sequence can be used to reconstruct the object instead of selecting the images with the best geometry. The development of digital still cameras and digital storage devices has opened new perspectives on the use of digital imaging. The capacity of storage devices for digital images is nowadays sufficient, while better spatial resolution gives an advantage in using digital cameras over video devices, where the resolution of images is restricted by video standards (PAL, NTSC etc).

### 3.1.2 Image Block Construction

It is important that the circular imaging sequence is closed, since the local coordinate system will be created based on the observations from the imaging sequence. That means that no control point network, or measurements for camera pose, are required. The enclosure of imaging works as in a geodetic leveling chain; the height difference of two points are measured twice, preferably on different routes, closing at the start point. Instead of adjusting measurements directly, in the case of image observations, the adjustment is based on observation equations of indirect observations. The coordinate system is defined by fixing one point and two directions. The navel point of revolution functions as the origin and two coordinates axes of the orthogonal coordinate system are the normal vector of plane rotation and it's orthonormal vector containing the centre of projection of the first camera pose in sequence. However, some scale measurements are required to create a coordinate system in the metric world.

The restricted imaging arrangement forces the projection centres of each camera position to lie on the same plane and within the same distance $r$ from the navel point. From the point of view of 3D measurements, a circular imaging block is perhaps not the perfect imaging configuration for the task. In imaging design, the camera is looking outward from the navel point, as in Figure (2). The consecutive camera positions will then have diverging optical axes. The impact of observations of images with divergent image geometry is a decrease of reliability of the camera orientation parameter estimates. The solution is to turn the camera to the tangential direction of the circle path, Figure (3).

Still, the optical axes of the subsequent images will be divergent. By constructing two such circular imaging blocks on the same tripod position with a difference in camera orientation, better geometry can be achieved. Between image sequences, the camera is turned $180^\circ$ at the end of the bar, as shown in Figure (4). These two

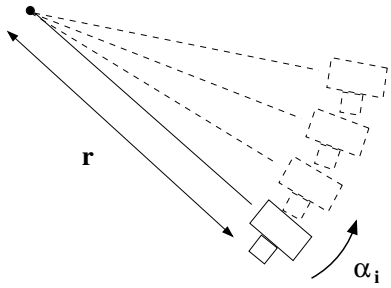


**Figure 3.** Circular imaging block geometry with camera turned to tangential direction

image blocks are co-centred and coexist in the same coordinate system. The object point can be seen in images from both image blocks, and the camera optical axis on the first block images is convergent with camera positions on the second block. Now the imaging geometry with respect to the previous case has substantially improved. Images of this pair of image blocks will be, at most, two times as far from each other as the length of the bar. This is the imaging geometry used in this work and implemented for the experiments. Imaging geometry resembles the implementation depicted is Section 1.3.1 and comparison with methods presented in Section 1.3.1 will be made later in this Chapter.

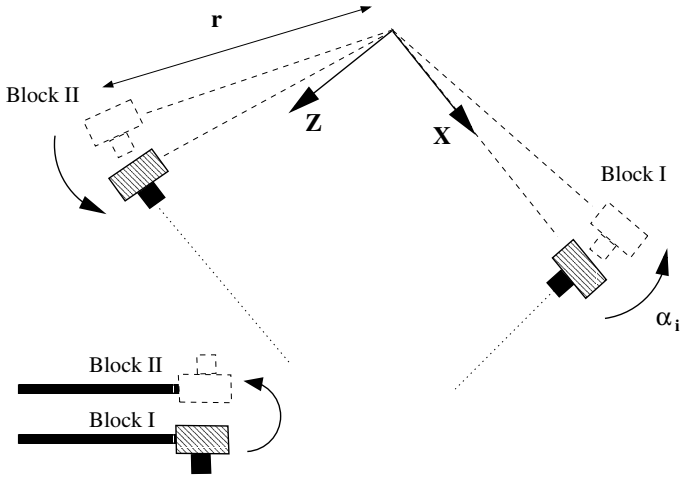


**Figure 4.** Two co-centric circular imaging blocks. The imaging geometry used in this thesis.

From the photogrammetric network design point of view, the ZOD-level of design is very much simplified with circular imaging blocks. The datum problem is solved by creating an "own" coordinate system, while the scale for the network is based on simple distance measurement between two or more 3D points. The FOD-level design consists of the selection of tie points from images and the length $r$ of the bar used. The selected tie points can be image points of natural features or targeted points. Using targeted points means extra work, but improvement

of measuring accuracy also improves the precision of block estimates. In most cases, especially when the image plane is chosen to be perpendicular to the plane of rotation, it is desirable to select points from the side areas of the images. This is because geometrically they have most resolving power in determining the orientation angles of images. The reason why it is favorable to have the image plane near perpendicular to the plane of rotation, and one of the image plane axes parallel to the rotation plane, is that the corresponding points between subsequent images will then most likely be found in the overlapping area. In the opposite case, the overlapping area will be decreased because of gaps between subsequent images. The same phenomenon is known in aerial photography as drift, when the airplane is turned away from the flying direction.

The optimum choice of length $r$ is mainly dependent upon mean object distance. The bounding values for $r$ will be restricted by real imaging circumstances; construction of a stable rotation system is compromised due to too large a radius $r$. The choice of the incident angle of the camera optical axes and the camera position angle was chosen earlier to be $90^\circ$ i.e. tangential direction. This is a reasonable choice in the case of using two co-centric circular imaging blocks for measurements.

The photogrammetric network design problem is substantially simplified in this imaging model. The effect of different choices of circular imaging block parameters on 3D object estimates is discussed in Chapter 4. This kind of approach is applicable in modelling tasks where there is no reference system nearby and the camera station configuration is difficult to design or build.

## 3.2 Estimation of the Model from a Circular Imaging Block

In order to determine object point coordinates, the exact orientation of the camera at the time of exposure has to be solved with respect to the chosen coordinate system. Since the coordinate system will be created from scratch without any coordinate reference system, the only observations included are image observations. The only á priori information which is taken into account is one or more object point distances. Those distances can be considered as observations or they can be seen as a constraint between coordinates of object point pairs. The purpose of scale measurement is to obtain object reconstruction in metric units.

Since the coordinate system is partially based on a predefined movement of the camera, it is logical to solve the camera orientations simultaneously. In order to ensure the accuracy of object reconstruction, *over-determination* (i.e. making more observations than the minimum requirement) is exploited. By using over-determination, it is also possible to assess the precision and reliability of object measurements plus the quality of measurements. Due to over-determination, adjustment of observations is required. As mentioned in Section 2.1, the overdetermined problem solved with an LSQ estimation has proved to be statistically

rigorous and therefore, in the discussion of the estimation model further on in this thesis, the use of the least squares model is assumed.

## 3.3 Perspective projection

The camera model expected here is based on a central perspective camera model. So the mathematical model of 3D-to-2D transformation is a perspective projection. The coordinate transformation from 2D to 3D image space will then be in the form:

$$P_{obj} = P_{prj} + \lambda^{-1} R^T p_{img} \tag{13}$$

$P_{obj}$ denotes a 3D point coordinate vector and $P_{prj}$ the camera projection centre coordinates in the chosen coordinate system in Equation (13). The 3D rotation matrix $R$ is assumed to be orthonormal and the image coordinate observation vector $p_{img}$ is supposed to be image centre coordinates. The scalar $\lambda$ is a scale factor between 3D and 2D image spaces. The inverse transformation derived from Equation (13) yields:

$$\begin{bmatrix} x_i \\ y_i \\ -c \end{bmatrix} = \lambda \begin{bmatrix} r_{11} & r_{12} & r_{13} \\ r_{21} & r_{22} & r_{23} \\ r_{31} & r_{32} & r_{33} \end{bmatrix} \begin{bmatrix} X_{obj} - X_0 \\ Y_{obj} - Y_0 \\ Z_{obj} - Z_0 \end{bmatrix} \tag{14}$$

Explicit in Equation (14) is that the three points $P_{prj}, P_{obj}$ and $p_{img}$ are collinear. That is the reason why it is widely called the collinearity condition. The linear equation system in Equation (14) can also be written as two separate equations, where the scale factor $\lambda$ will be eliminated:

$$\begin{aligned} x_i &= -c \, \frac{r_{11}(X_{obj} - X_0) + r_{12}(Y_{obj} - Y_0) + r_{13}(Z_{obj} - Z_0)}{r_{31}(X_{obj} - X_0) + r_{32}(Y_{obj} - Y_0) + r_{33}(Z_{obj} - Z_0)} \\ y_i &= -c \, \frac{r_{21}(X_{obj} - X_0) + r_{22}(Y_{obj} - Y_0) + r_{23}(Z_{obj} - Z_0)}{r_{31}(X_{obj} - X_0) + r_{32}(Y_{obj} - Y_0) + r_{33}(Z_{obj} - Z_0)} \end{aligned} \tag{15}$$

In Equation (15) the $r_{ij}$ denotes an element of orthogonal rotation matrix $R$. The 3D rotation matrix $R$ is an orthonormal matrix, which is uniquely defined by three independent rotation angles $\omega, \phi, \kappa$:

$$R = \begin{bmatrix} \cos\phi\cos\kappa & \cos\omega\sin\kappa + \sin\omega\sin\phi\cos\kappa & \sin\omega\sin\kappa - \cos\omega\sin\phi\cos\kappa \\ -\cos\phi\sin\kappa & \cos\omega\cos\kappa - \sin\omega\sin\phi\sin\kappa & \sin\omega\cos\kappa + \cos\omega\sin\phi\sin\kappa \\ \sin\phi & -\sin\omega\cos\phi & \cos\omega\cos\phi \end{bmatrix} \tag{16}$$

This type of rotation matrix, Equation (16), is proved to be statistically most rigorous when combined with redundant observations and an LSQ estimation (Cooper and Robson 1996). The rotations $\omega, \phi, \kappa$ of the coordinate axes $x, y, z$, respectively, are assumed to have positive direction on clockwise rotation while looking from the origin along the direction of the respective coordinate axes.

The disadvantage of such a parameterization of the rotation matrix is that the observation equation, Equation (1), presented in Section 2.1 becomes non-linear. Non-linearity of the function can be solved by linearizing the equation and solving parameters with iterative methods. Then, however, the initial values for parameters have to be obtained. This characteristic of the transformation model has restricted its use in many real-time applications. Because in this research the rigorousness of the solution is favored over the speed of computation, the non-linear projection model is used.

## 3.4 Camera model

The camera coordinate system is defined as a right handed, orthonormal 3D coordinate system. The origin of the coordinate system is in the projection centre of the camera and the image plane is positively oriented, i.e., it lies between projection centre and object. In the previous section, the perspective projection was based, essentially, on a pin-hole camera model. This is an ideal model of light traveling from a 3D object point through the projection centre into the image plane along a straight line. Unfortunately, this is not the case in reality, when light has to penetrate through the lens system onto the image plane. A description of light traveling inside the camera is called the interior orientation.

The discrepancies of this ideal model can be divided into linear and non-linear components. In order to accomplish precise photogrammetric measurements, these errors have to be eliminated or their effect on measurements have to be compensated. The process of determining these systematic errors is called *camera calibration*.

The deformations are due to many different error sources. The non-perpendicularity of the optical axis and image plane cause coordinate axes of the image plane to be non-orthogonal and so there can be a scale difference between the $x$- and $y$-axes. Also, non-linear deformation will be observed, but the amount of deformation usually is so small that only linear components are considered. The scale difference can also be an effect of the aspect ratio of a pixel and non-orthogonality of the effect of the misorientation of sensor elements in rows and columns in the case of a digital sensor.

In calibration, the location of the projection centre with respect to the image plane is described by the principal point coordinates $x_p$ and $y_p$. The perpendicular distance of the projection centre from the image plane is then expressed by the camera constant $c$. The scale difference is usually expressed by one number $a$, which

models affinity. The non-orthogonality of image coordinate axes, or skew, can be determined by one value $b$. The non-orthogonality $b$ can also be written with the help of angle $\theta$, which denotes the discrepancy in orthogonality and affinity $a$ as $b = a \tan\theta$ (Niini 2000). The camera centred image coordinates after the correction of linear distortions can be then given as

$$\begin{cases} x_l = x_i - x_p + b\,(y_i - y_p) \\ y_l = a\,(y_i - y_p) \end{cases} \tag{17}$$

In Equation (17) $x_l$ and $y_l$ denotes the camera centred and linear distortion corrected image observations. The non-linear components of interior orientation mainly are caused by the camera lens system. When light comes from object points to the image plane, it has to go through an optical lens system with several lenses that will change the direction of the light beam systematically due to different lens materials or misalignment of these lenses. This distortion is observed to be non-linear. The distortion model can be divided into radial and decentring distortion. Radial distortion causes image points to move away from the principal point (pincushion distortion) or toward the principal point (barrel distortion). This distortion is known to be circular symmetric in respect to the point of best symmetry. This distortion can be modelled by a third degree of polynomial (Brown 1971):

$$\begin{cases} x' = x_i + (x_i - x_p)(k_1(r_c^2 - r_0^2) + k_2(r_c^4 - r_0^4) + k_3(r_c^6 - r_0^6)) \\ y' = y_i + (y_i - y_p)(k_1(r_c^2 - r_0^2) + k_2(r_c^4 - r_0^4) + k_3(r_c^6 - r_0^6)) \end{cases} \tag{18}$$

Here, $r_c = \sqrt{(x_i - x_p)^2 + (y_i - y_p)^2}$, and $r_0$ denotes the radial distance from the point of best symmetry, see Equation (18). The radial distortion is zero in the point of best symmetry, but it can be forced to be zero in any freely-chosen radius $r_0$. The different choice of $r_0$will have an effect on the values of coefficients and camera constant, but the total effect of changed parameter values will compensate the radial distortion equally well (Brown 1971).

The decentring distortion is caused by an improper alignment of lens elements in a compound lens system, with its correction being given as (Brown 1966):

$$\begin{cases} x'' = x_i + 2p_2(x_i - x_p)(y_i - y_p) + p_1(r_c^2 + 2(x_i - x_p)^2) \\ y'' = y_i + 2p_2(x_i - x_p)(y_i - y_p) + p_2(r_c^2 + 2(y_i - y_p)^2) \end{cases} \tag{19}$$

Normally, in camera calibration, all these parameters are determined simultaneously. Niini (Niini 2000) points out in his investigations that lens distortions should be taken into account before the distortion raised in the imaging media is corrected. This is because the lens distortions occur before the light beam is

exposed to other distortions. In practice, this means substituting the $x_i - x_p$ and $y_i - y_p$ observations by their corrected values $(x_l, y_l)$ in Equation (18) and Equation (19) and solving the corrections to linearly distorted coordinates. This substitution yields to an iterative solution of calibration parameters. Niini, however, discovered that, if the effect of radial distortion is less than 60 pixels in size (with the camera in question), the difference of these estimation models is less than unit measurement precision, here expected to be 0.05 pixels. The difference can especially be seen with devices that have substantial affine distortion, like video cameras. But even with video cameras, the effect of lens distortion is unlikely to be greater than the mentioned bounding effect. Since we are not primarily interested in the actual values of calibration parameters, but more in the ability to compensate distortions of image observations, we can safely use the following correction model, where all camera-calibration parameters are solved simultaneously:

$$\begin{cases} x_{corr} = x_l + x_l r_{cl}^{-1}(k_1 r_{cl}^3 + k_2 r_{cl}^5 + k_3 r_{cl}^7) + p_1(r_{cl}^2 + 2x_l^2) + 2p_2 x_l y_l \\ y_{corr} = y_l + y_l r_{cl}^{-1}(k_1 r_{cl}^3 + k_2 r_{cl}^5 + k_3 r_{cl}^7) + p_2(r_{cl}^2 + 2y_l^2) + 2p_1 x_l y_l \end{cases} \quad (20)$$

where $r_{cl} = \sqrt{x_l^2 + y_l^2}$ , see Equation (20). Other sources of non-linear distortion might be due to a discrepancy of sensor or imaging media from the rectangular flat image plane. In the case of film, the deformation of the media can occur at the time of exposure if the film is not precisely in contact with the image plate. The non-linear deformation of film can also be a result of the developing process or film-storage environment. With digital sensors, the non-linear deformation can be considered as a manufacturing imperfection. Sensor elements in a CCD array might not be perfectly lined up or they might not be evenly spaced. The flatness of the sensor array might also be compromised.

The non-linear deformations of the imaging media are quite difficult to model. Usually some polynomial functions have been applied in order to compensate for the effect of these anomalies on image observations. The problem with high-order polynomials is that they require a substantial number of measurements to be made in order to be precisely defined. For this reason, réseau grids with known image coordinates have been used with film cameras. In modern digital sensors, the non-linearity has been considered so small compared to the image observation accuracy that it has been ignored. In addition, the non-orthogonality component has been found to model the deformation of digital sensor irregularities also. In addition, the instability of the sensor location inside the camera has been noted (Shortis et al. 1998, 2001). The calibration unknowns can be divided into block-invariant and -variant parameter. Meaning that block-variant parameters (e.g. principal point coordinates) are independently derived for each exposure and all other calibration parameters are in common for all exposures in image block. This approach is good for cases where imaging geometry is adequate for self-calibration. An improved procedure is suggested, where block-invariant parameters are defined with help of finite element correction grid (Hast-

edt et al. 2002). In this model also unflatness of sensor can be defined. However, if self-calibration is not appropriate for the task, this stability problem has to be taken care of with practical means, such as frequent calibration, or ensuring physically stable CCD chip positioning in the camera body.

In this research, the linear and non-linear deformations are expected to be corrected based on pre-calibration of the camera. Self-calibration by including intrinsic camera parameters in a circular imaging block-adjustment can also be applied, but, due to restricted imaging geometry, determination of all calibration parameter values is not feasible. The determination ability also depends very much on the object point distribution.

## 3.5 Estimation Problem, Approach I

We can see the estimation problem as $n-1$ number of relative orientations, or even $n$ number, if we include relative orientation between the first and last image in sequence. By choosing the model of independent stereo models, we can avoid resolving the object point unknowns. To do so is advantageous, since we are primarily interested in image locations and orientations in an image block. The idea behind this prioritization is that we first want to get the image block and coordinate system created. Then we carry out measurements on images in order to reconstruct objects as in the ordinary mapping process, rather than targeting all object points needed to reconstruct the object and resolve object points simultaneously with block parameters.

Alternatively, we can end up using the bundle block estimation and applying the collinearity condition. Then we will have $n$ number of exterior orientations to be solved. The unfortunate situation is that now we have to assign initial values for all of our tie points, because of the non-linear model.

In both cases we have a datum that is insufficient. We can apply a free-net type approach and use a minimum norm solution or we can fix some parameters in order to get the datum to become sufficient. We do not expect to have any exterior points known in any coordinate system. As mentioned in Section 3.1.2, we create a local coordinate system on site for our measurements. By selecting the navel point of the image block as an origin, and fixing the $x$-axis of a defined coordinate system in the direction of the first image projection centre while the rotation-plane normal assigns the second direction of the orthogonal coordinate system, the datum problem will be solved.

As the camera is rotated around the origin, the orientation will change with respect to the coordinate system, but the angle between the image plane and position vector of the projection centre will stay constant. By applying this knowledge, and the fact mentioned earlier that all projection centres $P_i$ lie on the path of the same circle, we can set constraints to stabilize the estimation process.

$$|P_i| = r \tag{21}$$

$$\sqrt{X_i^2 + Y_i^2 + Z_i^2} = r \tag{22}$$

Equations (21) and (22) state that all projection centres are at the same distance $r$ from the navel point, but this does not say anything about them lying on the same plane. This can be expressed by setting a constraint between the projection centres and a normal vector $\eta$ of the rotation plane:

$$P_i \bullet \eta = 0 \tag{23}$$

We can also consider $\eta$ as a new parameter vector to be estimated. By giving a large weight in the LSQ estimation for this observation equation we can force the system to retain this condition, given in Equation (23). The constant angle between the position vector of the projection centre and the optical axis of the camera can be forced by adding the following constraint in estimation:

$$R_i \begin{bmatrix} 0 \\ 0 \\ 1 \end{bmatrix} \bullet \frac{P_i}{|P_i|} = constant \tag{24}$$

In Equation (24), $R_i$ denotes the orthonormal rotation matrix of the $i^{th}$ image in sequence and $P_i$ the equivalent projection centre position vector. By using independent stereo models and a coplanarity condition, there will be $n \times 5 + 5$ unknown parameters ($r$, $\eta$ and *constant* value are included as unknowns) or $n \times 5$ unknowns plus $n \times 3$ constraint equations. With the bundle of rays model, we will end up to $6 \times n + 4$ plus $m \times 3$ unknown parameters, where $m$ denotes the number of tie points. Since stereo models are based on the coplanarity of corresponding image rays and base vector, no explicit observation function can be written where only one observation is involved. This leads to the construction of the condition equation and the general adjustment model (Mikhail 1976):

$$\begin{cases} B(l + v) + Ax = f \\ Cx = g \end{cases} \tag{25}$$

where the matrix $B$ denotes the coefficient matrix of observations and the matrix $C$ contains the constraint conditions, see Equation (25). The bundle of image rays model is based on the collinearity condition and explicit observation equations.

The equation is equivalent to Equation (1) with the addition of constraints, see Equation (26).

$$\begin{cases} Ax = v + l \\ Cx = g \end{cases} \tag{26}$$

## 3.6 Estimation Problem, Approach II

The image block estimation based on the bundle of rays model can also be written by using a different set of parameters. As we are not using any exterior control points, but are constructing our own coordinate system, we can make some assumptions. As we have already defined the origin to be the navel point of revolution and the $x$-axis to be in the direction of the first photo projection centre, we can also state that the projection centre of the camera in different camera poses will lie on a plane parallel to a coordinate plane. We can choose the $y$-axis to point upwards so that all projection centres will lie on the $xz$-plane. This choice is as good as any other, and widely used in terrestrial photogrammetric networks (Slama 1980). Now we can fix the $y$-coordinate of all projection centres to be a constant and express the $x$- and $z$-coordinates in a polar coordinate system instead of Cartesian coordinates:

$$\begin{cases} X_i = r \cdot \cos \alpha_i \\ Y_i = constant \\ Z_i = r \cdot \sin \alpha_i \end{cases} \tag{27}$$

Now we do not need to put any constraints to force parameter values of the projection centres to lie on a plane nor to be at a distance of $r$ from the centre of revolution, because all this information is included in Equation (27). What we have not yet included in the model is the constant angle between the optical axis of the camera and the position vector of the projection centre. In a special case where we have zero tilt $\omega_0$ and spin $\kappa_0$ angles, our rotation matrix differs from the first camera rotation matrix $R_{\omega_0,\phi_0,\kappa_0}$ only by the difference $R_{\omega_0,\phi_0-\alpha,\kappa_0}$. (Note that the $\phi$ increases in the opposite direction to $\alpha$). More generally, the rotation of the camera by $\alpha_i$ can be expressed in a 2D rotation on the plane:

$$R_{\omega_i,\phi_i,\kappa_i} = R_{\omega_0,\phi_0,\kappa_0} \cdot R_{\alpha_i} \tag{28}$$

where,

$$R_{\alpha_i} = \begin{bmatrix} \cos \alpha_i & 0 & -\sin \alpha_i \\ 0 & 1 & 0 \\ \sin \alpha_i & 0 & \cos \alpha_i \end{bmatrix} \tag{29}$$

The elements of the $R_{\omega_i,\phi_i,\kappa_i}$ will then be:

$$\begin{cases} a_{11} = \cos\alpha\cos\phi\cos\kappa - \sin\alpha\sin\phi \\ a_{12} = \cos\alpha\left(\cos\omega\sin\kappa + \sin\omega\sin\phi\cos\kappa\right) + \sin\alpha\sin\omega\cos\phi \\ a_{13} = \cos\alpha\left(\sin\omega\sin\kappa - \cos\omega\sin\phi\cos\kappa\right) - \sin\alpha\cos\omega\cos\phi \\ a_{21} = -\cos\phi\sin\kappa \\ a_{22} = \cos\omega\cos\kappa - \sin\omega\sin\phi\sin\kappa \\ a_{23} = \sin\omega\cos\kappa + \cos\omega\sin\phi\sin\kappa \\ a_{31} = \sin\alpha\cos\phi\cos\kappa + \cos\alpha\sin\phi \\ a_{32} = \sin\alpha\left(\cos\omega\sin\kappa + \sin\omega\sin\phi\cos\kappa\right) - \cos\alpha\sin\omega\cos\phi \\ a_{33} = \sin\alpha\left(\sin\omega\sin\kappa - \cos\omega\sin\phi\cos\kappa\right) + \cos\alpha\cos\omega\cos\phi \end{cases} \tag{30}$$

Since the rotation angles $\omega_i$,$\phi_i$,$\kappa_i$ depend on the first image rotation matrix by the angle $\alpha_i$ and projection centre coordinates of a single camera position are dependent on the values of $r$ and $\alpha_i$ , there is no need to estimate these dependent parameters. Instead, the collinearity Equation (15) can be written according to these independent parameters as

$$\begin{cases} x = -c\,\dfrac{a_{11}(X_{obj} - r\cos\alpha_i) + a_{12}(Y_{obj} - h) + a_{13}(Z_{obj} + r\sin\alpha_i)}{a_{31}(X_{obj} - r\cos\alpha_i) + a_{32}(Y_{obj} - h) + a_{33}(Z_{obj} + r\sin\alpha_i)} \\ y = -c\,\dfrac{a_{21}(X_{obj} - r\cos\alpha_i) + a_{22}(Y_{obj} - h) + a_{23}(Z_{obj} + r\sin\alpha_i)}{a_{31}(X_{obj} - r\cos\alpha_i) + a_{32}(Y_{obj} - h) + a_{33}(Z_{obj} + r\sin\alpha_i)} \end{cases} \tag{31}$$

This nonlinear observation equation, Equation (31), is then linearized with respect to the first image rotation angles $\omega_0, \phi_0, \kappa_0$, radius $r$ and the angle $\alpha_i$, $i = 1, 2, .., n$. Also, object point coordinates are expected to be unknowns and linearization is to be carried out with respect to those object parameters $X_{obj}, Y_{obj}, Z_{obj}$ as well. Value $h$ is some arbitrary constant. The result of linearization is presented in Appendix I. It is essential to notice that all image observations from all images have an effect on the determination of the first image orientation angles $\omega_0, \phi_0, \kappa_0$ and radius $r$. All camera orientations are dependent on those parameter values and therefore they can be considered as common parameters of the image block. Now, the total number of image unknowns will be $4 + n$. The assumption of the first image projection centre to be in the direction of the $x-$axis means that $\alpha_1$ will be fixed to zero and the number of unknowns reduced by one to $4 + n - 1$. The total number of unknowns is then $4 + (n - 1) + m \times 3$. The effect of one image observation on the normal matrix $N$ is depicted in Figure (5).

It can be seen that the number of unknown block parameters is less than with using the parameter set presented in Section 3.5. Also we can avoid the use of constraint equations. Exterior orientation parameters of dependent camera poses can easily be derived back to standard presentation in a Cartesian coordinate system by applying Equations (27) and (28).

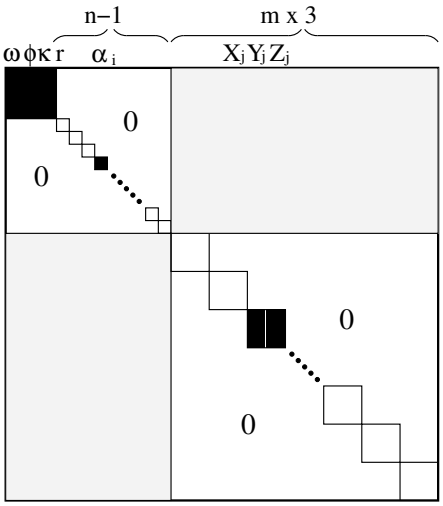


**Figure 5.** Effect of one image observation on normal matrix.

It was mentioned earlier that point intersection would be poor unless we do not use image observations from a second co-centric image block. The difference between these two coordinate systems is only an angle between their $x-$axes. So the angle can be estimated from observations of common points.

With a single block estimation, we can find that the same geometrical problem will appear. The intersection angle of image rays for the unknown 3D tie point will be rather small, as shown in Figure (6). So, the position accuracy for such a point is questionable. Even though those tie points are not to be used for modelling purposes, the unreliability of these observations also affects the determination of camera orientation.

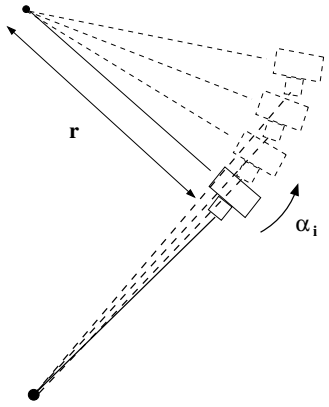


**Figure 6.** Poor intersection geometry.

Based on this aspect, both image blocks must be estimated simultaneously. This way we can obtain good observations from convergent images, as depicted in

Figure (4). The number of additional unknowns with respect to photo parameters is $4 + n_2$. The first four unknown parameters consist of rotation angles of the first camera position on the second block and radius $r_2$ of the second circular imaging block. The angle $\beta_1$ (equivalent to $\alpha_1$in the first block) is an angle between the first image projection centre and the $x$-axis. It is to be emphasized that both blocks are to be bound into the same coordinate system and therefore all camera rotations $\beta_i$ , when $i = 1, 2, 3, ...n_2$, are measured from the $x$-axis. The number of tie points does not need to increase much as both sequences will include more or less the same scenery. The tie points are expected to be observed from both image blocks since otherwise the geometry of intersection will be poor.

The assumption made is that the camera is turned by $180°$ at the end of the supporting bar, as suggested in Section 3.1.2 and shown in Figure (4). The camera projection centres will still be on the same $xz$-plane as the first image block. Otherwise correction for the height, or more precisely $y$-coordinate difference, has to be introduced for the projection centre coordinates of the second block.

As we will construct our own coordinate system, and as we do not have any exterior knowledge, we have to have a scale for our measurements. Distance measures can be included in the estimation as a constraint equation or as a normal observation with a large weight. For defining scale for the measurements, we can include a distance measure between object points $p_i$ and $p_j$ as an observation equation in the form of Equation (32).

$$\sqrt{(X_i - X_j)^2 + (Y_i - Y_j)^2 + (Z_i - Z_j)^2} = d_{ij} \tag{32}$$

The model presented here resembles the imaging model of *omnivergent stereo* (Seitz et al. 2002) and *stereo panoramas* (Peleg and Ben-Ezra 1999). In both cases, the objective is to reconstruct image mosaics, where the object point can be seen in two panorama images having image rays with convergent angles. Imaging is assumed to comply strictly with the imaging model; no variation is allowed. In contrast to those approaches, in this research the measurements are to be made from multiple perspective projected images and the objective is to exploit the over-determination and bundle method in object measurements. Also, determination of the exact orientation of the camera at the individual time of exposure is the purpose of multiple image observations. In both the omnivergent stereo and stereo panoramas methods, the goal is to reduce the redundant information in the image sequence and exploit the epipolar geometry and stereo matching algorithms. Also, aspects of the accuracy of object measurements have not been treated in these two models.

## 3.7 Image Block Estimation

The mathematical model used is based on image bundle blocks and a collinearity condition. An alternative method would have been to use independent stereo models as primary computation units. It is true that block adjustment based on stereo models and a coplanarity condition does not include unknown 3D object points in the estimation, which was stated earlier. But, thinking geometrically, those unknown points are still there, and in the case of a bundle of rays one can always eliminate the unknown 3D points from a LSQ type estimation by creating a reduced normal matrix (Mikhail 1976; Mikhail et al. 2001). The design matrix $A$ and normal matrix $N$ can be partitioned in respect to orientation unknowns and object coordinate unknowns as follows:

$$A = [A_1 A_2] \tag{33}$$

$$N = A^T A = \begin{bmatrix} A_1^T A_1 & A_1^T A_2 \\ A_2^T A_1 & A_2^T A_2 \end{bmatrix} = \begin{bmatrix} N_{11} & N_{12} \\ N_{21} & N_{22} \end{bmatrix} \tag{34}$$

$$\begin{bmatrix} N_{11} & N_{12} \\ N_{21} & N_{22} \end{bmatrix} \begin{bmatrix} x_1 \\ x_2 \end{bmatrix} = \begin{bmatrix} b_1 \\ b_2 \end{bmatrix} \tag{35}$$

The design matrix $A$ is partitioned into two sub-matrices where the columns of the matrix represent the coefficients of the image orientation or 3D point coordinate values as depicted in Equation (33). By using a similar notation, the solution vector can also be divided into two parts $x_1$consisting of the parameter values of exterior orientation parameters and $x_2$ the 3D point coordinate values, respectively, see Equations (35). The normal matrix $N$ can then be reduced to the size of the sub-matrix $N_{11}$ of the original normal matrix (Mikhail 1976):

$$\left(N_{11} + N_{21}\, N_{22}^{-1}\, N_{12}\right)\; x_1 = b_1 - N_{21}\, N_{22}^{-1}\, b_2 \tag{36}$$

The notation $b_1$ and $b_2$ are result of corresponding partition of right-handside of the normal equation in Equation (36). By using the linear model, we do not need to re-eliminate the 3D point unknown parameters, but, since we have chosen to use a nonlinear type model, we are forced to resolve corrections to approximations of point unknown parameters also. The back substitution to obtain $x_2$ in given as

$$x_2 = N_{22}^{-1}(b_2 - N_{21}x_1) \tag{37}$$

Equation (37). The idea of eliminating the unknown point parameters from the estimation is beneficial. Since we are going to have numerous images included in a single circular imaging block, we will most likely have numerous unknown 3D points as well. In standard close-range block adjustments, we usually eliminate the image parameters from the normal matrix in cases where we have numerous images, since one image increases the diagonal element of the normal matrix by six. In this model, one additional image increases the number of unknown parameters by one, but one additional 3D point increases the number of unknowns by three. Also, in the case of convergent imaging, the same object point can be seen in multiple images, sometimes even from all of them. In circular imaging, the scene from image to image changes, and one point can be seen only from a small subset of images, therefore the number of tie points increases significantly.

As the normal matrix $N$ can be updated sequentially by observation equations, there is no need to construct the design matrix $A$ at all. Also, the unknown parameters can be eliminated sequentially. So the elimination can be performed point-by-point. Although we have to take care that all observations attached to that point are updated consecutively to the sub-matrix of $N_{12}$ and $N_{22}$. After this, the reduced normal matrix can be updated by using Equation (36) and we can continue by processing the observations of the next point. The number of steps to construct the reduced normal matrix does not differ much from the number of steps used to construct the original $N$. Calculating the back substitution increases the number of steps, but the computing time in this task is very short compared to the time spent for computing the LSQ solution for a large normal matrix $N$.

# 4 SIMULATION

The most desirable outcome of a photogrammetric measuring system is the ability to create a consistent and reliable model of the object scene. The highest attainable accuracy of object measurements can be evaluated by the use of simulation. Simulation is a tool to verify the correctness of a mathematical model in an artificial situation, sometimes due to unknown situations, lack of experience, or to reproduce essential features or characteristics of a phenomenon. Often the objective is to provide the circumstances that are as close as possible to those of a real situation. In this research, the basic measuring conditions are maintained throughout testing while only one parameter value of the system at one time is altered in each experiment. Due to this alteration of multiple variables, the impact of change of an individual parameter value on object measurements is hard or unreliable to determine. In many cases, the unreliability of assessment is due to a high correlation of individual parameter values.

In simulations carried out in this research, the maintained conditions were: *the number and distribution of object points* in a scene; *the camera model* used; and *the orientation of camera with respect to the supporting bar*. The object point set used in the simulations was computer generated, consisting of $200$ object points. The object distance from the origin varied from two to fifteen meters and the mean object distance was about eight meters. Generation of the point set was accomplished by using a random number generator to generate a normal distributed dataset. The only restriction for object point generation was that object points were allowed to be situated not farther off than the maximum distance and not closer than the minimum distance. Also, it was ensured that all points fitted the height range according to the field of view of the used camera model. This was to guarantee object points would be visible on images of the fictitious image block.

The camera geometry was chosen to be $1024 \times 1280$ pixels with a camera constant of $1400$ pixels. This camera model resembles the geometry of the real camera *Olympus Camedia C-1400L*, which was available at that time at the institute where the research was carried out. The pixel resolution and field of view have an effect on object measuring accuracy as well. Testing the measuring accuracy with different camera geometries could have been one test option, but, as the choice of camera cannot be considered to relate particularly to this photogrammetric measuring method, only one camera model was used. Since no prominent camera geometry on terrestrial imaging can be assigned, this selection can be considered as good as any other choice. The pixel size of this particular camera model was announced by the manufacturer to be $25.4\mu m$ and was used in converting the pixel noise level values to corresponding values in micrometers in Tables (1) and (2).

The orientation of the camera with respect to the plane of rotation, and the direction of the camera optical axis with respect to the rotation path, were kept

constant. The optical axis of the camera was parallel to the plane of rotation and also tangential to the circular path of projection centres during the rotation. The rotation angles of the camera in the first camera pose in the first image block were therefore $\omega = 0, \phi = 0, \kappa = 0$ and for the second block $\omega = 0, \phi = 180°, \kappa = 0$. Otherwise, the camera was rotated around a fixed rotation point with equal angular steps in the fictitious image block, i.e., only the $\phi$-angle was changed. It is to be noted that the $y$-axis was parallel with the normal vector of the rotation plane.

Simulated image observations were created by back-projecting those 3D object points, which fitted to the field of view, onto the focal plane in each camera pose. Random noise of some predefined level was added to observations and the adjustment of the block was performed. In adjustment, both image blocks were computed simultaneously with object point coordinates. In addition to these arrangements, one scale observation in the size of two meters was included in the computation.

These arrangements remained the same throughout all simulation tests. In order to attain reliability in terms of statistical variables, $100$ simulation runs were carried out. Statistical parameters as the mean value and variance of block parameters and object coordinates were computed from the results of $100$ simulation runs of tests.

## 4.1 Selection of simulation parameters

The performance of circular imaging blocks can be tuned by changing a few factors in the construction of the block. The accuracy of a final 3D model depends on *accuracy of image observations*, *geometry of imaging network*, *number of observations*, and precision of *camera model*. These are all factors most often mentioned in the literature dealing with the accuracy of close-range photogrammetry (Fraser 1984, 1989; Mason 1995). The effect of image observation accuracy on object parameter determination is apparent. Also, it can clearly be shown with error propagation, how the geometry of intersecting image rays affects object accuracy. An increase in the number of observations above the number that is necessary to solve the object parameters does not only improve the accuracy of object measurements, but also gives us a tool with which to estimate the precision of our measurements without any exterior reference. By applying a correct and precise camera model the occurrence of systematic errors on the object model can be prevented.

In this kind of constrained imaging system, the only factors having an influence on imaging geometry are the length of the used bar and the initial orientation of the camera with respect to rotation. The orientation of the camera has an influence on imaging geometry at close range. Since the object distance in these tests spans over $15m$ the length of the bar will have more effect on the imaging geometry than the orientation. The accuracy of measurements has been simulated by adding some noise on "correct" image observations. The number of observations can only be increased by shortening the angular step between camera

poses in the image block. The correct camera model has an influence on coordinate values, as in any photogrammetric network. In a free-net type photogrammetric network, the incorrect camera model may cause minor effects on object coordinate values, since part of the systematic error will be absorbed in orientation parameter values. In this kind of constrained imaging system especially, the correctness of the camera model has an essential importance, since systematic error is more likely to be present in coordinate values than in constrained orientation parameter values. Nevertheless, in these simulation tests, the camera model is assumed to be correct without any systematic errors.

## 4.2 Noise level

The following procedure was adapted while testing the noise level of the image measurements. This noise level test is to simulate the use of different cameras or object points of different quality. The chosen noise levels were $0.5$, $0.2$, $0.05$ and $0.02$ pixels. The first two cases can be considered to simulate bad and good image measurements of natural object points and the latter two as bad and good observations of targeted object points. The noise levels can also be thought of as cameras of different quality or resolution.

In these simulation tests the radius was a constant $50cm$ and 30 images were included in both image blocks. The object points were back-projected onto the focal plane as image point observations according to the orientation information. The quality of image observations was then degraded by adding normal distributed noise on image coordinate values via a random number generator. In the generation of normal distributed noise, the algorithm depicted in (Knuth 1981) was followed. The noise generated had a zero mean with a standard deviation of $0.5$, $0.2$, $0.05$ and $0.02$ pixels, respectively.

From 100 runs of tests, the mean values and deviation of block parameter and object 3D coordinate values were calculated in each test case. The standard deviation of block parameters have been collected in Tables (1) and (2) and an equivalent presentation of the object coordinate standard deviation is depicted in Figure (7). In Tables (1) and (2), the standard deviation values of $\alpha_i$-angles are averaged mean standard deviations.

| $pix\ (\mu m)$ | $d\omega\ (deg)$ | $d\phi\ (deg)$ | $d\kappa\ (deg)$ | $dr\ (mm)$ | $d\overline{\alpha}\ (deg)$ |
|---|---|---|---|---|---|
| $\sigma = 0.50\ (13.0)$ | 0.02385 | 0.02926 | 0.02060 | 1.13253 | 0.00752 |
| $\sigma = 0.20\ (5.1)$ | 0.01183 | 0.01173 | 0.01016 | 0.47376 | 0.00349 |
| $\sigma = 0.05\ (1.3)$ | 0.00314 | 0.00349 | 0.00269 | 0.10728 | 0.00080 |
| $\sigma = 0.02\ (0.51)$ | 0.00114 | 0.00122 | 0.00098 | 0.04490 | 0.00033 |

**Table 1.** Standard deviations of block parameters, Block I

| $pix\ (\mu m)$ | $d\omega\ (deg)$ | $d\phi\ (deg)$ | $d\kappa\ (deg)$ | $dr\ (mm)$ | $d\overline{\alpha}\ (deg)$ |
|---|---|---|---|---|---|
| $\sigma = 0.50\ (13.0)$ | 0.03340 | 0.03202 | 0.03001 | 1.06836 | 0.04481 |
| $\sigma = 0.20\ (5.1)$ | 0.01639 | 0.01633 | 0.01473 | 0.55887 | 0.01948 |
| $\sigma = 0.05\ (1.3)$ | 0.00434 | 0.00472 | 0.00390 | 0.13908 | 0.00531 |
| $\sigma = 0.02\ (0.51)$ | 0.00158 | 0.00164 | 0.00142 | 0.05589 | 0.00189 |

**Table 2.** Standard deviations of block parameters, Block II

From Table (1), we can see that standard deviation declines first to half and then to $1/10$ and $1/20$ from the first listed values. The linear change in standard deviations with changing $\sigma$ is entirely as predicted and consistent with expectations. The same phenomenon can be seen in Table (2). The only difference between these two tables can be seen in column $d\bar{\alpha}$, where values in Table (2) are slightly higher. That is partly due to the estimation of the angular difference of $x$-axis in the first and second block. This uncertainty of estimate affects the estimates on $\alpha_i$-values in the second block. In the first image block $x$-axis was fixed.

In order to evaluate the tie point accuracy, mean values of point coordinate standard deviations were computed and indexed in respect to 3D point nominal distances from the centre of measurements. Second-order polynomials were then fitted to point distances and coordinate mean deviations. Correspondent graphs of different noise levels are shown in Figure (7).

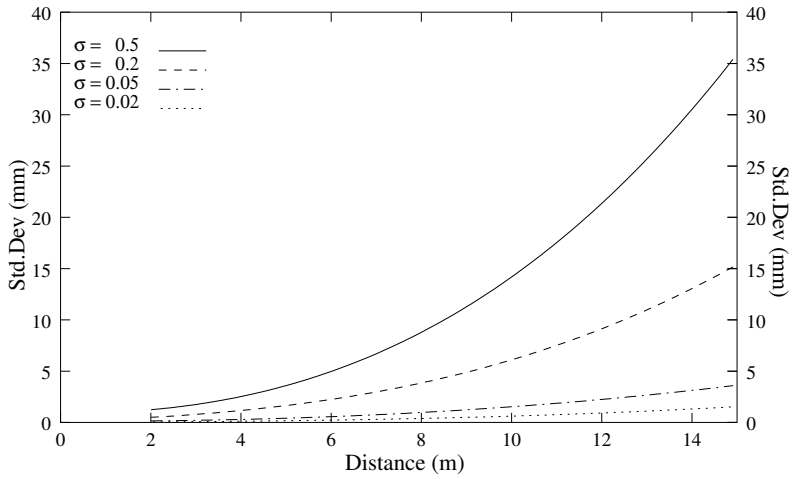


**Figure 7.** Effect of noise on object point accuracy

From Figure (7), the accuracy of such a measuring configuration can be estimated to be $1 : 15000$ for the best case and $1 : 900$ in the worst case. These relative accuracy numbers are derived assuming the maximum dimension of the object to be $30m$. As this imaging system is symmetrical, the maximum distance from the imaging station is then $\leq 15m$.

## 4.3 Length of radius

The length of the bar here has the same meaning as the base length in stereoscopy. In principle, the longer the bar, the better the precision. However, in practice, the imaging environment and mechanical constraints can limit the length of the bar. This can occur when there is only a constricted space for the camera to be rotated or when extending the length; the view will also change, and objects closer to the centre will be out of sight, on most of the images or when the construction of such a rotation system will be too unstable.

Fictitious circular imaging blocks with differing radii were constructed in the centre of a randomly generated object point set. The field of view according to the camera model was $40° - 49°$depending on whether it was evaluated in the direction of $y$- or $x$-axis. In each case, the number of images in a block was $30$. So, in each computation, $67$ block parameters and $606$ coordinate values were subject to estimation. The number of observations depended on the pose of the camera with respect to the object point set. Only those object points that fitted inside the field of view, were back-projected onto the image plane as image observations. The difference in number of observations between the maximum and minimum case was about $1\%$. This variation was due to the change of imaging geometry and can be considered insignificant in terms of redundancy of estimation.

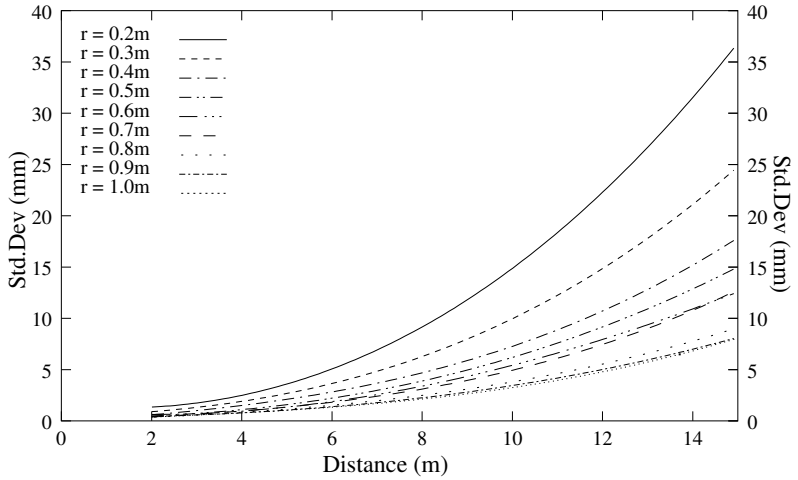


**Figure 8.** Effect of length of radius on object point accuracy

The standard deviations of coordinate values with respect to distance are depicted in Figure (8). The standard deviations were calculated from $100$ simulated test runs with normal distributed noise added at a level of $0.2$ pixels. The polynomial curve was fitted to the data, where the mean coordinate standard deviation was depicted on the ordinate and the distance of the 3D point on the abscissa. A curve was fitted to all data sets of different radii. The result of the simulation showed that the effect was not totally linear. The further the object

points locate, the more significant is the improvement of point precision. After some limit, the extension of the radius did not improve the result significantly. In this case, the limit seemed to be around $80cm$ and was, without question, also dependent on the structure of the object point set and chosen camera model.

## 4.4 Number of photos in block

The change of number of images in a block was also tested in a similar way. Normally, it can be stated that increasing the number of images does not improve the precision much, unless the whole imaging geometry of the photogrammetric network is improved. This holds in traditional networks, where each new camera position brings six new parameters into estimation. In this approach, one new camera position adds only a single parameter $\alpha_i$ in adjustment, while redundancy is essentially larger. This is due to the use of polar coordinates for presenting the projection centres in the formulation of the mathematical model of the circular imaging block. From Figure (9), it can be seen that increasing the number of images and observations improved the precision up to $100$ frames per block, but, after that no significant improvement could be seen. However, whether it is worthwhile to nearly double the number of frames in image processing if the expected accuracy improvement is less than $17\%$, as it is when increasing the number of frames in a block from $30$ to $50$ frames (i.e., from $60$ to $100$ images, totally) should be considered. The amount of additional processing is dependent on the chosen image measuring strategy and has to be assessed in each individual case.

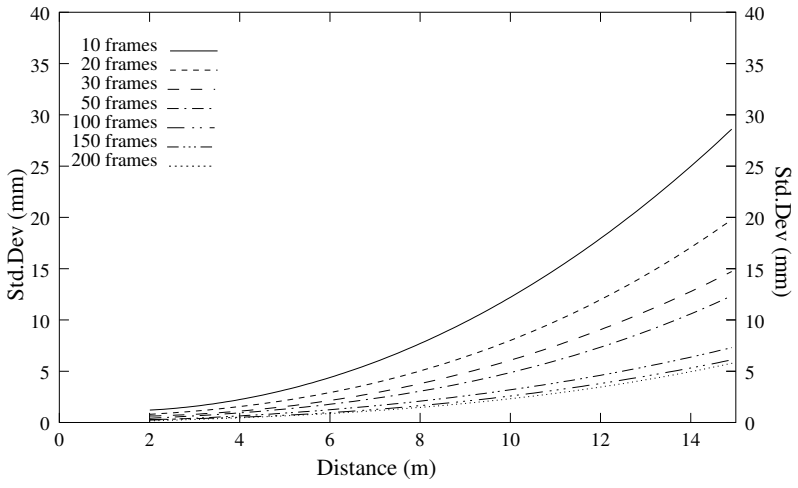


**Figure 9.** Effect of number of images in block on object point accuracy

## 4.5 Quality of initial values

In simulation tests, the initial values were set close to the correct values. The reason for this was that there then would be no risk of the adjustment not converging to a local minimum. The simulation environment was also used for testing the limits of the goodness of initial values. The parameter values were slightly changed from their correct values and only one parameter was alternated at a time. The test was first accomplished without noise, and then only a small amount of noise was added to the image observations.

The orientation angles of the first camera were more sensitive to the incorrectness of the initial values than the $\alpha$-angle of each photo or length of radius $r$. For $\omega, \phi, \kappa$-angles, the initial values were required to be better than $3^\circ - 5^\circ$ in order to meet convergence. For $\alpha_i$-angles, $5^\circ$ was generally good enough, and for length of radius $r$ the initial value $\pm 5cm$ was acceptable. When evaluating the system sensitivity with respect to the initial values of 3D points, it was discovered that the discrepancy of a few decimeters up to a meter from correct coordinate values were still acceptable.

In general, it can be noted that this photogrammetric measuring method requires more accurate initial values for parameters than the measuring approach based on convergence imaging. Acquiring the initial values for common block parameter $\omega, \phi, \kappa$-values is an especially demanding task. The reason that these parameters are more strict with their initial values can be deduced from the fact that all rotation matrices are derived from these parameters. Also, all image observations affect the determination of the values of these unknown parameters in the adjustment process. However, obtaining such accurate initial values for this kind of regulated imaging strategy is easily achievable by the use of simple auxiliary instruments, i.e., measuring tape, angle measuring devices, etc.

# 5 VERIFICATION OF THE DEVELOPED METHOD

By using simulation, one can verify the system as being able to work in general. But it is quite usual that not all possible variations from the ideal state of the system can be simulated. This has also been the case in simulations described in Chapter 4. A possible source of errors in imaging systems is systematic error in the imaging devices, i.e., in the camera and lens systems. Also, it is presumed in the mathematical model that no deviation of camera pose with respect to the rotation plane or orientation of the optical axis of the camera with respect to the path of rotation can exist.

In order to verify the results derived from simulated tests, two field tests with real images were carried out. The aim of the tests conducted was to compare the object coordinate values received from the measuring system with an exterior reference. Two tests were accomplished; one was conducted in an indoor environment and the other in the open-air, in more optimal conditions.

## 5.1 Verification methodology

The decision to use reference data was made partly to verify that the developed mathematical model would apply in real conditions and partly to gain an estimate of achievable accuracy. The precision of measurements can be evaluated by use of error propagation. This, however, would not necessarily reveal the possible systematic errors inside the estimation model. The reference information must be acquired with a degree of accuracy better than that of the observed data it is compared to, in order to guarantee the reliability of test results.

In this research, the exterior reference has been attained by tacheometer measurements. The same instrument, a *Geodimeter 600*, has been used in both tests in the acquisition of reference data. The 3D object targets were measured mainly from a single measuring station by means of vertical and horizontal angle measurements and one distance observation. As is commonly known, the tacheometer can provide accurate measurements of target objects if the object distance is above ten meters. At shorter ranges, distance measurements especially become less accurate. However, a confidence check could be made in the calibration measurements of the instrument in distances shorter than ten meters.

Because the imaging is symmetrical in nature, the accuracy of object point measurements is supposed to be equal for all points at the same distance from the imaging station. This was realized earlier with simulated tests. For this reason, the reference tacheometer measurements were made from the same point as the photographic imaging. The object distance in such arrangements is the same in both methods, which are therefore more comparable with each other.

The tacheometer measurements can be considered to be more accurate than the image-based methods of the circular image bock for object distances longer than five meters. Within shorter distances, the reliability of tacheometer measurements is reduced and the accuracy will be on the same level, or even worse, than with image-based methods. This is a mild drawback, since, in order to assess the accuracy of this method in the whole range, some accuracy information is needed for the shorter distances as well. In order to overcome the problem, object points at close range were measured from more than one measuring station and coordinate systems were then bound into a common coordinate system. Unfortunately, this could be done only with the test conducted outdoors. In the indoor case, the point distribution and complexity of the measuring environment made the equivalent arrangement impractical to realize. For this reason, the results concerning the case with shorter distances should be studied with caution. In the optimized test case, the accuracy of reference can be estimated to be better than two millimeters, since that was the maximum residual in the estimation of the coordinate transformation of separate point sets into a common coordinate system.

### 5.1.1 Targets

The objective in targeting is to be able to measure the same object points in both reference and photogrammetric coordinate frames. In the indoor test case, the used targets were printed black circles on white backgrounds attached to cardboard as shown in Figure (10a). In the middle of the black circle there was a white spot, which was used to assist in setting the field prism in the centre of the target. Three different sizes of targets were used in the test to compensate for the scale difference in the image measurements. The diameters of the circles were $30$, $60$ and $100$ millimeters. The further the point was located from the imaging station, the larger was the target size used.

In the optimized test case, the used targets were retro-targets or retro-prisms. The retro-targets were made of retro-reflecting material and were designed especially for tacheometer measurements. The targets were originally of a square shape, but were covered with black adhesive paper with a round hole in the middle, as indicated in Figure (10b). The idea was to provide favorable conditions for image matching, since a circular shape in image matching is more invariant to perspective distortion than a rectangular. In this case, the size of the targets was fixed. There would have been two different sizes of retro-targets available, but since the difference would have been so small, only $20mm$ size targets were used. The distance observations were tested with tacheometer retro-target combination at several distances ($4m, 5m, 10m, 15m, 20m$) and the standard deviation of distance observations was $\pm 1.0mm$, which is quite acceptable.


( a ) Indoor Case: Cardboard targets


( b ) Optimized Case: Retro-targets in black background

**Figure 10.** Used targets in experiments.

## 5.2 Image measurements

In photogrammetric measurement systems, the image point correspondence problem is the most demanding task from the image measurement point of view. In general, the choice, of which of the points are to be measured is not as important as how precisely the image points can be located and how reliably it can be verified that corresponding image point observations are from the same object point. It is not strictly true to say that the choice as to which points are measured would have no importance. The distribution of image points on an image does affect the accuracy of block parameter estimates. But what is meant here is that points measured in this stage do not have to have any relevance from the object modelling point of view. The only purpose of point measurements is to be able to determine the camera pose with respect to the coordinate system. Although, in these tests, the aim was to compare two data sets at the same object point location, and therefore the object measurements were carried out with targeted points. However, a few image observations were made on untargeted natural points as well.

So, in selecting an image measurement strategy, one good choice could be feature-based image matching. In a feature-based solution, the prominent well-defined image point set is measured automatically. Extraction and selection of image points on images is based on local distinct properties of the gray-level function. The most significant algorithms, so-called interest operators, for extracting image points, have been developed by *Moravec*, *Harris* and *Förstner* (Förstner and Gülch 1987; Förstner 1986; Mikhail et al. 2001). The correspondence of image points on other images can next be determined by examining the feature properties. The decision on the correct match can be based purely on geometrical reasoning and

the feature properties themselves. In addition, the feature properties of interest points in the vicinity can be taken into account in decision making. There is a group of strategies to follow in order to solve the correspondence problem in a robust manner. If some á priori knowledge of imaging geometry is available, this can be taken into account as well. In this research, the initial approximates of camera pose can easily be produced due to developed imaging strategy; applying the feature-based method for image point measurements is therefore sensible.

As mentioned previously in this section, the objective was to be able to measure the same object points both in a geodetic and photogrammetric manner in order to compare the data sets. This was the main argument for using area-based image matching approach. This way we can have control over object point measurements. Also, the precision of individual image observations based on the area-based method has been discovered to be better than in the feature-based method (Mikhail et al. 2001).

Area-based matching, sometimes called template matching, is a method for searching a similar image patch (template) of the source image on the target image. The template image is a small image patch extracted in a particular location from a source image. The source image is an image whose corresponding image points will be searched on another image - here designated as the target image. The method does not necessarily require human interaction. The area-based matching method can be applied in combination with the feature-based approach by first selecting the suitable image patches on the source image with the help of an interest operator and then applying the template matching at the location indicated by the correspondence match. But once again, since the particular object points are the subject of interest, human interaction is required to point out the equivalent image point at least on one image.

### 5.2.1 Strategy of image measurements

The followed procedure in image observation acquisition can be considered to be semiautomatic. The goodness of initial values of block parameters were exploited in the automation of image measurements. The object point was first measured from one image of the block by the human operator, and after that the same image point was used as a template for matching on an image of the second block, as indicated by Figure (11). The idea was that the camera pose and orientation were approximately known and the object point coordinates could easily be calculated from these two image point observations. This coarse approximation of object point location could subsequently be back-projected on other images of both image blocks; see Figure (12). The back-projection of the object point indicated the image area where the corresponding image point would be located on other images. How closely the back-projection will succeed in exposing the real location of corresponding image points is heavily dependent upon block parameter approximations. This procedure was followed until all preferred object points were measured.

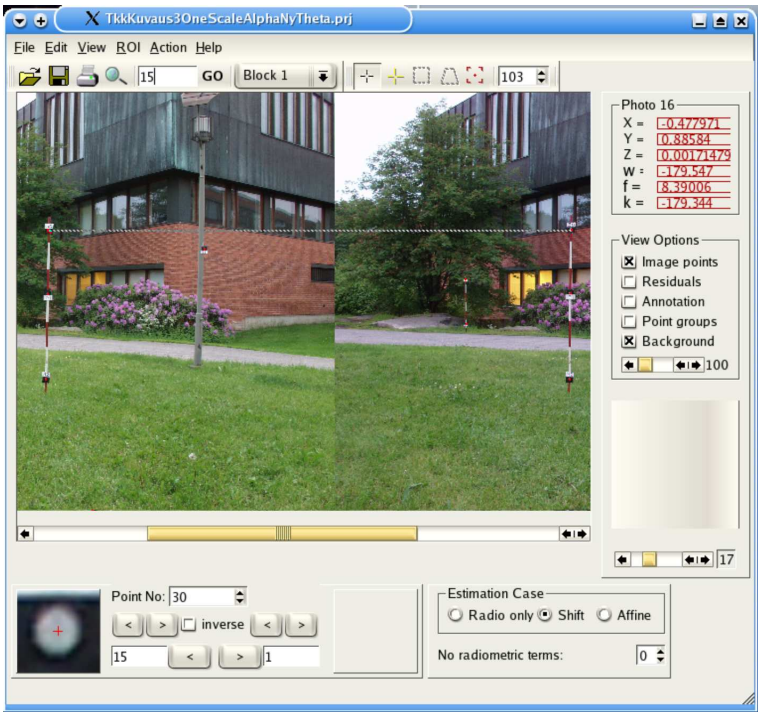


**Figure 11.** Correspondence of image points (shown by the operator) between image from Block I and II.

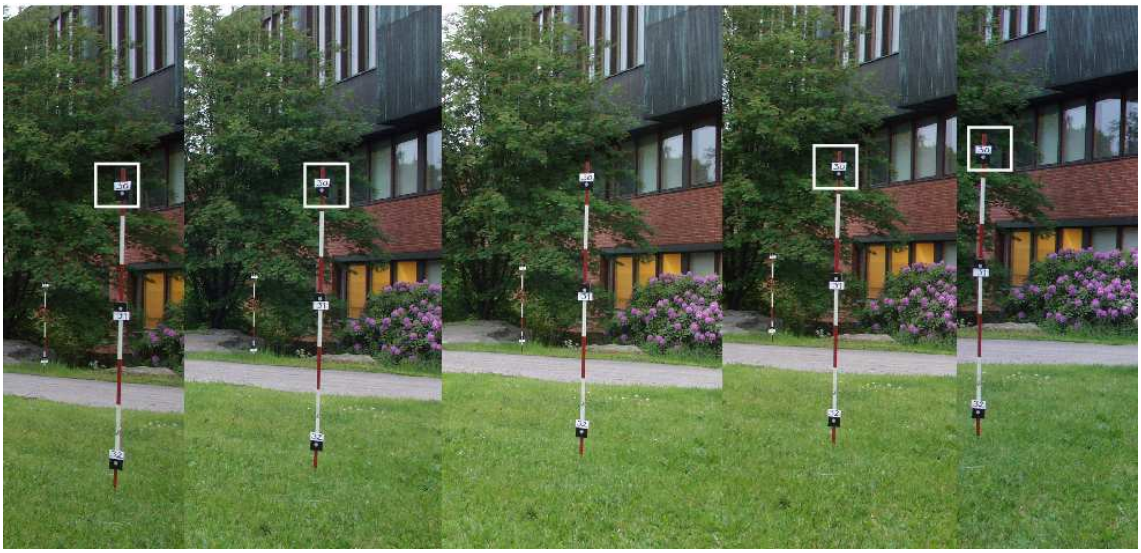

**Figure 12.** Back-projection of an object point on images of one image block.

The selection of the image point on the first image was accomplished manually. The object point could be measured with sub-pixel accuracy by utilizing image magnification. Next, an image patch was extracted from the image and the tem-

plate was generated from that image patch, so that the measured image point located exactly at the centre of the template. In template generation, the bilinear interpolation method was used to derive new gray-level values for the new pixel locations in all three channels (red, green, blue). The size of the template might also be changed.

A disadvantage of the area-based matching method is that it cannot tolerate big perspective distortions between matched images. If the object surface is a flat surface, the distortion can be considered as a 2D transformation problem. An assumption of a flat object surface can be made only if small image templates are used. In general, a smooth object surface can be approximated by number of small flat patches. Since the used targets were flat, no violation to that restriction of the method was made. Also, possible distortion could be diminished by selecting a target image on another block whose direction of view was close to the source image. The reason why the target image was chosen from another image block, and not among consecutive images on the same image block in this first stage, was due to better imaging geometry. The image pair chosen is close to the stereo case; the larger the base-to-distance ratio, the better the accuracy in point determination. So getting better approximates for object point coordinates helps us to acquire the rest of the corresponding image point observations more reliably.

For template matching, the Least Squares-method (LSQ) was applied. In LSQ matching, the gray-level function of the template is matched against target image gray-levels at a given location. The template is moved on the target image until the sum of least squares of gray-level value differences is minimized. This gives the location of the corresponding image point of the template to sub-pixel accuracy on the target image. Since the matching problem is turned to nonlinear form, the solution can only be achieved with the help of an iteration process. However, the matching process needs good initial values for iteration and the operator therefore has to give the starting point within a few pixels from the correct location.

For the rest of the image point correspondences, the calculated approximate location of the object point could be used to indicate the initial locations by means of back-projection. However, these initial locations could not be regarded as accurate enough for applying the LSQ-matching directly. A better start-point for iteration was acquired, therefore, by use of image correlation. The cross-correlation of template image and target image was computed for every location in the search area. The back-projection strategy worked at this stage in favor of reducing the size of the search area on the target image, as illustrated in Figure (12). If no á priori knowledge had been available, the cross-correlation of template and target image would have had to be computed at every pixel location of the target image. This way, the amount of computation was reduced and the search area could be set around the back-projected image point. The size of the search space could be changed at the operator's discretion. The calculation of the correlation

coefficient based on the equation of the normalized cross-correlation coefficient is given (Schenk 1999):

$$\rho = \frac{\sum_{i=1}^{m}\sum_{j=1}^{n}(g_r(i,j) - \bar{g}_r)\,(g_l(i,j) - \bar{g}_l)}{\sqrt{\sum_{i=1}^{m}\sum_{j=1}^{n}(g_r(i,j) - \bar{g}_r)^2}\sqrt{\sum_{i=1}^{m}\sum_{j=1}^{n}(g_l(i,j) - \bar{g}_l)^2}} \tag{38}$$

In Equation (38) $\bar{g}_r$ and $\bar{g}_l$ are mean gray-level values in the template and matching window, respectively. The value of the correlation coefficient $\rho$ will lie in the range of $-1 \leq \rho \leq +1$.

On occasions when the back-projected point was located near the edge of the image, there was doubt if the object point was out of the field of view. In order to overcome this, the threshold value was set for the maximum correlation coefficient based on empirical observations. The maximum correlation coefficient value within the search window had to be exceeded before proceeding to the final measuring stage. Otherwise the conclusion was that that point had been out of sight, and the search for the conjugate image point was halted. If the threshold for correlation coefficient was exceeded, the pixel location that had the largest correlation value was then used as a start point for the final LSQ-matching to sub-pixel accuracy. The template matching was run sequentially in such a way that the template was extracted always on the previous image and was only used for a subsequent image in a block. So after every successful match, a new template was extracted in that location and it was only used in matching on the next image. This way, the effect of perspective distortion could be minimized in the matching procedure.

The LSQ-matching can be considered as a two-dimensional signal fitting process. In the least squares context, the $f(x,y)$ is a gray-level observation from a template image in location $(x,y)$ and $g(x,y)$ is a transformation function for the target image, which minimizes the gray-level differences between images. The observation equation in the least squares sense is then

$$f(x,y) - e(x,y) = g(x,y) \tag{39}$$

The component $e(x,y)$ in Equation (39) describes the random effect (noise) in both images. This is an LSQ-image matching idea, which was presented in the early 1980's. The estimation model has been presented both by Grün (Grün and Baltsavias 1985; Grün 1996) and in parallel to Grün's investigation by Prof. Ackermann and his research group at the University of Stuttgart (Ackermann 1984).

Transformation is supposed to rectify the target image patch into a template image pixel coordinate system. If the source image and target image are taken substantially from different view angles, and the object is evidently three dimensional, the rectification would not satisfy the perspective distortion between images. However, by assuming the object surface is smooth and treating only a small patch of the image in matching, even the following affine transformation can be considered to be adequate for the task (Ackermann 1984):

$$\begin{cases} x = a_0 + a_1 x_o + a_2 y_o \\ y = b_0 + b_1 x_o + b_2 y_o \end{cases} \tag{40}$$

Since it is a case of two separate photographs taken with different exposures, the radiometric difference between images also has to be taken into account. In this research, as in the original research of Ackermann (Ackermann 1984), two linear components of radiometric transformation were considered to be adequate, as given by:

$$f(x, y) - e(x, y) = g^o(x, y) + r_s + g^o(x, y) r_t \tag{41}$$

The linear radiometric transformation included the *shift* $r_s$ and the *scale* factor $r_t$ as depicted in Equation (41). The LSQ-image matching algorithm was implemented with a simple image shift operation also. Instead of estimating all affine parameters, only the displacements in both $x$- and $y$-directions were included. This kind of simplification is justified if no perspective distortion is expected. Also, this solution does not allow any significant image rotation between images.

Nevertheless, a simplified version of the LSQ-image matching method was used successfully, since the used targets were the shape of a circle and therefore invariant for image rotation. Also, the scale difference and effect of viewing angle were considered to be small enough to be disregarded. The reason for finally using a reduced parameter set is partly because of the known risk of over-parameterization in the estimation process. In some cases, the target size was as small as 9x9 pixels, which can be considered to be too small an image area to reliably solve all six affine and two radiometric parameters. However, the affine model was also used when the posterior estimate of standard deviation $\hat{\sigma_0}$ of gray-level observation was detected to be too large for the use of shift parameters only. Also, the choice of estimation model was based on visual inspection made by the operator.

For observing all conjugate image points of a single object point, the only actions required from the operator were to measure the object point from one image and to point out it's equivalent location on an image of the other block, as indicated in Figure (11). The rest of the homologous image points were found automatically

and their relation to each other and to the object point could be stored for further computation.

All image measuring operations and calculations were implemented in a computer program written by the author of this thesis. At the time, the research work was started, there was no software on the market that could handle the image sequence and measure homologous points with sub-pixel accuracy; those that were available were not flexible enough to be altered for the special needs of this measuring method. The implementation was carried out in the *Linux RedHat 9.0* platform with *2.4.20-8* kernel. The programming was accomplished in C++ programming language and, for some graphical operations and user interfaces, Qt-3.1.2 library functions were utilized. Also, some matrix operations in the estimation part were programmed by exploiting the library functions of the mathematical programming library package, LAPACK (Lapack 2005).

## 5.3 Real world experiments

The real world experiments were made in two different setups, one of which included fairly optimized conditions, while the other included more realistic measuring conditions. The experiment accomplished in optimized conditions will be designated from now on as *Experiment I* and the one made in the indoor environment as *Experiment II*. For both experiments, selected object points were targeted and reference measurements made with geodetic techniques for the purpose of comparison as depicted in Section 5.1.

### 5.3.1 Experiment I

In this experiment measuring conditions were designed to be as optimal as possible, i.e., optimized regarding both photogrammetric measurements and the geodetic reference system.

The rectangular retro-targets were covered with black adhesive paper with a round hole in the middle, as depicted earlier in Section 5.1.1 and Figure (10b).

All targets were faced to centre partly to obtain an optimal orientation for tacheometer measurements and partly to provide favorable conditions for the selected image matching method. The distribution of points was designed so that there would be enough points within different object distances. Special attention was paid to observe the effect of object distance on point accuracy since the accuracy is independent of the direction to the object point, due to symmetric imaging. Targets were attached to the measuring poles at different heights, as shown in Figure (13). The reason was to get adequate point distribution in the vertical direction also. This is essential in order to determine camera orientation reliably.

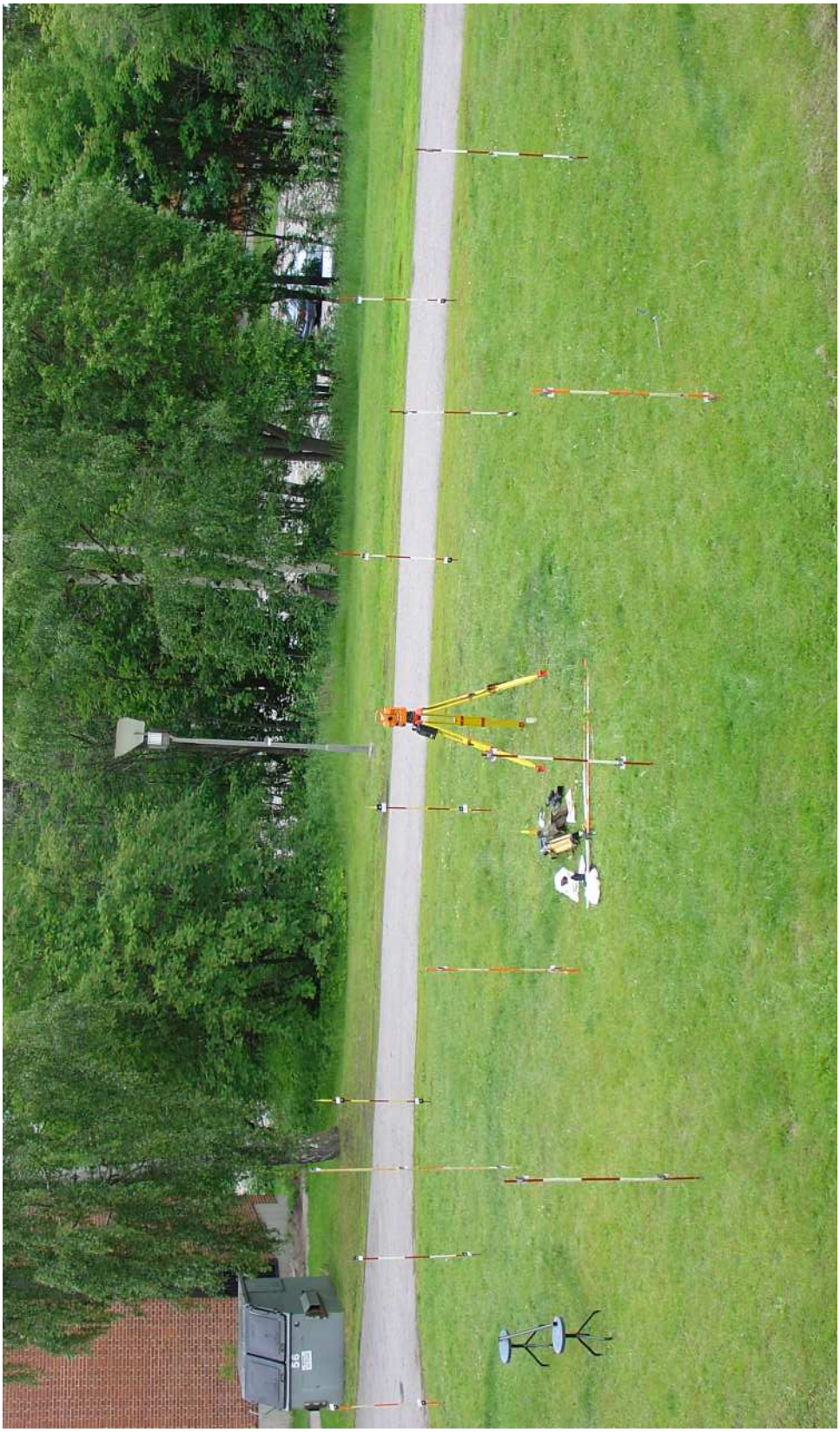

**Figure 13.** Distribution of target points attached to the measuring poles in Experiment I.

The camera setup was attached to the same tripod that was used in the tacheometer measurements. This way, the origin of both coordinate systems could be approximately centred on the same point. It has to be emphasized here that geodetically measured coordinates were never used as a control datum, but only for the purpose of comparison. The orientation of both local coordinate systems was fixed by using the same object point in order to define the reference direction for plane coordinate axes.

**Figure 14.** Camera setup in Experiment I.

The navel centre was equipped with a centring device that had a bubble leveling compensator. Leveling of the imaging system was not necessary by definition, but it gave feedback as to how stable the system was during the imaging sequence. The camera used in the experiment was an Olympus E-10 (1680x2240pix, c=2350pix) digital still camera and this was attached to the end of the metal bar $480mm$ from the centre, as shown in Figure (14) . The other end of the bar was supplied with an adequate counterbalance in order to maintain stability during imaging. Images in sequence were taken with equiangular steps. The plane angle between subsequent images was $12^\circ$ resulting in 30 images per image block. The camera was triggered with wireless remote control and the focus set to infinity; the aperture was also predetermined according to setup values used in a previous camera calibration. The exposure time was allowed to be determined by the automatic function of the camera. For the second block, the camera was turned around $180^\circ$ and imaging was started at the same start point as the first image sequence. Naturally, the real location of the projection centre inside the camera could not be precisely determined at this stage. So the minor plane rotation difference between image blocks had to be accepted.

The required initial values for block parameters could be obtained by using simple instrumentation. The radius of rotation could be evaluated by use of a

tape measure and, for plane rotation angle readout a graduated scale attached to the centring device could be used. The angle of optical axis with respect to the supporting bar was fixed to the perpendicular alignment with the help of a simple tool.

There were, in total, $43$ targets used in the experiment and the distance range of targets was from $2m$ up to $22m$. The distribution of points was designed in such a way that the target distances were distributed evenly. At least two targets were attached to each measuring pole. The measuring poles were divided across the target field so that targets could be used as tie points in the mensuration of image blocks. The scale bar used for getting scale for measurements was set up at the distance of $6m$ from the origin. The nominal value of the calibrated distance was somewhat under $2$ meters.

The initial values for unknown parameters were acquired quite easily. The length of the bar was measured with the accuracy of a centimeter and rotation to an accuracy of one degree. In this experiment, the camera was fixed perpendicularly at end of the bar. With the help of a simple tool, this could be accomplished within $1^\circ - 2^\circ$. The length of the scalebar was added into the estimation as a constraint, the length having been verified beforehand in laboratory conditions.

### 5.3.2 Experiment II

The second experiment was conducted in an indoor environment. The target area was an entrance hall, where the maximum distance inside the area was approximately $40$ meters. Conditions were not as optimal as in *Experiment I*. Compromises had to be made as regards the photogrammetric measuring system and acquisition of geodetic reference data. Targets used in the experiment were attached to walls and to surfaces of columns inside the test area. This time, retro-targets were not used, since they could not be measured reliably with a tacheometer. In these circumstances, it was known that difficulties would occur with distance measurements. When using retros, it is required that the incident angle of the measuring ray should be equal or near the normal to the target surface to receive an impulse of a reflected ray of adequate size; this cannot be guaranteed in indoor space. Therefore, a standard field prism was used for reference measurements and the targets used were printed targets made of cardboard. Three different sizes of targets were used in *Experiment II* for different object distances. A more detailed description was presented in Section 5.1.1 and in Figure (10a) .

In this experiment, the focus was set on more robust imaging system development. The plane rotation is a hard condition to be fulfilled. Human intervention in the rotation of the camera from one exposure to the next, and triggering the camera, can cause unwanted discrepancy of supposed camera orientation. Some abnormality in the height of the projection centres from the plane of rotation during imaging can easily occur, if sufficient precautions are not taken.

In order to fulfill requirements and to receive better initial values, a ball-bearing type of rotation system was designed and assembled. Better rotation control was achieved by supplying the system with a worm gear and a step motor, Figure (15a). The step motor was controlled by the computer to rotate the camera with equal-angled steps, Figure (15b). The camera was also triggered automatically under computer control. In order to obtain other required initial values, the same procedure as in *Experiment I* was followed.

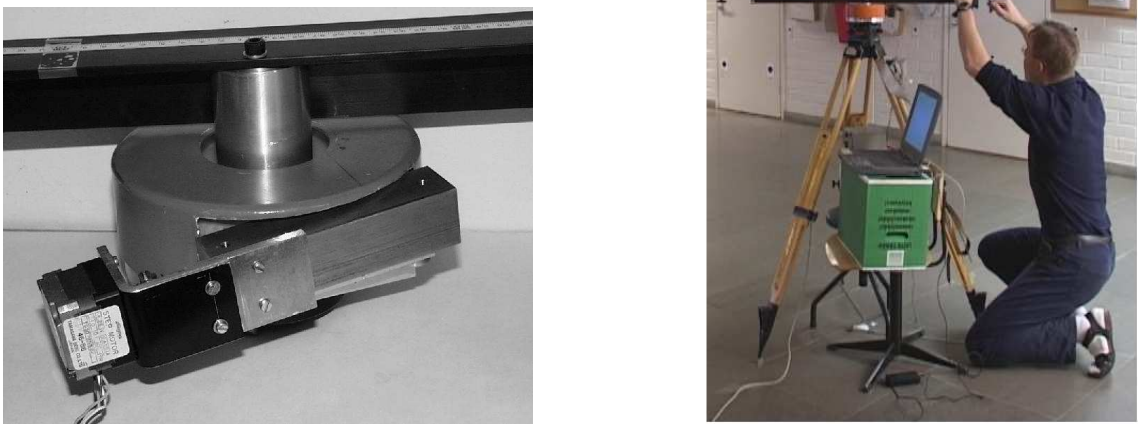

( a ) Step motor fitted into worm gear. ( b ) Computer contolled imaging system.

**Figure 15.** Step motor driven imaging system

This type of system design provided fully-automatic imaging without human intervention. The camera was the same as that used in *Experiment I* and the same setup of camera parameters as used in the earlier camera calibration was adopted.

The experiment was run in interior space in an entrance hall, which consisted of a corridor, two round columns and a staircase, as seen in Figure (16). So the conditions were representative of those one might meet when carrying out a typical measurement task in interior space: blind angles, small angles between wall surfaces and viewing angle plus varying illumination.

The imaging was made from the same spot as the tacheometer measurements. The rotation centre of imaging differed only a few millimeters from the tacheometer coordinate system. This was verified afterwards with a coordinate system transformation. Imaging was accomplished with a computer controlled system with 32 photos per image block, the camera with a perpendicular viewing angle being attached to the supporting bar approximately $450mm$ from the rotation centre. The camera settings were fixed to the same focus and aperture values as used in camera calibration. The exposure time was allowed to be determined by the automatic function of the camera. The imaging was carried out

**Figure 16.** The entrance hall where the experiment took place.

under artificial illumination conditions and there was no control over how the fluorescent lamps impacted upon image quality in any individual shot. For this reason, some images were over-exposured and some under-exposured. Nevertheless, targets were able to be measured on images reasonably well. The scale bar with a length of $\sim 2m$ provided the scale for the 3-D measurements and was set at a distance of $4m$ from the centre of measurements.

## 5.4 Camera calibration

The camera used in both experiments was an Olympus E-10, a typical non-professional digital still-camera. According to the manufacturer, the camera has a $1680 \times 2240$ pixel resolution with a $35mm - 140mm$ zoom lens. The camera was used in experiments only with focal lengths in wide-angle mode with a single-aperture stop value. The camera was therefore calibrated only with those settings.

In camera calibration, linear sensor deformations and nonlinear lens distortion corrections were calculated according to the distortion model presented in Section 3.4 in Equations (17) and (20). For the calibration, a three dimensional calibration field was photographed from five imaging stations, see Figure (17). In each imaging station, three images were taken, having approximately $90^\circ$ roll between exposures. So, all together $15$ images were taken and around $70$ targeted object points were measured. The estimation of unknown camera calibration parameters was carried out via free-net adjustment with a single distance measure. In free-net adjustment, inner constraints were applied.

**Figure 17.** Three-dimensional calibration field used in calibration.

In both experiments, the resolved calibration parameters were kept fixed in the block computation and only block parameters and object coordinate values were estimated. In the latter analysis, it was suspected that radial distortion parameters were not determined with adequate accuracy after all. Therefore, in addition, *a plumb-line calibration* was accomplished in order to obtain better estimates of the amount of distortion of the lens. The problem with camera calibration carried out with the calibration field is the high correlation of decentring lens distortion parameters and the principal point, especially with $y_p$-component and $p_1$. However, this problem can be overcome by solving the lens distortion parameters, with, for example, plumb-line calibration and the rest of the calibration parameters with test field calibration.

For the *plumb-line calibration*, $12$ plumb-lines were set to hang from the ceiling in front of a dark background, see Figure (18). The plumb lines were made of a heavy fishing line, having small weights tied at the other end and letting them hang freely. Three images were taken at a single position with $90^\circ$ roll between exposures. The distance to plumb lines was only two meters, but the camera focus was set to infinity; other settings were the same as with earlier calibration. The procedure followed in plumb line calibration was similar to that reported by Fryer (Fryer et al. 1994).

The centre of the lines were observed from images by means of centroid computation of gray-levels in the transversal direction. Samples of the centroid locations were observed at evenly separated points along the line.

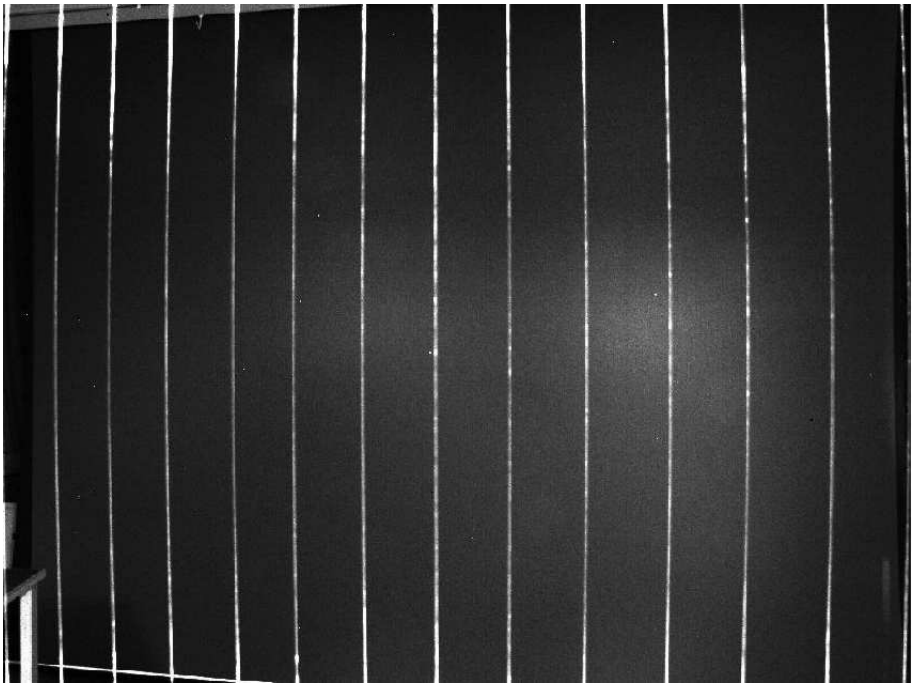

**Figure 18.** Used plumb-lines in camera calibration.

In computation of camera calibration, only the first two coefficients of radial distortion parameters $k_1$, $k_2$ and decentring distortion parameters $p_1$, $p_2$ were estimated. In addition, the line parameters $\alpha_l$ and $d_l$ had to be estimated. The straight line equation in a parametric presentation is given as

$$\mathcal{F} = x_i \cos\alpha_l + y_i \sin\alpha_l - d_l = 0 \tag{42}$$

In Equation (42), $x_i$ and $y_i$ are corrected image observations according to the distortion model. The lens distortion is included via terms $dx$ and $dy$ as follows:

$$\begin{cases} x_i = & x + x_p + dx \\ y_i = & y + y_p + dy \end{cases} \tag{43}$$

The Equation (43) presents the corrected image observations. It is to be noted that the adjustment model differs from that depicted in Equation (1) since the object function is in implicit form. This means that Equation (42) has to be differentiated with respect to observations also:

$$B(l + v) + A\Delta x = f \tag{44}$$

In computation of new calibration parameters, the corrections were made to distortion parameters and line parameters after every iteration round, until the corrections were small enough to be neglected. After this, new values were applied in the calibration model and a new estimation of other calibration parameters were computed, while lens distortion parameters were set fixed with observations made on images of a three-dimensional calibration field, Figure (17). This was repeated until no corrections were required for any calibration parameters. The reason for this kind of procedure was that it is not possible to solve all calibration parameters with plumb line calibration and the change of lens distortion parameters have an effect on other calibration parameters and vice versa.

# 6 RESULTS AND ANALYSIS

## 6.1 Refinement of the mathematical model

The mathematical model presented in Section 3.6 was followed in the computations. As mentioned earlier, over-determination was exploited in measurements, partly to improve the precision of estimates and partly to be able to evaluate the quality of measurements afterwards. The estimation was based on linear least squares, which guaranteed the optimal solution with respect to the observation error. The collinearity condition Equation (31) is non-linear with respect to the parameter set based on polar coordinates and is dependent on rotation angles. So, solving the unknown parameter values leads to an iterative solution and the need for initial parameter values. Initial values can be acquired in a relatively easy manner, as explained in Section 5.3.

Computation converged nicely after a few iterations. In earlier experiments, where initial values were not accurate enough, the computation model had to be altered to some extent. The parameter set had to be computed in groups in order to assure the convergence of computation. First, only the plane rotation angles $\alpha_i$ were set free, while the other parameter values were kept fixed. Iteration was continued until the convergence was reached. After this, the common camera rotation angles $\omega_0, \phi_0, \kappa_0$ were also set free one by one and, in the final stage, radii values of both image blocks were set free as well, and a common adjustment was computed.

The magnitude of the maximum residual was found to be larger than expected. It was found to be too large when compared through experience or by means of equivalent instrumentation to other close-range measurements; this was especially the case when the fact that targeted points were used was taken into account. The posterior estimate of the standard deviation of unit weight observation could be computed from the residual values as

$$\widehat{\sigma}_0 = \sqrt{\frac{v^T P v}{n - u}} \tag{45}$$

This estimate says a lot about the fitness of the measurements with the chosen model. In this case, the standard deviation of unit weight was over one pixel, so it was evident that either the model was incorrect or that there were gross errors among the observations.

When residuals were examined geometrically, the vertical alignment of residual vectors could be noticed directly. This clear systematic pattern indicated that either camera sensor plus lens calibration were not correct or the physical model

presented with the chosen parameter set, Equation (31), could not depict the actual imaging case.

Since calibration was carried out according to standard methods and camera calibration parameters were kept fixed during computation, the conclusion was that the used mathematical model could not entirely explain the physical model.

In order to verify the observed shortcoming of the mathematical model, the photogrammetrically acquired 3D point coordinates were transformed into the same coordinate system as the tacheometer measurements for comparison. For transformation, a rigid body 3D transformation with three rotations and translations was used. When comparing the coordinates, it was immediately noticed that there were big differences on coordinates of the points at greatest distance from the camera.

The restrictions set for imaging required that all projection centres should lie on the same plane and the orientation of the camera with respect to the supporting bar and rotation plane should remain static during imaging. If the requirement of projection centres lying on the same plane was violated, the effect of this discrepancy should be visible on points with shorter distances also. Because the difference in object point coordinates with respect to reference data was much larger with points far away, it was logically deduced that the reason for this discrepancy was more likely due to unexpected orientation angle values than to simple vertical translation.

Modification in the mathematical model was carried out in order to take into account possible variation of the plane of rotation of the camera around the navel point. The variation was suspected to be due to transversal tilt of the supporting bar within the imaging session. Figure (19) describes the expected alteration of camera height from nominal rotation plane during imaging due to tilting of the bar.

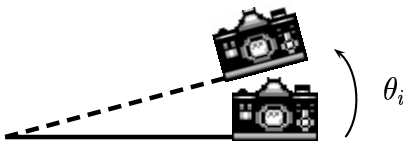


**Figure 19.** Possible transversal tilt of bar during imaging.

An additional parameter $\theta$ was added to the mathematical model to describe the height difference from the nominal plane of rotation on each camera pose, see Figure (19). The number of parameters was increased by $n-1$ from the original set of parameters in Equations (27) and (28). Only the first camera of the first block was supposed to have a fixed value $\theta = 0$ defining the nominal plane. The total

number of parameters was nearly doubled, but still the system was substantially overdetermined. It is essential to notice that this geometrical interpretation affects both projection centre coordinate values as well as rotation matrix construction, as is depicted below:

$$\begin{cases} X_i = & r \cdot \cos\alpha_i \cdot \cos\theta_i \\ Y_i = & r \cdot \sin\theta_i \\ Z_i = & r \cdot \sin\alpha_i \cdot \cos\theta_i \end{cases} \tag{46}$$

The change made in computation of the rotation matrix for each individual camera pose could be derived from the common parameter angles of the block with multiplication of rotation matrices:

$$R_{\omega_i,\phi_i,\kappa_i} = R_{\omega_0,\phi_0,\kappa_0} \cdot R_{\alpha_i,\theta_i} \tag{47}$$

This refinement of the model, presented in Equations (46) and (47), reduced the standard error of unit weight $\widehat{\sigma}_0$ from $1.340$ pixels to $0.897$ pixels in the common adjustment. The effect of introducing a new parameter into the model can be illustrated in the height variation of the projection centre from the nominal plane during the imaging, which is shown in Figure (20). The fluctuation inside one image block is quite small, but a clear shift can be noticed between image blocks. This shift of $6mm$ could have happened when the camera was turned into the opposite direction at the end of the bar between the first and second image sequence. Similar fluctuation of an array sensor from the nominal plane rotation during imaging has also been reported in investigations of panorama-cameras (Parian and Gruen 2004).

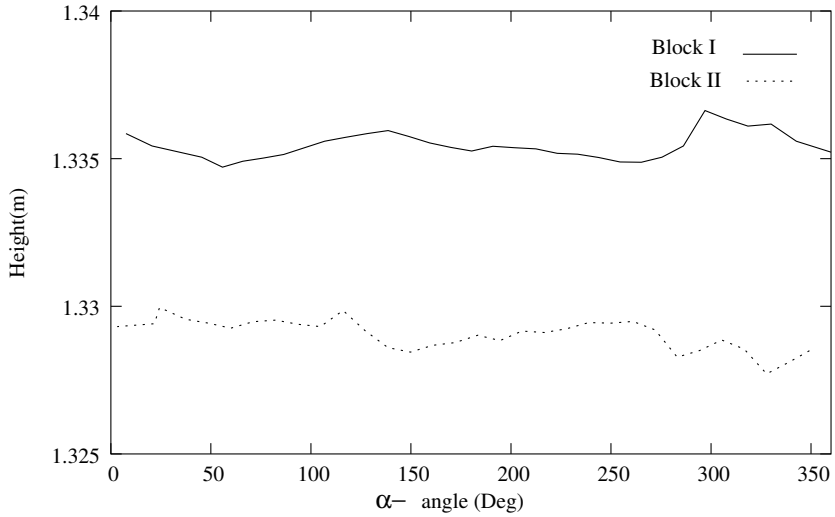


**Figure 20.** Height variation of projection centre during imaging.

After this model refinement, the maximum length of the residual vector was still over four pixels and residuals in $y$-direction were still slightly bigger than in $x$-direction. Also, the comparison to reference showed that the 3D points were systematically farther away than points measured by a tacheometer. The conclusion drawn from this discrepancy was that the camera must have been tilted in the direction of the optical axis during imaging as well. Figure (21) demonstrates this suspected phenomenon.

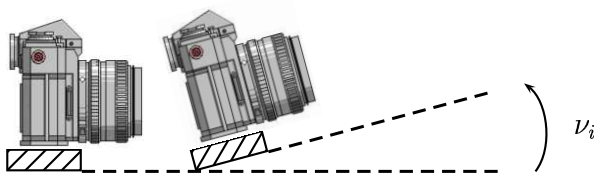


**Figure 21.** Possible tilt of the camera in direction of optical system.

The tilting can be considered as a vertical plane rotation. Some vertical and horizontal displacement of a projection centre may have occurred as well as a consequence of this tilt. This, however, can be neglected, since the maximum value of the tilt $\nu$ was less than $1^\circ$ and the maximum effect of the tilt was less than a millimeter in the projection centre coordinate value. So, the effect of the tilt can be appended as an additional angle in the calculation of the rotation matrix:

$$R_{\omega_i,\phi_i,\kappa_i} = R_{\omega_0,\phi_0,\kappa_0} \cdot R_{\alpha_i,\nu_i,\theta_i} \tag{48}$$

With this last addition, given in Equation (48), the systematic pattern on residuals seemed to have disappeared, at least when visually examined . Also, the standard deviation of unit weight $\widehat{\sigma_0}$ reduced to $0.23$ pixels, which is quite typical in close-range photogrammetric cases and correlates with earlier experiments.

The refined mathematical model defined in Equations (46) and (48) was adopted for all further computations reported in this thesis. The collinearity condition then changed into the form:

$$\begin{cases} x = -c\,\dfrac{a_{11}(X_{obj}-r\cos\alpha_i\cdot\cos\theta_i)+a_{12}(Y_{obj}-r\cdot\sin\theta_i)+a_{13}(Z_{obj}+r\sin\alpha_i\cdot\cos\theta_i)}{a_{31}(X_{obj}-r\cos\alpha_i\cdot\cos\theta_i)+a_{32}(Y_{obj}-r\cdot\sin\theta_i)+a_{33}(Z_{obj}+r\sin\alpha_i\cdot\cos\theta_i)} \\ y = -c\,\dfrac{a_{21}(X_{obj}-r\cos\alpha_i\cdot\cos\theta_i)+a_{22}(Y_{obj}-r\cdot\sin\theta_i)+a_{23}(Z_{obj}+r\sin\alpha_i\cdot\cos\theta_i)}{a_{31}(X_{obj}-r\cos\alpha_i\cdot\cos\theta_i)+a_{32}(Y_{obj}-r\cdot\sin\theta_i)+a_{33}(Z_{obj}+r\sin\alpha_i\cdot\cos\theta_i)} \end{cases} \tag{49}$$

where terms $a_{ij}$ denote the matrix elements of rotation matrix $R_{\omega_i,\phi_i,\kappa_i}$ in Equation (48). The linearization of the collinearity condition, Equation (49), with respect to the new unknowns is presented in Appendix II.

One issue yet to be dealt with is the eccentricity of the rotation system. In a panoramic imaging system, the eccentricity of the rotation has to be determined or it has to be minimized in order to achieve the geometry of ideal panoramic imaging. In this research, the coordinate system is created on site, defining that the $x$-axis must converge with the centre of rotation (navel, origin) and the projection centre of the first camera pose in sequence, which is not necessarily the direction of the supporting bar. The rotation is defined with respect to this coordinate system by definition. Since the bar-camera mount is assumed to be a rigid construction, the only source of eccentricity can be the ball bearing of the rotation or the arbitrary movement of the whole imaging system during the imaging sequence. The possible anti-symmetric rotation caused by a ball bearing system can be considered to be so small compared to other sources of error that it can be neglected. The possible arbitrary movement of the whole system during the imaging sequence is quite hard to determine. The situation is here the same as with panoramic imaging or with laser scanning; the instability of the imaging platform has to be dealt with by other means. Also, here the question is handled by mounting the imaging system on a platform, for example, on a tripod made as stable as possible, and, in this way, ensuring that the possible vibration of the whole system is negligible.

## 6.2 Comparison to reference

In order to compare photogrammetric data with reference data, a rigid body 3D transformation between data sets for Experiment I was calculated. The length of point-to-point differences, shown in Figure (22), represents the absolute coordinate difference between data sets including inaccuracies of both measuring methods and the coordinate transformation. The point differences near the origin are clearly greater due to the unsuitability of a tacheometer for measuring over short distances. Whereas the tacheometer coordinates of far-off points are more reliable, the differences between data sets are due more to the limitation of photogrammetric methods. The second order curve, depicted in Figure (22), was fitted to the data set of point differences. The differences are presented with respect to the nominal distance of points from the origin. It can be compared with the equivalent representation of simulated data in Figure (7), although it has to be remembered that the camera model and the imaging configuration were not entirely equivalent. In both real-world experiments, the radius of the imaging sequence was near $50cm$ and the expected observation standard deviation was $0.23pix$ corresponding to $1.38\mu m$, which is equivalent to the used noise level of $0.05pix \approx 1.3\mu m$ in simulation. The field of view was the same in both camera models (simulated - true) .

In the optimal case, the situation can be considered to be near the simulated case in terms of geometry (all targets facing the centre). However, the number of points in the real-world experiment is essentially smaller than in the simulation.

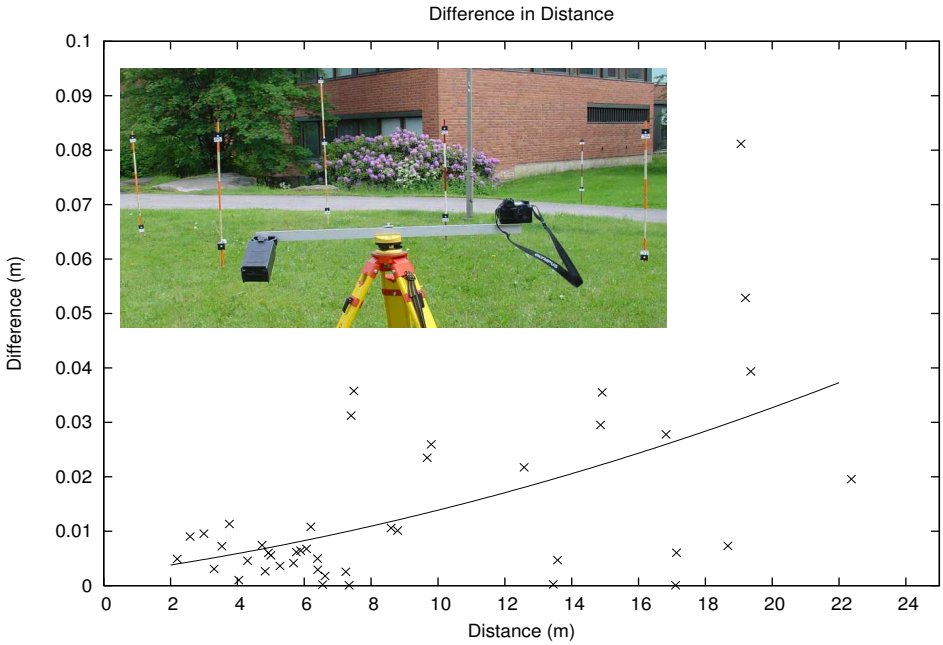


**Figure 22.** Optimal case, Experiments I

Also, it is to be noted that in the simulation the image observation accuracy is assumed to be constant regardless of point distance. In the real-world case, the image scale does have an effect on the accuracy of observations, especially when the size of the target is the same, despite their location. In the simulated case, only random noise is assumed to be found on observations, but, in the real-world experiment, it is not possible to guarantee that all systematic error components can be entirely compensated in computation.

In Figure (22), the coordinate difference between data sets is larger than the standard deviation of point coordinates in the simulated case in the same distance range ($2m - 15m$), compare to Figure (7). In the simulated case, the maximum standard deviation is $5mm$ (noise $\sigma = 0.05pix$) at distance of $15m$, but, in real-world experiment, the coordinate difference is around $20mm$ at this distance. However, differences below $10mm$ within the same distance were recorded. The derived values at the maximum distance ($22m$) give the coordinate difference of $40mm$ which is quite small compared to object distance.

In the case of interior space measurements, Experiment II, the effect of imperfection of reference data with shorter distances is evident, Figure (23). The variation of coordinate differences within the same distance says something about the lack of confidence in the reference values. However, the mean or derived value from the fitted second-order polynomial curve gives an insight into the expected accuracy of the measurements. Compared to equivalent results of the optimized case, Experiments I, larger variation throughout the distance range can be seen.

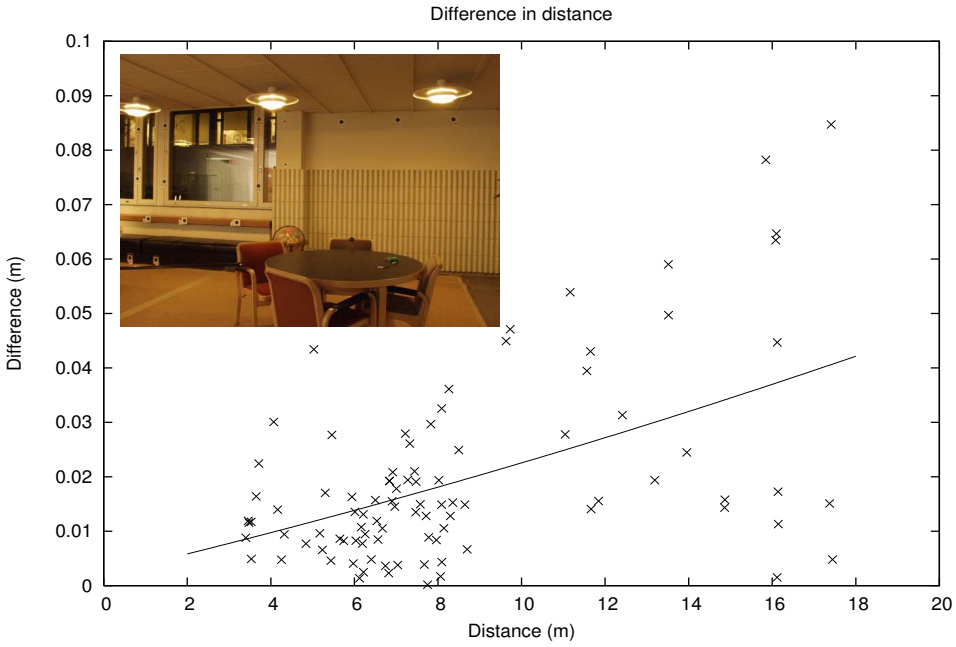


**Figure 23.** The length of point differences respect to object distance, indoor case, Experiment II.

Some discrepancies can be considered to be due to the tilted angle of the target surface with respect to the view angle or inadequate illumination of the target area. Insufficient illumination could be verified for the two furthermost points. In general, illumination can be seen as one of the most restricting elements when trying to achieve the most accurate measurements in indoor environments.

When comparing the indoor case with the optimized case, coordinate differences with respect to reference in the indoor case are only slightly worse than with the optimized case. However, the variation of differences is clearly larger in the indoor case.

### 6.2.1 Root Mean Square Difference

Since the accuracy of 3D point measurements with this method is highly dependent on the point distance from the origin, distinct coordinate differences should be observed for different distance ranges. Another presentation of the object coordinate accuracy can be given in the form of *Root Mean Square Differences* (RMSD). In Tables (3) and (4), 3D coordinate RMSD's are depicted for four distance ranges, approximately five meters each. However, in the first range category, the closest points are not closer than two meters. In Tables (3) and (4), the first column presents the total point RMSD values and the next three columns present the RMSD values in respect to each coordinate. The last column lists the number of points falling into each distance range.

| Distance | RMSD | RMSD X | RMSD Y | RMSD Z | No. of points |
|---|---|---|---|---|---|
| 2m-5m | 0.00705 | 0.00653 | 0.00857 | 0.00574 | 11 |
| 5m-10m | 0.01010 | 0.01191 | 0.00552 | 0.01155 | 19 |
| 10m-15m | 0.01393 | 0.01108 | 0.00502 | 0.02085 | 5 |
| 15m-20m | 0.02459 | 0.03088 | 0.01197 | 0.02678 | 7 |

**Table 3.** Optimized case RMSD values in meters (m), Experiments I.

| Distance | RMSD | RMSD X | RMSD Y | RMSD Z | No. of points |
|---|---|---|---|---|---|
| 2m-5m | 0.01390 | 0.01990 | 0.00602 | 0.01214 | 12 |
| 5m-10m | 0.01286 | 0.01625 | 0.00502 | 0.01439 | 59 |
| 10m-15m | 0.02110 | 0.03293 | 0.00633 | 0.01451 | 13 |
| 15m-20m | 0.02913 | 0.04810 | 0.00832 | 0.01277 | 10 |

**Table 4.** Interior space RMSD values in meters (m), Experiment II.

In Table (3), the RMSD increases with respect to the point distance, which is as expected. With individual coordinate RMSD values, the trend is not so clear. Especially the RMSDY values stay almost constant, except in the last distance range. This says something about the nature of the measuring method. The point accuracy, at worst, will always be in the outward direction from origin and the $Y$-coordinate axis is almost orthogonal to this direction among all points. Whereas with $X$- and $Z$-axis direction, the accuracy varies a lot and is point-location dependent. Especially in the indoor experiment, the effect of the direction of the point location can clearly be seen, see Table (4). In this case, most of the points located far off are along the $X$-axis direction. The degradation of RMSDY values in the last range category, especially visible in the optimized case, can be considered to be due to the change of image scale. In the indoor case, larger targets were used at points locating furthest away.

The number of points in each distance range is not equal as in ideal circumstances. This is partly due to practical issues dictated by the object scene. In the indoor case, the targets could only be attached on surfaces of wall, doors, or columns, and in the optimized case, only a limited number of special targets were available to be used in the target area.

The proportional accuracy numbers can be drawn from these RMSD values expressing the relative accuracy with respect to the size of the object. Since in this method accuracy is expected to be symmetric with respect to the origin, the maximum dimension of the object can be considered to be twice as big as the distance range depicted in Tables (3) and (4). Regarding this, the proportional accuracy can be calculated to be in the range of $1:1500$ to $1:2000$.

## 6.3 Correlation of parameters

When determining the parameter values, the correlations between parameters need to be considered. In least squares estimation with indirect observations, the correlation of parameters can be problematic. In the case of a high correlation between two parameters, it is hard to separate the influence of observations on values of different correlating parameters in common adjustment. In principle, the correlation of parameters should be dealt with by multivariable analysis, but because of the complexity of computation and analysis of multivariate correlation values, pairwise correlation values are computed instead.

In the following presentation, the pairwise correlations among common block parameters are computed in the optimized case, Table (5-6), and in the interior space case, Table (7-8).

| | $\omega$ | $\phi$ | $\kappa$ | $r$ |
|---|---|---|---|---|
| $\omega$ | 1 | -0.00599 | 0.07982 | -0.01822 |
| $\phi$ | -0.00599 | 1 | 0.11092 | 0.83304 |
| $\kappa$ | 0.07982 | 0.11092 | 1 | -0.14633 |
| $r$ | -0.01822 | 0.83304 | -0.14633 | 1 |

**Table 5.** Optimized case, Experiment I, Block I

| | $\omega$ | $\phi$ | $\kappa$ | $r$ |
|---|---|---|---|---|
| $\omega$ | 1 | 0.00441 | 0.08996 | 0.01817 |
| $\phi$ | 0.00441 | 1 | -0.11274 | 0.82962 |
| $\kappa$ | 0.08996 | -0.11274 | 1 | 0.14760 |
| $r$ | 0.01817 | 0.82962 | 0.14760 | 1 |

**Table 6.** Optimized case, Experiment I, Block II

| | $\omega$ | $\phi$ | $\kappa$ | $r$ |
|---|---|---|---|---|
| $\omega$ | 1 | 0.00201 | 0.10339 | 0.00264 |
| $\phi$ | 0.00201 | 1 | -0.02704 | 0.90343 |
| $\kappa$ | 0.10339 | -0.02704 | 1 | 0.01085 |
| $r$ | 0.00264 | 0.90343 | 0.01085 | 1 |

**Table 7.** Interior space, Experiment II, Block I

In general, the pairwise correlations are quite small except in one case. In both experiments and in both blocks, a high correlation was found between $\phi$- and $r$-parameters. In the interior space case, the correlation was over $0.9$ and in the

| | $\omega$ | $\phi$ | $\kappa$ | $r$ |
|---|---|---|---|---|
| $\omega$ | 1 | -0.00047 | 0.02927 | -0.00066 |
| $\phi$ | -0.00047 | 1 | 0.02684 | 0.91494 |
| $\kappa$ | 0.02927 | 0.02684 | 1 | -0.00816 |
| $r$ | -0.00066 | 0.91494 | -0.00816 | 1 |

**Table 8.** Interior space, Experiment II, Block II

optimized case correlation was of the size of $0.83$. The reason for this high correlation can be deduced from the fact that both parameters have an influence on the scale of measurements, especially when the image plane, is perpendicular to the rotation plane as was the case in both experiments. One reason why the correlated values in the optimized case were lower than in the interior space case is that the distribution of object points in Experiment I was more even than in Experiment II.

When the pairwise correlation of individual camera parameters ($\alpha_i$,$\theta_i$,$\nu_i$) and object coordinate values with common block parameters were computed, no significant correlations were found, see Tables (9-12). In Tables (9-12), values are the mean correlations of parameters. The maximum correlations of camera parameters ($\alpha_i$ , $\theta_i$ , $\nu_i$) between common block parameters were only $0.24$ with the interior space case and $0.22$ with the optimized case. Therefore, these correlations can be considered to be insignificant.

| | $\bar{\alpha}_i$ | $\theta_i$ | $\bar{\nu}_i$ | $X$ | $Y$ | $Z$ |
|---|---|---|---|---|---|---|
| $\omega$ | 0.00289 | 0.11401 | 0.09249 | 0.00428 | 0.01551 | 0.02311 |
| $\phi$ | 0.05676 | 0.02096 | 0.01068 | 0.00754 | 0.03288 | 0.00641 |
| $\kappa$ | 0.00702 | 0.12816 | 0.07603 | 0.00458 | 0.01581 | 0.01847 |
| $r$ | 0.15511 | 0.00876 | 0.00254 | 0.00888 | 0.03688 | 0.00669 |

**Table 9.** Optimized case, Experiment I, Block I

| | $\bar{\alpha}_i$ | $\theta_i$ | $\bar{\nu}_i$ | $\bar{X}$ | $\bar{Y}$ | $\bar{Z}$ |
|---|---|---|---|---|---|---|
| $\omega$ | 0.00420 | 0.11701 | 0.09568 | 0.00394 | 0.01445 | 0.01779 |
| $\phi$ | 0.05600 | 0.02054 | 0.01214 | 0.00962 | 0.03111 | 0.00455 |
| $\kappa$ | 0.00872 | 0.12486 | 0.08183 | 0.00477 | 0.01579 | 0.01717 |
| $r$ | 0.15019 | 0.00904 | 0.00316 | 0.01168 | 0.03639 | 0.00536 |

**Table 10.** Optimized case, Experiment I, Block II

| | $\bar{\alpha}_i$ | $\theta_i$ | $\bar{\nu}_i$ | $X$ | $Y$ | $Z$ |
|---|---|---|---|---|---|---|
| $\omega$ | 0.00306 | 0.13517 | 0.05711 | 0.01186 | 0.01277 | 0.00269 |
| $\phi$ | 0.05133 | 0.00567 | 0.00324 | 0.01055 | 0.00362 | 0.00220 |
| $\kappa$ | 0.01637 | 0.08988 | 0.07867 | 0.01801 | 0.01501 | 0.00408 |
| $r$ | 0.15958 | 0.00561 | 0.00200 | 0.01230 | 0.00415 | 0.00272 |

**Table 11.** Interior space, Experiment II, Block I

| | $\bar{\alpha}_i$ | $\bar{\theta}_i$ | $\bar{\nu}_i$ | $\bar{X}$ | $\bar{Y}$ | $\bar{Z}$ |
|---|---|---|---|---|---|---|
| $\omega$ | 0.00278 | 0.07042 | 0.11645 | 0.01162 | 0.01441 | 0.00373 |
| $\phi$ | 0.04706 | 0.00720 | 0.00200 | 0.00919 | 0.00162 | 0.00237 |
| $\kappa$ | 0.01740 | 0.16176 | 0.04263 | 0.00671 | 0.00487 | 0.00149 |
| $r$ | 0.16522 | 0.00548 | 0.00146 | 0.00985 | 0.00205 | 0.00254 |

**Table 12.** Interior space, Experiment II, Block II

However, when pairwise correlations between camera parameters ($\alpha_i$,$\theta_i$,$\nu_i$) were observed, a high correlation between $\theta_i$- and $\nu_i$-angles was found. The maximum pairwise correlations are depicted in Tables (13) and (14). The high correlation is apparent, since both angles have an effect on the vertical angle of the optical axis. Since these two parameters $\theta_i$and $\nu_i$ have been added into the mathematical model in order to compensate the discrepancy of imaging from the ideal case, the nominal values of these angles do not have real significance as long as deviation from ideal conditions can be compensated, especially when the actual values have been a fraction of a degree.

| $max$ | $\alpha_i$ | $\theta_i$ | $\nu_i$ |
|---|---|---|---|
| $\alpha_i$ | 1 | 0.26630 | 0.17787 |
| $\theta_i$ | 0.26630 | 1 | 0.99159 |
| $\nu_i$ | 0.17787 | 0.99159 | 1 |

| $max$ | $\alpha_i$ | $\theta_i$ | $\nu_i$ |
|---|---|---|---|
| $\alpha_i$ | 1 | 0.19951 | 0.15270 |
| $\theta_i$ | 0.19951 | 1 | 0.99407 |
| $\nu_i$ | 0.15270 | 0.99407 | 1 |

**Table 13.** Optimized case, Experiment I, Block I (left) and Block II (right)

| $max$ | $\alpha_i$ | $\theta_i$ | $\nu_i$ |
|---|---|---|---|
| $\alpha_i$ | 1 | 0.23189 | 0.13985 |
| $\theta_i$ | 0.23189 | 1 | 0.99865 |
| $\nu_i$ | 0.13985 | 0.99865 | 1 |

| $max$ | $\alpha_i$ | $\theta_i$ | $\nu_i$ |
|---|---|---|---|
| $\alpha_i$ | 1 | 0.38489 | 0.18647 |
| $\theta_i$ | 0.38489 | 1 | 0.99510 |
| $\nu_i$ | 0.18647 | 0.99510 | 1 |

**Table 14.** Interior space case, Experiment II,Block I (left) and Block II (right)

The high correlation of the parameters do have affect on determination of the values of parameters in estimation. Therefore, it is sensible to try to reduce the correlation by improving the point distribution and imaging geometry. In order to achieve better determinability of estimates, it is also essential to acquire good initial values of parameters. Fortunately, this can be achieved quite easily with a proper initialization procedure, as described in Section 5.3. During the first stage, the iteration can be carried out by taking only part of the parameters in an adjustment process, and thereafter, with improved parameter values of the first parameter group, release the remaining parameter values for estimation. The acquired initial values for parameters can also be introduced in the estimation process as weighted observations and, this way, support the adjustment not to converge into a local minimum.

## 6.4 Reliability estimates

### 6.4.1 Internal and external reliability

When evaluating the goodness of the mensuration system, it is important to ensure the reliability of estimates. The reliability includes the ability to detect erroneous observations and evaluate the effect of undetected gross errors on estimates. This can be achieved by means of statistical testing. The use of the least squares method does not require any assumptions of distribution or statistical properties of observations. However, while analyzing the residuals of the observation in order to detect possible gross errors, some assumption of their distribution has to be made. By treating the observations as normally distributed, which is a fair assumption, the estimates of the linear least squares become maximum likelihood estimates (Förstner and Molenaar 1986). Also, the estimates are then the best linear unbiased estimates for the unknown parameters. Equally, the distribution of residuals can be assumed to follow normal distribution with zero mean value $v \sim N(0, \sigma_0^2 Q_{vv})$.

The effect of an observational error $\nabla l$ on the residuals can be derived in relation to the *redundancy* matrix $R_e$ (Förstner and Molenaar 1986):

$$\nabla \hat{v} = -R_e \nabla l \tag{50}$$

where $R_e$ depicted in Equation (50) is defined as,

$$R_e = I - A\left(A^T \Sigma_{ll}^{-1} A\right)^{-1} A^T \Sigma_{ll}^{-1} = Q_{\hat{v}\hat{v}} Q_{ll}^{-1} \tag{51}$$

The redundancy matrix denotes the proportion of observational error that is absorbed into residuals. It is essential to notice that an error in one observation

influences all residuals and one residual is influenced by all observational errors. How a large portion of an observational error $\nabla l_i$ affects the corresponding residual $\hat{v}_i$ is depicted by the diagonal element of the redundancy matrix $r_i$. The value of the diagonal element of the $R$ will be between $0$ and $1$. The closer the value is to $1$, the better the localibility of the erroneous observation from the residual values. As can be seen in Equation (51), the structure is highly dependent on the geometry of the measuring system.

In order to detect gross errors via testing of residual values, the calculated residuals are first normalized by their estimated standard deviation. The resulting values are known as *standardized residuals* $\hat{w}_i$:

$$\hat{w}_i = \frac{-\hat{v}_i}{\hat{\sigma}_0 \sqrt{q_{\hat{v}_i \hat{v}_i}}} = \frac{-\hat{v}_i}{\sigma_{l_i} \sqrt{r_i}} \tag{52}$$

In order to test an individual observation, whether it consists of a gross error or not, an assumption needs to be made that the expected value of the individual residual is zero and its distribution follows a normal distribution $v_i \sim N(0, 1)$. The hypothesis test can be expressed as,

$$\begin{aligned} H_0 : &\quad v_i = 0 \\ H_a : &\quad v_i \neq 0 \end{aligned} \tag{53}$$

The test is known as the *Data Snooping* test. This hypothesis testing of residuals is based on the work of Baarda (Baarda 1968). Instead of testing individual residual values, Equation (53), the standardized residuals $\hat{w}_i$ are used as test criteria. The standardized residual can be considered to be a better test criterion than computed residuals $\hat{v}_i$, since it consists of the influence of local geometry (included in value $r_i$ ) on its value; this can be seen from Equation (52). The hypotheses are, therefore:

$H_0$ : $\hat{w}_i$ are from normal distribution or

$H_a$ : a gross error has influence on the value of test statistics $\hat{w}_i$ and the probability density function is shifted by $\delta_i$.

The possible influence $\nabla w_i$ of error in an observation $\nabla l_i$ on test statistics can be derived from Equations (50) and (52) to the form (Förstner and Molenaar 1986):

$$\delta_i = \nabla w_i = \frac{\nabla v_i}{\sigma_{l_i} \sqrt{r_i}} = \frac{\nabla l_i}{\sigma_{l_i}} \sqrt{r_i} \tag{54}$$

It can noted, in Equation (54), that this characteristic of weaker geometry can be summarized as follows: the smaller the redundancy number $r_i$, the smaller

the detectable effect on test statistic $\nabla\hat{w}_i$. A corresponding formulation of the hypotheses can be written as

$$\begin{aligned} H_0: &\quad \hat{w}_i \approx N(0,1) \\ H_a: &\quad \hat{w}_i \approx N(\delta_i,1) \end{aligned} \tag{55}$$

The parameter expressing the shift of the probability density function $\delta_i$, in Equation (55), is also known as the *non-centrality* parameter. The problem is, of course, that the size of an error made in observation $\nabla l_i$ is not known. Therefore, in practice, the power of the test is fixed with a specified significance level and the non-centrality parameter is computed as a result of this selection:

$$\delta_0 = f_\delta(\alpha,\beta) \tag{56}$$

The significance level $1-\alpha$, in Equation (56), expresses the probability of correctly accepting an observation not consisting of an error and the power of the test $\beta$ is a probability of correctly rejecting an erroneous observation. The probabilities and separation $\delta$ of probability density functions of hypotheses $H_0$ and $H_a$ are depicted in Figure (24).

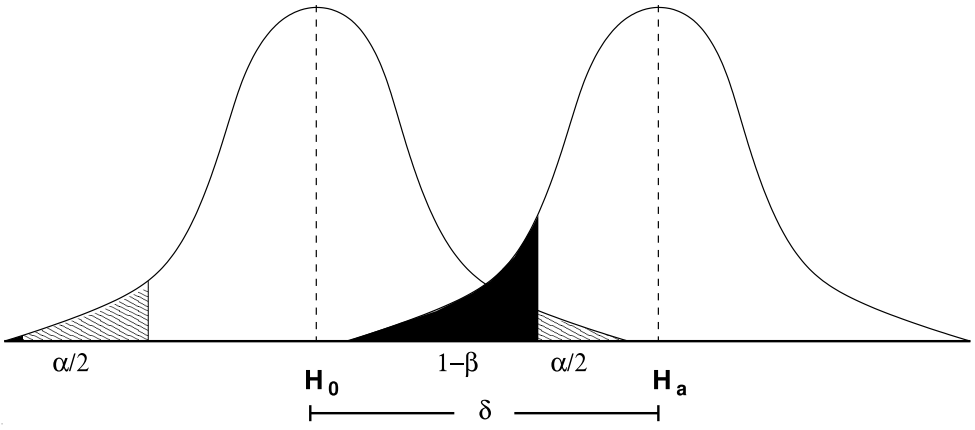


**Figure 24.** Non-centrality $\delta$ of hypotheses $H_0$ and $H_a$ with selected significance level and power of test.

In hypothesis testing there are two types of error that can be made in making a decision of accepting an observation.

*Type I error:* Rejecting a good observation as erroneous.

*Type II error:* Accepting a contaminated observation.

**Internal Reliability:** By using the non-centrality parameter $\delta_0$ solved from statistics, the estimate of the size of a gross error not exceeding the limit of rejecting an observation can be computed:

$$\nabla_0 l_i = \sigma_{l_i} \frac{\delta_0}{\sqrt{r_i}} \tag{57}$$

In other words, it is the size of the error remaining on observations that cannot be detected by using statistical testing with the selected power of the test with an associated significance level. According to Baarda (Baarda 1968), this value is known as the *internal reliability* of the measurements. It can also be seen as a measure of controllability of the observations. The last part of the Equation (57), namely the *controllability factor* $\delta'_{0i}$, is given as

$$\delta'_{0i} = \frac{\delta_0}{\sqrt{r_i}} \tag{58}$$

This is often computed to express the size of the gross error still to be detected with respect to the standard deviation of the observation, see Equation (58). $\delta'_{0i}$ is a useful parameter when evaluating the internal reliability of observations with different types of observation.

**External Reliability:** For continuation of the definition of interior reliability, Baarda presented the concept of *exterior reliability,* which means the maximum influence of undetected gross error on estimates. This influence can be derived by placing the value of the undetected gross error $\nabla_0 l_i$ in the right-hand side of the normal equation in place of the observation:

$$\nabla_0 x_i = N^{-1} A^T P \nabla_0 l_i \tag{59}$$

The exterior reliability values, in Equation (59), can be presented in the matrix where $\nabla L$ presents an $n \times n$ matrix having $\nabla_0 l_i$ values on diagonal $i = 1, 2, ..., n$:

$$\nabla X = N^{-1} A^T P \nabla L \tag{60}$$

In Equation (60), $\nabla X$ will be a $u \times n$ matrix $u$ presenting the number of unknown parameters. However, these values are rather difficult to interpret, therefore more-condensed values are derived from the matrix as the norm of the columns $\nabla x_i$ , $i = 1, 2, ..., n$:

$$\lambda_i^2 = \frac{\nabla x_i^T N \nabla x_i}{\sigma_0^2} \tag{61}$$

This value $\lambda_i$, in Equation (61), shows the amount of the undetected gross error that is absorbed by values of estimates compared to the standard deviation of estimates, and is known as the *sensitivity factor*. It is to be noted that matrix $\nabla X$ does not have to be constructed, since $\lambda_i^2$ can be computed from internal reliability figures:

$$\lambda_i^2 = \nabla l_i \Sigma_{xx}^{-1} \nabla l_i \tag{62}$$

With an assumption that image observations are uncorrelated, Equation (62) can be written as

$$\lambda_i = (1 - r)\, \delta_{0i}' = \sqrt{\frac{1 - r_i}{r_i}}\, \delta_0 \tag{63}$$

This assumption essentially simplifies the computation of sensitivity factors as can be seen from Equation (63).

### 6.4.2 Reliability of experiments

After the adjustment the residuals from the observation equation system were computed. An a posteriori estimate for standard deviation of observations connected with unit weight could be then calculated according to Equation (45). In both experiments, $\hat{\sigma}_0$was $0.23pix$, see Tables (15) and (16), which indicates a fairly good fitness of observation to mathematical model. The mean and maximum residuals and standardized residual values are depicted in Tables (15) and (16). The standardized residuals $w_x$ and $w_y$ are derived from image residuals according to Equation (52) and were used as test variables in hypothesis testing for outlayers.

| $\hat{\sigma}_0 = 0.230$ | $v_x$ | $v_y$ | $w_x$ | $w_y$ |
|---|---|---|---|---|
| $mean$ | 0.15106 | 0.12758 | 0.71427 | 0.62169 |
| $max$ | 0.49674 | 0.57031 | 2.44374 | 2.52473 |

**Table 15.** Residuals & standardized residuals (optimized case, Experiment I)

| $\hat{\sigma}_0 = 0.231$ | $v_x$ | $v_y$ | $w_x$ | $w_y$ |
|---|---|---|---|---|
| $mean$ | 0.17351 | 0.13385 | 0.78091 | 0.62910 |
| $max$ | 0.60747 | 0.54802 | 2.73555 | 2.60769 |

**Table 16.** Residuals & standardized residuals (interior space, Experiment II)

In order to evaluate the imaging system with respect to the reliability of measurements, internal and external reliability numbers were computed. The internal reliability is expressed with a controllability factor $\delta_0'$ which gives the size of the gross error, which still can be detected with respect to the image observation standard deviation. In the computation of controllability factors, the non-centrality parameter $\delta_0$ was determined from statistics, where the power of the test was $\beta = 0.2$ with a significance level $\alpha = 0.001$. According to Inkilä (Inkilä 1996), these are common values used in hypothesis testing of observational errors. In Tables (17) and (18), the minimum, maximum, and mean values of controllability factors $\delta_0'$ are depicted in the first column. In subsequent columns, the sensitivity factors $\lambda$ and redundancy numbers $r$ of observations are depicted respectively. The sensitivity factors are computed according to Equation (63) by assuming the observations to be uncorrelated.

| | $\delta_0'$ | $\lambda$ | $r$ |
|---|---|---|---|
| $min$ | 4.13412 | 0.12877 | 0.27309 |
| $max$ | 7.90719 | 6.74161 | 0.99903 |
| $mean$ | 4.58102 | 1.88799 | 0.82393 |

**Table 17.** Controllability, sensitivity factors and redundancy numbers of observations (optimized case, Experiment I)

| | $\delta_0'$ | $\lambda$ | $r$ |
|---|---|---|---|
| $min$ | 4.13699 | 0.20075 | 0.24881 |
| $max$ | 8.28405 | 7.17991 | 0.99765 |
| $mean$ | 4.39536 | 1.42933 | 0.88810 |

**Table 18.** Controllability, sensitivity factors and redundancy numbers of observations (interior space, Experiment II)

From Tables (17) and (18), it can be seen that the minimum and mean values of controllability factors are of a size that can be expected to be found in a normal close-range photogrammetric case. However, the maximum values are nearly two-times the equivalent minimum values. This indicates an inhomogeneity of measurements. The same phenomenon can be found by observing the sensitivity values, although the mean redundancy values are quite good and typical for the close-range case. In order to examine the internal reliability values more closely, the controllability factors were computed with respect to different object distances. The values were generated from controllability factors corresponding to image observations connected with object points that have fallen in the chosen range category. The chosen presentation can be considered to be fair because of

the nature of the imaging method; in other words, the imaging geometry does change with respect to object distance. In Table (19), the controllability factors are presented for four distance range categories.

| $\delta_0'$ | $< 5$ | $< 10$ | $< 15$ | $< 20$ |
|---|---|---|---|---|
| $min$ | 4.1762 | 4.1341 | 4.1341 | 4.1341 |
| $max$ | 6.1040 | 6.1040 | 7.9072 | 7.9072 |
| $mean$ | 4.6729 | 4.5871 | 4.5962 | 4.5828 |

| $\delta_0'$ | $< 5$ | $< 10$ | $< 15$ | $< 20$ |
|---|---|---|---|---|
| $min$ | 4.1405 | 4.1370 | 4.1370 | 4.1370 |
| $max$ | 5.2073 | 5.3980 | 5.3980 | 8.2841 |
| $mean$ | 4.5346 | 4.4097 | 4.3977 | 4.3954 |

**Table 19.** Controllability factors respect to object distance; Experiment I: Optimized case (upper), Experiment II: Interior space (lower),

What can be seen from Table (19) is that maximum values remain fairly constant up to the last category in the interior space case, but, in the optimized case, the abrupt change in maximum values already appears in the category under $15m$. However, the mean values of controllability factors are nearly the same throughout all distance ranges. One explanation could be that, even though the imaging geometry degrades with respect to object distance, the number of images in sequence increases where the object point can be seen. This means a larger redundancy of estimates.

In order to examine controllability separated into $x$- and $y$-components, a similar presentation of internal reliability divided into range categories was generated, see Tables (20) and (21). The most interesting fact is that maximum values, as well as mean values are, throughout the range categories, larger in $y$-components than in $x$-components. Again, this says something about the imaging geometry: the geometry is stronger in the horizontal direction than in the vertical. This is obvious, since the camera has been rotated on one plane during the imaging sequence. Therefore, it would be a good idea to create a similar imaging sequence on a different level parallel to the first one with a distinctive separation in height.

One general observation regarding the maximum and mean values in Tables (19), (20) and (21) is that they are slightly bigger in the optimized case than in the interior space case. This can be explained by the number of object points included in the measurements. In the optimized case, there were $45$ object points measured, whereas, in the interior space case, the number measured exceeded one hundred.

| $\delta'_{0x}$ | $< 5$ | $< 10$ | $< 15$ | $< 20$ |
|---|---|---|---|---|
| $min$ | 4.3264 | 4.1430 | 4.1430 | 4.1430 |
| $max$ | 5.4133 | 5.6006 | 5.6006 | 5.6006 |
| $mean$ | 4.6870 | 4.5413 | 4.5324 | 4.5082 |

| $\delta'_{0y}$ | $< 5$ | $< 10$ | $< 15$ | $< 20$ |
|---|---|---|---|---|
| $min$ | 4.1762 | 4.1341 | 4.1341 | 4.1341 |
| $max$ | 6.1040 | 6.1040 | 7.9072 | 7.9072 |
| $mean$ | 4.6588 | 4.6329 | 4.6601 | 4.6573 |

**Table 20.** Controllability separated to $x$- and $y$-components (Experiment I, optimized case)

| $\delta'_{0x}$ | $< 5$ | $< 10$ | $< 15$ | $< 20$ |
|---|---|---|---|---|
| $min$ | 4.2078 | 4.1370 | 4.1370 | 4.1370 |
| $max$ | 5.0955 | 5.0955 | 5.0955 | 5.0955 |
| $mean$ | 4.4940 | 4.3179 | 4.3074 | 4.3040 |

| $\delta'_{0y}$ | $< 5$ | $< 10$ | $< 15$ | $< 20$ |
|---|---|---|---|---|
| $min$ | 4.1405 | 4.1405 | 4.1405 | 4.1405 |
| $max$ | 5.2073 | 5.3980 | 5.3980 | 8.2841 |
| $mean$ | 4.5753 | 4.5014 | 4.4880 | 4.4867 |

**Table 21.** Controllability separated to $x$- and $y$-components (Experiment II, interior space)

# 7 DISCUSSION

This novel *Circular Imaging Block* method can be considered to be quite unorthodox from a classical photogrammetric point of view. Traditionally, in close-range photogrammetry, a single object or objects that are distributed in a distinctively bounded area are measured. Imaging is designed to achieve a proper configuration of camera stations, preferably with convergent geometry. Conventionally, multiple camera stations are set up and the camera station geometry is optimized in order to achieve the required accuracy. Iteratively, the geometry of the imaging is redesigned by alternating the multiple factors connected with the design procedure, as described in Section 2.2. All this requires a great deal of expertise and some knowledge of estimation theory.

As opposed to the traditional approach, in this method, the imaging is achieved outwards, inside the object space, i.e. inside scene imaging. The object does not have to be a single object but can be composed of multiple objects distributed around the imaging station. The measurements are made from a single imaging station, although multiple imaging stations can be used and are even recommended, especially if the object space is large and has a complicated structure. Although, in the previous Chapter, accuracy aspects and reliability of the developed system were discussed and analyses were based on solid estimation theory, the use of this method does not require a full understanding of the estimation process. The imaging geometry is basically fixed. Only a few parameters that have some effect on imaging geometry can be altered. This method can therefore be regarded as a *blackbox*-method from the user's point of view. Accuracy-wise, the accuracy achieved in object space is not on the same level as with optimized close-range measurements based on convergent imaging with high-contrast targets. But this has not been the objective of this method. The objective has been to develop and provide a supplemental measuring method for special conditions in close-range photogrammetry, in which traditional methods meet their limitations. However, the achieved accuracy in object space has been found to be at level of $1:1500 - 1:2000$, which is adequate in many applications where the object shape and geometry are to be measured for further analysis. One extra benefit of applying this method, perhaps not emphasized enough, is that all three dimensional object coordinates will be in one and the same coordinate system. Traditionally, when measurements are made in object conditions that fulfill the same characteristics as those for which this novel method is designed, many stereo-models or image bundle blocks have to be constructed, and coordinate transformations made in order to get measurements into a common coordinate system.

## 7.1 Applicability of the method

A distinctive characteristic of the experiments is that the object space has been clearly three dimensional. This property will most likely be the same in many applications. There will be objects quite near the imaging station and some objects will lie at a distance of the outmost range of measuring capability. Conventionally, the imaging in close-range photogrammetry is arranged in such a way that the precision of measurements will be preferably isotropic and with fairly constant size throughout the scene. Unfortunately, the conditions under which this method will be applied hardly ever meet the demand for a uniform image scale, except in some simple cases. Due to imaging geometry no isotropic precision pattern is not to be expected either, if measurements are made form single imaging station. However, by setting up more than one imaging station and planning the locations of the imaging stations inside the object area, a more homogeneous image scale and isotropic precision pattern can be achieved. Another advantage of using multiple imaging stations is the improved measuring geometry, especially over long object distances as exemplified by Figure (25).

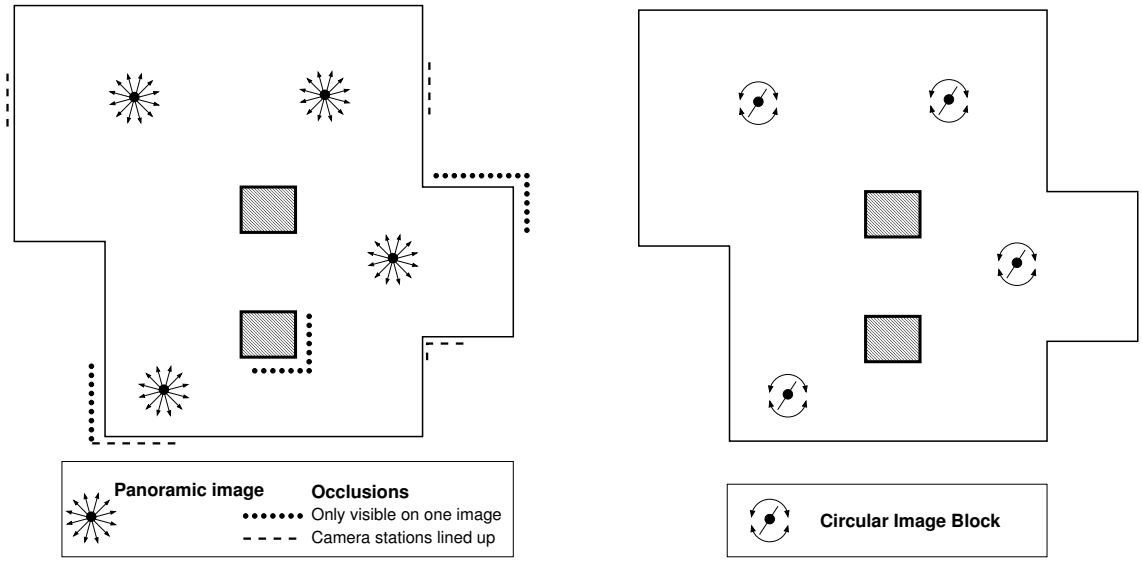


( a ) Panoramic images and possible occlusions

( b ) Circular Image Block without any occlusions

**Figure 25.** Comparison of panoramic imaging and Circular Imaging Blocks in a fictitious indoor environment with obtrusive pillars and extensions.

This, however, requires the relative orientation of imaging stations to be solved as in 3D mapping from panoramic images (Luhmann and Tecklenburg 2004; Schneider and Maas 2005). Applying this method for 3D measurements, object points

can be observed from single imaging station, where image image scale is quite uniform, unlike with panoramic images, where conjugate image observations are always from different imaging stations and therefore can have substantial image scale difference. The uniform image scale can be considered to be advantage when image observations acquisition are to be automated. Also with the same number of imaging stations as in panoramic imaging, the occlusions can be substantially diminished, due to single station measuring capability of this novel method. When 3D measurements are made from panoramic images, the same 3D point has to be seen in at least two images, i.e. from two imaging stations. This is one kind of drawback in the usage of panoramas, since if object space is complex in shape, there can be quite a number of areas that only can be seen on one panoramic image and in this way create occlusions. The object points that are collinear with imaging stations, i.e. two panoramic images lined up with respect to the object, cannot be determined reliably. This is especially so if images are taken on the same level. This is another reason to prefer Circular Imaging Blocks to panoramic imaging for inside scene measurements. In Figure (25) the comparison of panoramic imaging and circular imaging block methods are made with respect to occlusion areas in object measurements.

**Scale determination:** While running the real-world experiments, it was noted that, if only one scale measurement was observed at mean object distance, computed object point coordinates were consistent with reference measurements in short and mean object distances, but, far away, discrepancies were surprisingly large. This is one reason why there were two separate scale measures; one measured between two points with a short distance from imaging station, while the second measured between two points among points locating farthest away. Two separate scale measures seems to be needed in order to determine the scale for measurements adequately and improve the determination of imaging geometry, when there is large variation in object distances. It is recommended, therefore, that at least two scale measures are made if the total distance range exceeds $20m$, and one of these distance measurements is made between points at the farthest distance.

**Illumination:** In the interior space experiment case, the variation of illumination was found to be quite substantial. The effect of insufficient illumination or a large variation of illumination on object measurements can be significant. To achieve an even illumination throughout the object scene is a general problem in all close-range photogrammetric measurements indoors. In order to have some control over the illumination, a source of light could be attached to the navel point of the rotation system. The light source should be directed parallel to camera optical axis. This way, the object will be illuminated similarly in both sequences, at least on images having near a stereo position. However, this is not a comprehensive solution, since in cases where there are objects at close and long distances from camera, i.e., where there is a large image scale variation on a single image frame, the objects closer to the camera will be over-exposured while the farthest objects will be underexposured. Therefore, good general lighting over the whole area

is to be taken care of and additional light sources are to be set to illuminate the farthest objects and possible shadow areas, if this should prove possible.

**Stability of imaging construction:** In this research, the imaging is organized in a controlled way. As has been shown, the original assumption of imaging has not been entirely satisfactory and a few additional parameters have been assimilated into the model to explain the variation from an ideal case. The instability of the rotation system has been found to be the source of the variation. The effect of these disparities on object coordinates have been found to be significant, although variations have not been extensive. In experiments, the longest radius $r$ used while rotating the camera around a navel point has been $50cm$ and, even then, the counter balance has been discovered to be useful in stabilizing the rotation system. In order to improve the stability of the rotation system, a better mechanical design of the system has to be created, as has been achieved in the design of panoramic cameras. Even then, the correction terms to compensate the possible variation from the ideal conditions cannot be totally ignored, as has been stated in papers dealing with this matter (Parian and Gruen 2004; Schneider and Maas 2005).

## 7.2 Direction for further improvement

It has been shown that the measuring system presented in this thesis is functional and object points coordinates can be reliably obtained. The results obtained from real-world experiments have been found to be consistent with results derived from simulations. In order to succeed in the computation of circular imaging block adjustment, the acquisition of good initial values is crucial. Fortunately, with presented instrumentation, the initial values are rather simple to obtain. In adjustment, the initial values have only been treated as starting values of unknown parameters in the estimation of the non-linear least squares system. However, the initial values can also be considered as additional observations in adjustment. The observation equation for radius $r$ estimate can be created in a way that was achieved with the distance observation between two object points. For the angular values, the observation equations can be constructed in a way shown by King (King 1994). When initial values are treated as observations, the question of proper weights has to be considered. Properly weighted observations of parameters can assist in the convergency of computation and eliminate or decrease the effect of correlation between parameters on results. However, if weights of parameter observations are not consistent with weights of other observations, the result of computation can be ambiguous and lead to distortions in object space. Nevertheless, if the effect of the correlation of parameters, especially in this model $\phi$ and $r$, can be diminished, the approach is worthy of investigation.

Correspondingly, the camera system can be calibrated beforehand. In case the camera is statically fixed to a supporting bar, the orientation of camera with respect to rotation plane and length of radius can be determined with system cali-

bration. All that is needed is a three-dimensional calibration field with known object point coordinates. Thereafter, the common block parameters can be treated as known values in an adjustment. Only parameters to be solved in addition to object coordinates are the plane rotation $\alpha_i$ , roll $\theta_i$, and tilt $\nu_i$ values.

Until now, only one camera has been used at one time. It is also possible to use two cameras fixed into each end of the supporting bar. This way both image sequences are obtained simultaneously. If system calibration is performed and common block parameters are solved, also rotation values $\alpha_{1i}$ of the first image block are bound with equivalent $\alpha_{2i}$-values of the second block. This, however, requires that both cameras are triggered off simultaneously. This coupling of $\alpha_{1i}$- and $\alpha_{2i}$-values is meant to improve the determination of $\alpha$-angles in general. A similar relation of roll $\theta_i$- and tilt $\nu_i$-angles can be established, but the coupling is not as unambiguous as with angles $\alpha_i$.

In this research, the only object features that have been dealt with have been points. However, in an indoor environment, the object features most likely to be found are straight lines, regular curves, planes, round pillars, etc. It is natural, therefore, that these features should be included in the estimation model. Either they can be incorporated within the block adjustment while block parameters are to be solved, or they can be used as target features to be measured from known camera positions. The procedure used in image observations of point features is quite suitable for linear features also. The procedure, in which the operator makes initial measurements on one image and the system automatically derives the observation of the same object feature from subsequent images, is quite applicable for guided object modelling. The procedure can be called an *assisted automatic measuring* approach. If lines are measured from an image sequence and the parametric presentation of lines is to be solved as in linear feature photogrammetry (Mulawa and Mikhail 1988; Mulawa 1989; Heikkinen 1994), there could be cases when a solution cannot be found. The lines parallel to the plane on which the camera is rotated cannot be determined if end points of the line are not visible on images. In order to solve this problem, another image sequence pair, whose rotation plane is parallel to the first image sequence pair, should be made. A distinctive separation in the vertical direction also improves the general intersecting geometry.

It was noted earlier in this section that, by using the imaging model presented in this research, some occlusions can be avoided, in contrast to the panoramic imaging approach. However, some occluded areas might still remain, even with careful planning. One option to be seriously considered for future research is the inclusion in common adjustment of stereo pairs that cover the areas of occlusion.

# 8 CONCLUSION

In this thesis, a novel *Circular Imaging Block* method and its mathematical model have been developed. This offers a new approach to close-range photogrammetric object reconstruction, which is most applicable in special circumstances.

Factors affecting the performance of the method have been revealed by the use of computer simulations. The expected accuracy of 3D measurements can thereby be derived from simulations regarding: the quality of image observations, the number of images in a sequence, and the radius of the circle. This will also assist in the design of measurements.

With the help of real-world experiments, the functionality of the developed method has been verified. A refinement to the mathematical model has been made, which also encompasses the possible deviation from an initial model of imaging in practice. Consequently, with the completed mathematical model, an accuracy capability of up to $1:2000$ has been verified with respect to reference data when using an off-the-shelf digital camera. The results can be considered to be adequate in several applications for 3D data acquisition in difficult inside scene measuring cases.

The presented method is designed to be used for measuring the surrounding object space from a single point of location. However, more than one such imaging station can be combined to achieve a more precise and geometrically improved network in terms of measuring accuracy. On the basis of experience obtained in this work, it is recommended that object distances longer than $20m$ should not be measured from a single imaging station; rather, if the maximum dimension of the space exceeds $40m$, multiple imaging stations ought to be established. However, the feasible range of measurements from a single imaging station can be estimated to be between $2-15m$, in general.

A good quality of initial values for parameters has been found to be essential with this method, but this issue can be considered to be quite general in close-range photogrammetry. However, with this method, the requirement is more stringent. Fortunately, the acquisition of initial values for parameters is a straight-forward procedure, which can partly be computerized. Some attention, however, has to be paid to data correctness.

In this work, the measurements from an image sequence have been semi-automated. When acquiring image observations, the knowledge of camera orientation information is exploited. This has led to measuring from a single image while corresponding image observations on subsequent images in the sequence are derived automatically. The single image guided measuring procedure is especially suitable for this kind of imaging approach, where subsequent images do not differ much in their orientation. Characteristics of the procedure have

also been used in measurements of an image block. However, in order to automate the acquisition of observations even more, the use of interest operators and the feature-based matching approach in image block measurements should be seriously considered.

The object measurements made by using this method have been performed without any control points or control features. By applying this method, the coordinates acquired will be directly in the same local coordinate system. This can be regarded as a real benefit because coordinate transformations from one submodel to another are no longer needed.

A further solution has been obtained to the problem of inside scene object modelling, where the design of imaging geometry has been found to be the most challenging task. This method has been created for the purpose of object reconstruction of stationary objects from a moving camera. The design of imaging geometry in this approach has been greatly simplified. One of the reasons for simplification of the design process has been to provide a technique for non-photogrammetrists or inexperienced users to create an image configuration for 3D object measurements. The method can be considered to work like a "blackbox" method, where imaging geometry design can be created without any knowledge of the theoretical background of the method. By means of confined parametrization of camera position and orientation in observation adjustment model, the weakness of imaging geometry has been partly compensated. The use of redundant image observations, i.e., overdetermination, has improved the accuracy in object space positioning and provided a better controllability of measurements compared to the equivalent imaging geometry of present methods.

The objective of the thesis was to obtain a comprehensive answer to the following question:

> *Can a circular imaging block be robust enough and provide object measurements for the purpose of photogrammetric object reconstruction?*

The answer to this question is demonstrably affirmative. A new imaging method has been developed and its mathematical model derived for this difficult case. With refinements the mathematical model has been shown to be consistent with the practical imaging conditions. The feasibility of the method have been demonstrated with real examples and the accuracy of the measurements satisfies the demands of object reconstruction in general.

# References


Ackermann, F. (1984). Digital image correlation: Performance and potential application in photogrammetry, *Photogrammetric Record* **11**(64): 429–439. (Cited on p. 70 and 71.)

Baarda, W. (1968). *A Testing Procedure for Use in Geodetic Networks*, Vol. 2(5), Netherlands Geodetic Commission, p. 97. (Cited on p. 93 and 95.)

Balzani, M., Pellegrinelli, A., Perfetti, N., Russo, P. and Tralli, F. U. S. (2002). Cyrax 2500 laser scanner and g.p.s. operational flexibility: From detailed close range surveying, to urban scale surveying, *in* W. Boehler and P. Patias (eds), *Int. Workshop on Scanning for Cultural Heritage Recording (CD)*, CIPA WG6 and ISPRS Comm. V, Corfu, Greece, pp. 27–32. (Cited on p. 22.)

Bell, J., Squyres, S. W., Herkenhoff, K., Maki, J. N., Arneson, H. M., Brown, D., Collins, S. A., Dingizian, A., Elliot, S. T., Hagerott, E. C., Hayes, A. G., Johnson, M. J., Johnson, J. R., Joseph, J., Kinch, K., Lemmon, M. T., Morris, R. V., Scherr, L., Schwochert, M., Shepard, M. K., Smith, G. H., Shol-Dickstein, J. N., Sullivan, R. J., Sullivan, W. T. and Wadsworth, M. (2003). Mars exploration rover athena panoramic camera (pancam) investigation, *Journal of Geophysical Research* **108**(E12): 30. (Cited on p. 27.)

Beraldin, J.-A., El-Hakim, M. P. S., Godin, G., Latouche, C., Valzano, V. and Bandiera, A. (2002). Expolring a byzantine crypt trough a high resolution texture mapped 3d model: Combining range data and photogrammetry, *in* W. Boehler and P. Patias (eds), *Int. Workshop on Scanning for Cultural Heritage Recording (CD)*, CIPA WG6 and ISPRS Comm. V, Corfu, Greece, pp. 65–72. (Cited on p. 21.)

Boehler, W. and Marbs, A. (2002). 3d scanning instruments, *in* W. Boehler and P. Patias (eds), *Int. Workshop on Scanning for Cultural Heritage Recording (CD)*, CIPA WG6 and ISPRS Comm. V, Corfu, Greece, pp. 9–12. (Cited on p. 20.)

Borg, C. E. and Cannataci, J. A. (2002). Thealasermetry: A hyprid approach to documentation of sites and artefacts, *in* W. Boehler and P. Patias (eds), *Int. Workshop on Scanning for Cultural Heritage Recording (CD)*, CIPA WG6 and ISPRS Comm. V, Corfu, Greece, pp. 93–104. (Cited on p. 22.)

Brenner, C. and Haala, N. (1998). Rapid acuquisition of virtual city models from multiple data sources, *Real-Time Imaging and Dynamic Analysis*, Vol. XXXII, Part 5 of *International Archives of Photogrammetry and Remote Sensing*, ISPRS Symposium Comm. V, Hakodate, Japan, pp. 323–330. (Cited on p. 19.)

Brown, D. C. (1966). Dicentering distortion of lenses, *Photogrammetric Engineering* **32**(3): 444–462. (Cited on p. 47.)

Brown, D. C. (1971). Close-range camera calibration, *Photogrammetric Engineering* **37**(8): 855–866. (Cited on p. 47.)

Brown, D. C. (1976). The bundle method - progress and prospects, *in* K. Löfström and A. Savolainen (eds), *XXI International Congress of ISP*, Vol. XXI, Part 03-03-02 of *International Archives of Photogrammetry*, ISP, Helsinki, Finland, pp. 1–33. (Cited on p. 30.)

Chapman, D., Deacon, A. and Brown, J.-L. (2004). An omnidirectional imaging system for the reverse engineering of industrial facilities, *in* H.-G. Maas and D. Schneider (eds), *Panoramic Photogrammetry Workshop*, Vol. XXXIV, Part 5/W16 of *International Archives of Photogrammetry and Remote Sensing*, ISPRS, Dresden,Germany, p. 8. (Cited on p. 26 and 39.)

Chikatsu, H. and Anai, T. (1998). Relics modeling and visualization in virtual environment, *Real-Time Imaging and Dynamic Analysis*, Vol. XXXII, Part 5 of *International Archives of Photogrammetry and Remote Sensing*, ISPRS Symposium Comm. V, Hakodate, Japan, pp. 528–532. (Cited on p. 18.)

Cooper, M. A. R. and Robson, S. (1996). *Close Range Photogrammetry and Machine Vision*, Whittles Publishing, Chapter Theory of Close Range Photogrammetry, pp. 9–51. (Cited on p. 46.)

El-Hakim, S., Beraldin, J.-A. and Picard, M. (2002). Detailed 3d reconstruction of monuments using multiple techniques, *in* W. Boehler and P. Patias (eds), *Int. Workshop on Scanning for Cultural Heritage Recording (CD)*, CIPA WG6 and ISPRS Comm. V, Corfu, Greece, pp. 58–64. (Cited on p. 21.)

El-Hakim, S. F., Boulanger, P., Blais, F. and Beraldin, J. (1997). A system for indoor 3-d mapping and virtual environments, *in* S. F. El-Hakim (ed.), *Videometrics V*, Vol. 3174, SPIE, pp. 21–35. (Cited on p. 18, 19, 24, and 36.)

El-Hakim, S. F., Brenner, C. and Roth, G. (1998). An approach to creating virtual environments using range and texture, *Real-Time Imaging and Dynamic Analysis*, Vol. XXXII, Part 5 of *International Archives of Photogrammetry and Remote Sensing*, ISPRS Symposium Comm. V, Hakodate, Japan, pp. 331–338. (Cited on p. 18, 19, 24, and 36.)

Foramitti, H. and Ackler, F. (1976). *Emphfelungen für die Anwendung der Photogrammetrie im Denkmalschutz, in der Architektur und Archäologie*, Sonderheft 31 der Österreichishen Zeitschrift für Vermessungswesen und Photogrammetrie, Österreichischer Veraien für Vermessungswesen und Photogrammetrie, p. 78. (Cited on p. 23.)

Förstner, W. (1986). A feature based correspondence algorithm for image matching, *in* E.Kilpelä, A.Savolainen and A.Laiho (eds), *Proceedings of the Symposium from Analytical to Digital*, Vol. XXVI, Part 3/3 of *International Archives of*

*Photogrammetry and Remote Sensing*, ISPRS Symposium Comm. III, Rovaniemi, Finland, pp. 150–166. (Cited on p. 66.)

Förstner, W. and Gülch, E. (1987). A fast operator for detection and precise location of distinct points, corners and centres of circular features, *in* A. Gruen, H. Beyer, Z. Parsic and L. Steinbrückner (eds), *Intercommission Conference on Fast Processing of Photogrammetric Data*, International Archives of Photogrammetry and Remote Sensing, ETH-Hönggerberg, Zürich, Swizerland, pp. 281–305. (Cited on p. 66.)

Förstner, W. and Molenaar, M. (1986). Statistical concepts for quality control (tutorial), Vol. XXVI, Part 3/4 of *International Archives of Photogrammetry and Remote Sensing*, ISPRS Symposium III, Rovaniemi, Finland. (Cited on p. 92 and 93.)

Fraser, C. S. (1982). Optimization of precision in close-range photogrammetry, *Photogrammetric Engineering & Remote Sensing* **48**(4): 561–570. (Cited on p. 29 and 33.)

Fraser, C. S. (1984). Network design considerations for non-topographic photogrammetry, *Photogrammetric Enginering and Remote Sensing* **50**(8): 1115–1126. (Cited on p. 29, 30, 33, 34, 39, and 58.)

Fraser, C. S. (1989). *Non-Topographic Photogrammetry*, second edn, ASPRS, Falls Church, Virginia U.S.A., Chapter Optimatization of networks in non-topographic photogrammetry, pp. 95–106. (Cited on p. 58.)

Fraser, C. S. (1992). Photogrammetric measurement to one part in a million, *Photogrammetric Enginering and Remote Sensing* **58**(3): 305–310. (Cited on p. 22, 29, and 33.)

Fraser, C. S. (1996). *Close Range Photogrammetry and Machine Vision*, Whittles Publishing, Chapter Network design, pp. 256–282. (Cited on p. 29, 30, 33, and 35.)

Fraser, C. S. and Mallison, J. A. (1992). Dimensional characterization of a large aircraft structure by photogrammetry, *Photogrammetric Enginering and Remote Sensing* **58**(5): 539–543. (Cited on p. 35.)

Fryer, J. G., Clarke, T. A. and Chen, J. (1994). Lens distortion for simple c-mount lenses, *Close Range Techniques and Machine Vision*, Vol. XXX, Part 5 of *International Archives of Photogrammetry and Remote Sensing*, ISPRS Symposium Comm. V, Melbourne, Australia, pp. 97–101. (Cited on p. 78.)

Grafarend, E. (1974). Optimisation of geodetic networks, *Bollettino di Geodesia e Scienze Affini* **33**(4): 351–406. (Cited on p. 33 and 34.)

Grün, A. (1996). *Close Range Photogrammetry and Machine Vision*, Whittles Publishing, Chapter Least Squares matching: a Fundamental measurement Algorithm, pp. 217–255. (Cited on p. 70.)

Grün, A. W. and Baltsavias, E. P. (1985). Adaptive least squares correlation with geometrical constraints, *Computer Vision for Robots*, Vol. 595, SPIE, Cannes, pp. 72–82. (Cited on p. 70.)

Guidi, G., Tucci, G., Beraldin, J.-A., Ciofi, S., Damato, V., Ostuni, D., Costantino, F. and Hakim, S. E. (2002). Multiscale archaeological survey based on the integration of 3d scanning and photogrammetry, *in* W. Boehler and P. Patias (eds), *Int. Workshop on Scanning for Cultural Heritage Recording (CD)*, CIPA WG6 and ISPRS Comm. V, Corfu, Greece, pp. 13–18. (Cited on p. 21.)

Haggrén, H. and Mattila, S. (1997). 3-d indoor modeling from videography, *Videometrics V*, Vol. 3174, SPIE, San Diego, California, pp. 14–19. (Cited on p. 23.)

Hartley, R. (1993). Photogrammetric techniques for panoramic cameras, *Itegrateing Photogrammetric Techniques with Scene Analysis and Machine Vision*, Vol. 1944, Orlando, U.S.A., p. 13. (Cited on p. 25.)

Hastedt, H., Luhmann, T. and Tecklenburg, W. (2002). Image-variant interior orientation and sensor modelling of high-quality digital cameras, *in* P. Patias (ed.), *Close-Range Imaging, Long-Range Vision*, Vol. XXXIV, Part 5 of *International Archives of the Photogrammetry, Remote Sensing and Spatial Information Sciences*, ISPRS Symposium Comm. V, Corfu, Greece, p. 6. (Cited on p. 48.)

Heikkinen, J. (1994). Linear feature based approach to map revision., *Mapping and Environmental Applications of GIS Data*, Vol. XXX, Part 4 of *International Archive of Photogrammetry and Remote Sensing*, ISPRS Symposium Comm. IV, Athens, Georgia, U.S.A., pp. 344–351. (Cited on p. 36 and 104.)

Inkilä, K. (1996). *Pienimmän Neliösumman Estimointi*, 2. korjattu painos edn, Teknillinen korkeakoulu, Fotogrammetrian ja kaukokartoituksen laboratorio, Otaniemi, Espoo, Finland, p. 106. (Cited on p. 97.)

Inkilä, K. and Laiho, A. (1989). The minimum-norm solution of a rank-deficient least squares problem by qr-decomposition, *in* L. Mussio (ed.), *Tutorial on "Mathematical Aspects of Data Analysis"*, number InterCommission Working Group III/VI in *International Society for Photogrammetry and Remote Sensing*, ISPRS, Pisa, Italy, pp. 37–47. (Cited on p. 34.)

Ji, Q., Costa, M. S., Haralick, R. M. and Shapiro, L. G. (2000). A robust linear least-squares estimation of camera exterior orientation using multiple geometric features, *ISPRS Journal of Photogrammetry and Remote Sensing* **55**: 75–93. (Cited on p. 36.)

Jiang, G., Wei, Y., Quan, L., tat Tsui, H. and Shum, H. Y. (2005). Outward-looking circular motion analysis of large image sequences, *IEEE Transactions on Pattern Analysis and Machine Intelligence* **27**(2): 271–277. (Cited on p. 26.)

Kang, S. B. and Szeliski, R. (1997). 3-d scene data recovery using omnidirectional multibaseline stereo, *International Journal of Computer Vision* **25**(2): 167–183. (Cited on p. 26.)

Khalil, O. A. and Grussenmeyer, P. (2002). Single image and topology approaches for modeling buildings, *Close-Range Imaging, Long-Range Vision*, Vol. XXXIV, Part 5 of *International Archives of Photogrammetry and Remote Sensing*, ISPRS Symposium Comm. V, Corfu, Greece, pp. 131–136. (Cited on p. 24.)

King, B. A. (1994). *Methods for the Photogrammetric Adjustment of Bundles of Constrained Stereopairs*, PhD thesis, The University of Newcastle, New South Wales, Australia 2308, p. 220. (Cited on p. 36 and 103.)

Knuth, D. E. (1981). *The Art of Computer Programming. Part 2: Seminumerical Algorithms*, Addison-Wesley, Reading, Mass., U.S.A., p. 688. (Cited on p. 59.)

Koistinen, K., Latikka, J. and Pöntinen, P. (2001). The cumulative 3d data collection and management during an archaeological project, *Surveying and Documentation of Historic Buildings, Monuments, Sites - Traditional and Modern Methods*, CIPA, Potsdam, Germany, p. 6. (Cited on p. 18.)

Kukko, A. (2004). A new method for perspective centre alignment for spherical panoramic imaging, *The Photogrammetric Journal of Finland* **19**(1): 37–46. (Cited on p. 25.)

Lapack (2005). Lapack – linear algebra package version 3.0.
http://www.netlib.org/lapack/index.html
(Reference date 27.07.2005) (Cited on p. 72.)

Leroux, C., Even, P., Lottin, A., Gelin, R., Idasiak, J. M., Boissonneau, J. F. and Jeanjacques, M. (2002). Flexible 3-d modelling of hostile environments with constrined viewpoint and multiple unknowns, *in* P. Patias (ed.), *Close-Range Imaging, Long-Range Vision*, Vol. XXXIV, Part 5 of *International Archives of Photogrammetry and Remote Sensing*, ISPRS Symposium Comm. V, Corfu, Greece, pp. 175–180. (Cited on p. 39.)

Lichti, D. D., Gordon, S. J., Steward, M. P., Franke, J. and Tsakiri, M. (2002). Comparison of digital phtogrammetry and laser scaning, *in* W. Boehler and P. Patias (eds), *Int. Workshop on Scanning for Cultural Heritage Recording (CD)*, CIPA WG6 and ISPRS Comm. V, Corfu, Greece, pp. 39–46. (Cited on p. 21.)

Luhmann, T. and Tecklenburg, W. (2002). Bundle orientation and 3-d object reconstruction from multiple-station panoramic imagery, *Close-Range Imaging, Long-Range Vision*, Vol. XXXIV, Part 5 of *International Archives of Photogrammetry and Remote Sensing*, ISPRS Symposium Comm. V, Corfu, Greece, pp. 181–186. (Cited on p. 25.)

Luhmann, T. and Tecklenburg, W. (2004). 3-d object reconstruction from multiple-station panorama imagery, *in* D. S. H-G Maas (ed.), *Panoramic Photogrammetry Workshop*, Vol. XXXIV, Part 5/W16, ISPRS, Dresden,Germany, p. 8. (Cited on p. 26 and 101.)

Maki, J. N., Bell, J., Herkenhoff, K., Squyres, S. W., Kiely, A., Klimesh, M., Schwoshert, M., Litwin, T., Willson, R., Johnson, A., Maimone, M., Baumgartner, E., Collins, A., Wadsworth, M., Elliot, S. T., Dingizian, A., Brown, D., Hagerott, E. C., Scherr, L., Deen, R., Alexander, D. and Lorre, J. (2003). Mars exploration rover engineering cameras, *Journal of Geophysical Research* **108**(E12): 24. (Cited on p. 27.)

Mason, S. O. (1995). Conceptual model of the convergent multistation network configuration task, *Photogrammetric Record* **15**(86): 277–299. (Cited on p. 29, 35, 39, and 58.)

McGlone, C. (1995). Bundle adjustment with object space geometric constarints for site modeling, *Integrating Photogrammetric Techniques with Scene Analysis and Machine Vision II*, Vol. 2486, SPIE, SPIE, pp. 25–35. (Cited on p. 36.)

Mikhail, E. (1976). *Observations and Least Squares*, IEP-A Dun-Donneley, New York, U.S.A., p. 497. (Cited on p. 31, 33, 37, 50, and 55.)

Mikhail, E. M., Bethel, J. S. and McGlone, J. C. (2001). *Introduction to Modern Photogrammetry*, John Wiley & Sons, Inc., p. 479. (Cited on p. 33, 34, 37, 55, 66, and 67.)

Mulawa, D. C. (1989). *Estimation and photogrammetric treatment of linear features*, PhD thesis, Purdue, Ann Arbor, MI, U.S.A., p. 312. (Cited on p. 35 and 104.)

Mulawa, D. C. and Mikhail, E. M. (1988). Photogrammetric treatment of linear features, Vol. XXVII, Part B/3 of *International Archive of Photogrammetry and Remote Sensing*, ISPRS Congress, Kyoto, Japan, pp. 383–393. (Cited on p. 35 and 104.)

Ng, K., Sequeira, V., Butterfield, S., Hogg, D. and Goncalves, J. G. M. (1998). An integrated multi-sensory system for photo-realistic 3d scene reconstruction, *Real-Time Imaging and Dynamic Analysis*, Vol. XXXII, Part 5 of *International Archives of Photogrammetry and Remote Sensing*, ISPRS Symposium Comm. V, Hakodate, Japan, pp. 356–363. (Cited on p. 19 and 21.)

Niini, I. (2000). *Photogrammetric Block Adjustment Based on Singular Correlation*, PhD thesis, Helsinki University of Technology, Otakaari 1, FIN-02015 HUT, Finland, p. 111. (Cited on p. 47.)

Ogleby, C. (2001). Olympia - home of the ancient and modern olympic games a virtual reality three dimensional experience, *Recreating the Past - Visualization and Animation of Cultural Heritage*, Vol. XXXIV, Part 5/W1 of *International Archives of Photogrammetry and Remote Sensing*, p. 5. (Cited on p. 18, 19, and 21.)

Olague, G. (2002). Automated photogrammetric network design using genetic algorithms, *Photogrammetric Engineering & Remote Sensing* **68**(5): 423–431. (Cited on p. 35.)

Parian, J. A. and Gruen, A. (2004). A refined sensor model for panoramic cameras, *in* D. S. H-G Maas (ed.), *Panoramic Photogrammetry Workshop*, Vol. XXXIV, Part 5/W16, ISPRS, Dresden,Germany, p. 12. (Cited on p. 25, 83, and 103.)

Peleg, S. and Ben-Ezra, M. (1999). Stereo panorama with a single camera, *Computer Vision and Pattern Recognition (CVPR)*, IEEE, Fort Collins, Colorado, U.S.A., pp. 1395–1402. (Cited on p. 26 and 54.)

Pollefeys, M., Gool, L. V., Vergauwen, M., Cornelis, K., Verbiest, F. and Tops, J. (2003). 3d capture of archeology and architecture with a hand-held camera, *Vision techniques for digital architectural and archeological archives*, Vol. XXXIV, Part 5/W12 of *International Archives of Photogrammetry and Remote Sensing*, ISPRS, Ancona, Italy, pp. 262–267. (Cited on p. 18, 22, and 39.)

Pollefeys, M., Gool, L. V., Vergauwen, M., Verbiest, F., Cornelis, K., Tops, J. and Koch, R. (2004). Visual modeling with a hand-held camera, *International Journal of Computer Vision* **59**(3): 207–232. (Cited on p. 22, 30, and 39.)

Pollefeys, M., Vergauwen, M. and Gool, L. V. (2000). Automatic 3d modeling from image sequences, Vol. XXXIII, Part B5 of *International Archives of Photogrammetry and Remote Sensing*, ISPRS Congress, Amsterdam, Netherlands, pp. 619–626. (Cited on p. 22 and 39.)

Pöntinen, P. (1999). On the creation of panoramic images from image sequences, *Photogrammetric Journal of Finland* **16**(2): 43–67. (Cited on p. 25 and 39.)

Schenk, T. (1999). *Digital Photogrammetry Volume I*, TerraScience, Laurelville, Ohio, U.S.A., p. 428. (Cited on p. 70.)

Schneider, D. and Maas, H.-G. (2005). Combined bundle adjustment of panoramic and central perspective images, *in* U. K. R. Reulke (ed.), *Panoramic Photogrammetry Workshop*, Vol. XXXVI, Part 5/W8 of *International Archives of Photogrammetry and Remote Sensing*, Berlin, Germany, p. 4. (Cited on p. 25, 26, 101, and 103.)

Schwidefsky, K. and Ackermann, F. (1978). *Fotogrammetria (in Finnish, translated from original "Photogrammetrie", in German)*, seventh edn, Otakustantamo, Espoo, Finland, p. 384. (Cited on p. 36.)

Seales, W. B. and Faugeras, O. D. (1995). Building three-dimensional object models from image seaquence, *Computer Vision and Image Understanding* **61**(3): 308–324. (Cited on p. 19 and 22.)

Seitz, S. M., Kalai, A. and Shum, H.-Y. (2002). Omnivergent stereo, *International Journal of Computer Vision* **48**(3): 159–172. (Cited on p. 27 and 54.)

Sequeira, V., Ng, K., Wolfart, E., Goncalves, J. and Hogg, D. (1999). Automated reconstruction of 3d models from real environments, *ISPRS Journal of Photogrammetry & Remote Sensing* **54**(1): 1–22. (Cited on p. 18 and 21.)

Shortis, M., Ogleby, C., Robson, S., Karalis, E. and Bayer, H. (2001). Calibration modeling and stability testing for the kodak dc200 series digital still camera, *in* S. El-Hakim and A. Gruen (eds), *Videometrics and Optical Methods for 3D Shape Measurements*, Vol. 4309, SPIE, San Jose, CA, U.S.A., pp. 148–153. (Cited on p. 48.)

Shortis, M., Robson, S. and Beyer, H. (1998). Principal point behaviour and calibration parameter models for kodak dcs cameras, *Photogrammetric Record* **16**(92): 165–186. (Cited on p. 48.)

Slama, C. C. (ed.) (1980). *Manual of Photogrammetry*, fourth edn, American Society of Photogrammetry, 105 N. Virginia Ave. Falls Church, Va 22046 U.S.A., p. 1056. (Cited on p. 30, 36, and 51.)

van den Heuvel, F. (2003). *Automation in Architectural Photogrammetry Line-Photogrammetry for the Reconstruction from Single and Multiple Images*, PhD thesis, Techniche Universiteit Delft, The Netherlands, p. 190. (Cited on p. 22.)

van den Heuvel, F. A. (1998). Vanishing point detection for architectural photogrammetry, *Real-Time Imaging and Dynamic Analysis*, Vol. XXXII, Part 5 of *International Archives of Photogrammetry and Remote Sensing*, ISPRS Symposium Comm. V, Hakodate, Japan, pp. 652–659. (Cited on p. 22 and 24.)

Wendt, A. (2004). On the automation of the registration og point clouds using the metropolis algorithm, Vol. XXXV, Part B/3 of *International Archives of Photogrammetry and Remote Sensing*, ISPRS Congress, Istanbul, Turkey, p. 6. (Cited on p. 21.)

Wester-Ebbinghaus, W. (1978). Photogrammetrische punktbestimmung durch bündelausgleichung zur allseitigen erfassung eines räumlichen objektes, *Bildmessung und Luftbildwesen* **46**(6): 198–204. (Cited on p. 30.)

Wester-Ebbinghaus, W. (1982). Single station self calibration mathematical formulation and fisrt experiences, *Precision and Speed in Close Range Photogrammetry*, Vol. XXIV, Part V/2 of *International Archieves of Photogrammetry and Remote Sensing*, ISPRS Symposium Comm. V, Yorks, UK, pp. 533–550. (Cited on p. 25 and 39.)

Youcai, H. and Haralick, R. M. (1999). Testing camera calibration with constraints, *Photogrammetric Engineering & Remote Sensing* **65**(3): 249–258. (Cited on p. 35.)

# APPENDIX I

*This appendix presents the partial derivatives of the observation equation with respect to unknown camera and block parameters as well as object point coordinates.*

**Observation equation**

$$\begin{cases} x = -c\,\dfrac{a_{11}(X_{obj} - r\cos\alpha_i) + a_{12}(Y_{obj} - h) + a_{13}(Z_{obj} + r\sin\alpha_i)}{a_{31}(X_{obj} - r\cos\alpha_i) + a_{32}(Y_{obj} - h) + a_{33}(Z_{obj} + r\sin\alpha_i)} \\ \\ y = -c\,\dfrac{a_{21}(X_{obj} - r\cos\alpha_i) + a_{22}(Y_{obj} - h) + a_{23}(Z_{obj} + r\sin\alpha_i)}{a_{31}(X_{obj} - r\cos\alpha_i) + a_{32}(Y_{obj} - h) + a_{33}(Z_{obj} + r\sin\alpha_i)} \end{cases}$$

*where $h$ is a constant and symbols $a_{jk}$ denote the rotation matrix elements of $R_{\omega_i,\phi_i,\kappa_i}$:*

$$R_{\omega_i,\phi_i,\kappa_i} = R_{\omega_0,\phi_0,\kappa_0} \cdot R_{\alpha_i}$$

*In following equations the observation equation is simplified into a form:*

$$\begin{cases} x = -c\,\dfrac{Zx}{N} \\ \\ y = -c\,\dfrac{Zy}{N} \end{cases}$$

*where $Zx$ denotes the nominators of the fraction depicted in equations $x$, and $Zy$ of $y$ respectively. $N$ is the denominator of the fraction in both equations.*

*In following presentation only partial derivatives of $Zx$, $Zy$ and $N$ are depicted. The final derivatives of observation equation can be computed as*

$$\frac{\partial x}{\partial u} = -c\,\frac{DZxN - DNZx}{N^2}$$

$$\frac{\partial y}{\partial u} = -c\,\frac{DZyN - DNZy}{N^2}$$

*where $u$ denotes the unknown parameter and $DZx$, $DZy$ and $DN$ present equivalent partial derivatives of $Zx$, $Zy$ and $N$ with respect to $u$*

*It is to be noted that in case one would program the equations for the computer, parts of the equations can be substituted by elements of rotation matrices and consequently simplify the programming substantially. The presentation of rotation matrices is also included in this appendix.*

## Partial Derivates with respect to $X_{obj}$

$$\frac{\partial Zx}{\partial X_{obj}} = \cos(\phi)\cos(\kappa)\cos(\alpha) + (\sin(\omega)\sin(\kappa) - \cos(\omega)\sin(\phi)\cos(\kappa))\sin(\alpha)$$

$$\frac{\partial Zy}{\partial X_{obj}} = -\cos(\phi)\sin(\kappa)\cos(\alpha) + (\sin(\omega)\cos(\kappa) + \cos(\omega)\sin(\phi)\sin(\kappa))\sin(\alpha)$$

$$\frac{\partial N}{\partial X_{obj}} = \sin(\phi)\cos(\alpha) + \cos(\omega)\cos(\phi)\sin(\alpha)$$

### Partial Derivates with respect to $Y_{obj}$

$$\frac{\partial Zx}{\partial Y_{obj}} = \cos(\omega)\sin(\kappa) + \sin(\omega)\sin(\phi)\cos(\kappa)$$

$$\frac{\partial Zy}{\partial Y_{obj}} = \cos(\omega)\cos(\kappa) - \sin(\omega)\sin(\phi)\sin(\kappa)$$

$$\frac{\partial N}{\partial Y_{obj}} = -\sin(\omega)\cos(\phi)$$

## Partial Derivates with respect to $Z_{obj}$

$$\frac{\partial Zx}{\partial Z_{obj}} = -\cos(\phi)\cos(\kappa)\sin(\alpha) + (\sin(\omega)\sin(\kappa) - \cos(\omega)\sin(\phi)\cos(\kappa))\cos(\alpha)$$

$$\frac{\partial Zy}{\partial Z_{obj}} = \cos(\phi)\sin(\kappa)\sin(\alpha) + (\sin(\omega)\cos(\kappa) + \cos(\omega)\sin(\phi)\sin(\kappa))\cos(\alpha)$$

$$\frac{\partial N}{\partial Z_{obj}} = -\sin(\phi)\sin(\alpha) + \cos(\omega)\cos(\phi)\cos(\alpha)$$

## Partial Derivates with respect to $\omega$

$$\frac{\partial Zx}{\partial \omega} = \sin(\alpha)\left(\cos(\omega)\sin(\kappa) + \sin(\omega)\sin(\phi)\cos(\kappa)\right)\left(Xg - r\cos(\alpha)\right) + \left(-\sin(\omega)\sin(\kappa) + \cos(\omega)\sin(\phi)\cos(\kappa)\right) Yg + \cos(\alpha)\left(\cos(\omega)\sin(\kappa) + \sin(\omega)\sin(\phi)\cos(\kappa)\right)\left(Zg + r\sin(\alpha)\right)$$

$$\frac{\partial Zy}{\partial \omega} = \left(\cos(\omega)\cos(\kappa) - \sin(\omega)\sin(\phi)\sin(\kappa)\right)\sin(\alpha)\left(Xg - r\cos(\alpha)\right) + \left(-\sin(\omega)\cos(\kappa) - \cos(\omega)\sin(\phi)\sin(\kappa)\right) Yg + \left(\cos(\omega)\cos(\kappa) - \sin(\omega)\sin(\phi)\sin(\kappa)\right)\cos(\alpha)\left(Zg + r\sin(\alpha)\right)$$

$$\frac{\partial N}{\partial \omega} = -\sin(\alpha)\sin(\omega)\cos(\phi)\left(Xg - r\cos(\alpha)\right) - \cos(\omega)\cos(\phi)\, Yg - \cos(\alpha)\sin(\omega)\cos(\phi)\left(Zg + r\sin(\alpha)\right)$$

## Partial Derivates with respect to $\phi$

$$\frac{\partial Zx}{\partial \phi} = (-\sin(\phi)\cos(\kappa)\cos(\alpha) - \cos(\omega)\cos(\phi)\cos(\kappa)\sin(\alpha))\,(Xg - r\cos(\alpha)) + \sin(\omega)\cos(\phi)\cos(\kappa)\;Yg +$$
$$(\sin(\phi)\cos(\kappa)\sin(\alpha) - \cos(\omega)\cos(\phi)\cos(\kappa)\cos(\alpha))\,(Zg + r\sin(\alpha))$$

$$\frac{\partial Zy}{\partial \phi} = (\sin(\phi)\sin(\kappa)\cos(\alpha) + \cos(\omega)\cos(\phi)\sin(\kappa)\sin(\alpha))\,(Xg - r\cos(\alpha)) - \sin(\omega)\cos(\phi)\sin(\kappa)\;Yg +$$
$$(-\sin(\phi)\sin(\kappa)\sin(\alpha) + \cos(\omega)\cos(\phi)\sin(\kappa)\cos(\alpha))\,(Zg + r\sin(\alpha))$$

$$\frac{\partial N}{\partial \phi} = (\cos(\phi)\cos(\alpha) - \cos(\omega)\sin(\phi)\sin(\alpha))\,(Xg - r\cos(\alpha)) + \sin(\omega)\sin(\phi)\;Yg +$$
$$(-\cos(\phi)\sin(\alpha) - \cos(\omega)\sin(\phi)\cos(\alpha))\,(Zg + r\sin(\alpha))$$

## Partial Derivates with respect to $\kappa$

$$\begin{aligned}\frac{\partial Zx}{\partial \kappa} = &(-\cos(\phi)\sin(\kappa)\cos(\alpha) + (\sin(\omega)\cos(\kappa) + \cos(\omega)\sin(\phi)\sin(\kappa))\sin(\alpha))\,(Xg - r\cos(\alpha)) + \\ &(\cos(\omega)\cos(\kappa) - \sin(\omega)\sin(\phi)\sin(\kappa))\;Yg + \\ &(\cos(\phi)\sin(\kappa)\sin(\alpha) + (\sin(\omega)\cos(\kappa) + \cos(\omega)\sin(\phi)\sin(\kappa))\cos(\alpha))\,(Zg + r\sin(\alpha))\end{aligned}$$

$$\begin{aligned}\frac{\partial Zy}{\partial \kappa} = &(-\cos(\phi)\cos(\kappa)\cos(\alpha) + (-\sin(\omega)\sin(\kappa) + \cos(\omega)\sin(\phi)\cos(\kappa))\sin(\alpha))\,(Xg - r\cos(\alpha)) + \\ &(-\cos(\omega)\sin(\kappa) - \sin(\omega)\sin(\phi)\cos(\kappa))\;Yg + \\ &(\cos(\phi)\cos(\kappa)\sin(\alpha) + (-\sin(\omega)\sin(\kappa) + \cos(\omega)\sin(\phi)\cos(\kappa))\cos(\alpha))\,(Zg + r\sin(\alpha))\end{aligned}$$

$$\frac{\partial N}{\partial \kappa} = 0$$

## Partial Derivates with respect to radius $r$

$$\frac{\partial Zx}{\partial r} = -\left(\cos\left(\phi\right)\cos\left(\kappa\right)\cos\left(\alpha\right) + \left(\sin\left(\omega\right)\sin\left(\kappa\right) - \cos\left(\omega\right)\sin\left(\phi\right)\cos\left(\kappa\right)\right)\sin\left(\alpha\right)\right)\cos\left(\alpha\right) + \left(-\cos\left(\phi\right)\cos\left(\kappa\right)\sin\left(\alpha\right) + \left(\sin\left(\omega\right)\sin\left(\kappa\right) - \cos\left(\omega\right)\sin\left(\phi\right)\cos\left(\kappa\right)\right)\cos\left(\alpha\right)\right)\sin\left(\alpha\right)$$

$$\frac{\partial Zy}{\partial r} = -\left(-\cos\left(\phi\right)\sin\left(\kappa\right)\cos\left(\alpha\right) + \left(\sin\left(\omega\right)\cos\left(\kappa\right) + \cos\left(\omega\right)\sin\left(\phi\right)\sin\left(\kappa\right)\right)\sin\left(\alpha\right)\right)\cos\left(\alpha\right) + \left(\cos\left(\phi\right)\sin\left(\kappa\right)\sin\left(\alpha\right) + \left(\sin\left(\omega\right)\cos\left(\kappa\right) + \cos\left(\omega\right)\sin\left(\phi\right)\sin\left(\kappa\right)\right)\cos\left(\alpha\right)\right)\sin\left(\alpha\right)$$

$$\frac{\partial N}{\partial r} = -\left(\sin\left(\phi\right)\cos\left(\alpha\right) + \cos\left(\omega\right)\cos\left(\phi\right)\sin\left(\alpha\right)\right)\cos\left(\alpha\right) + \left(-\sin\left(\phi\right)\sin\left(\alpha\right) + \cos\left(\omega\right)\cos\left(\phi\right)\cos\left(\alpha\right)\right)\sin\left(\alpha\right)$$

## Partial Derivates with respect to $\alpha$

$$\begin{aligned}\frac{\partial Zx}{\partial \alpha} = &\left(-\cos\left(\phi\right)\cos\left(\kappa\right)\sin\left(\alpha\right)+\left(\sin\left(\omega\right)\sin\left(\kappa\right)-\cos\left(\omega\right)\sin\left(\phi\right)\cos\left(\kappa\right)\right)\cos\left(\alpha\right)\right)\left(Xg-r\cos\left(\alpha\right)\right)+\\ &\left(\cos\left(\phi\right)\cos\left(\kappa\right)\cos\left(\alpha\right)+\left(\sin\left(\omega\right)\sin\left(\kappa\right)-\cos\left(\omega\right)\sin\left(\phi\right)\cos\left(\kappa\right)\right)\sin\left(\alpha\right)\right)r\sin\left(\alpha\right)+\\ &\left(-\cos\left(\phi\right)\cos\left(\kappa\right)\cos\left(\alpha\right)-\left(\sin\left(\omega\right)\sin\left(\kappa\right)-\cos\left(\omega\right)\sin\left(\phi\right)\cos\left(\kappa\right)\right)\sin\left(\alpha\right)\right)\left(Zg+r\sin\left(\alpha\right)\right)+\\ &\left(-\cos\left(\phi\right)\cos\left(\kappa\right)\sin\left(\alpha\right)+\left(\sin\left(\omega\right)\sin\left(\kappa\right)-\cos\left(\omega\right)\sin\left(\phi\right)\cos\left(\kappa\right)\right)\cos\left(\alpha\right)\right)r\cos\left(\alpha\right)\end{aligned}$$

$$\begin{aligned}\frac{\partial Zy}{\partial \alpha} = &\left(\cos\left(\phi\right)\sin\left(\kappa\right)\sin\left(\alpha\right)+\left(\sin\left(\omega\right)\cos\left(\kappa\right)+\cos\left(\omega\right)\sin\left(\phi\right)\sin\left(\kappa\right)\right)\cos\left(\alpha\right)\right)\left(Xg-r\cos\left(\alpha\right)\right)+\\ &\left(-\cos\left(\phi\right)\sin\left(\kappa\right)\cos\left(\alpha\right)+\left(\sin\left(\omega\right)\cos\left(\kappa\right)+\cos\left(\omega\right)\sin\left(\phi\right)\sin\left(\kappa\right)\right)\sin\left(\alpha\right)\right)r\sin\left(\alpha\right)+\\ &\left(\cos\left(\phi\right)\sin\left(\kappa\right)\cos\left(\alpha\right)-\left(\sin\left(\omega\right)\cos\left(\kappa\right)+\cos\left(\omega\right)\sin\left(\phi\right)\sin\left(\kappa\right)\right)\sin\left(\alpha\right)\right)\left(Zg+r\sin\left(\alpha\right)\right)+\\ &\left(\cos\left(\phi\right)\sin\left(\kappa\right)\sin\left(\alpha\right)+\left(\sin\left(\omega\right)\cos\left(\kappa\right)+\cos\left(\omega\right)\sin\left(\phi\right)\sin\left(\kappa\right)\right)\cos\left(\alpha\right)\right)r\cos\left(\alpha\right)\end{aligned}$$

$$\begin{aligned}\frac{\partial N}{\partial \alpha} = &\left(-\sin\left(\phi\right)\sin\left(\alpha\right)+\cos\left(\omega\right)\cos\left(\phi\right)\cos\left(\alpha\right)\right)\left(Xg-r\cos\left(\alpha\right)\right)+\left(\sin\left(\phi\right)\cos\left(\alpha\right)+\cos\left(\omega\right)\cos\left(\phi\right)\sin\left(\alpha\right)\right)r\sin\left(\alpha\right)+\\ &\left(-\sin\left(\phi\right)\cos\left(\alpha\right)-\cos\left(\omega\right)\cos\left(\phi\right)\sin\left(\alpha\right)\right)\left(Zg+r\sin\left(\alpha\right)\right)+\left(-\sin\left(\phi\right)\sin\left(\alpha\right)+\cos\left(\omega\right)\cos\left(\phi\right)\cos\left(\alpha\right)\right)r\cos\left(\alpha\right)\end{aligned}$$

## Rotation matrix $R_{\omega,\phi,\kappa}$

$$
\begin{aligned}
R_{00} &= \cos(\phi)\cos(\kappa) \\
R_{01} &= \sin(\omega)\sin(\phi)\cos(\kappa) + \cos(\omega)\sin(\kappa) \\
R_{02} &= -\cos(\omega)\sin(\phi)\cos(\kappa) + \sin(\omega)\sin(\kappa) \\
R_{10} &= -\cos(\phi)\sin(\kappa) \\
R_{11} &= -\sin(\omega)\sin(\phi)\sin(\kappa) + \cos(\omega)\cos(\kappa) \\
R_{12} &= \cos(\omega)\sin(\phi)\sin(\kappa) + \sin(\omega)\cos(\kappa) \\
R_{20} &= \sin(\phi) \\
R_{21} &= -\sin(\omega)\cos(\phi) \\
R_{22} &= \cos(\omega)\cos(\phi)
\end{aligned}
$$

## Rotation matrix $R_{\alpha_i}$

$$
R_{\alpha_i} = \begin{bmatrix} \cos\alpha_i & 0 & -\sin\alpha_i \\ 0 & 1 & 0 \\ \sin\alpha_i & 0 & \cos\alpha_i \end{bmatrix}
$$

## Rotation matrix $R_i = R_{\omega,\phi,\kappa} R_{\alpha_i}$

$$
\begin{aligned}
Ri_{00} &= \cos(\phi)\cos(\kappa)\cos(\alpha) + (\sin(\omega)\sin(\kappa) - \cos(\omega)\sin(\phi)\cos(\kappa))\sin(\alpha) \\
Ri_{00} &= \cos(\omega)\sin(\kappa) + \sin(\omega)\sin(\phi)\cos(\kappa) \\
Ri_{00} &= -\cos(\phi)\cos(\kappa)\sin(\alpha) + (\sin(\omega)\sin(\kappa) - \cos(\omega)\sin(\phi)\cos(\kappa))\cos(\alpha) \\
Ri_{00} &= -\cos(\phi)\sin(\kappa)\cos(\alpha) + (\sin(\omega)\cos(\kappa) + \cos(\omega)\sin(\phi)\sin(\kappa))\sin(\alpha) \\
Ri_{00} &= \cos(\omega)\cos(\kappa) - \sin(\omega)\sin(\phi)\sin(\kappa) \\
Ri_{00} &= \cos(\phi)\sin(\kappa)\sin(\alpha) + (\sin(\omega)\cos(\kappa) + \cos(\omega)\sin(\phi)\sin(\kappa))\cos(\alpha) \\
Ri_{00} &= \sin(\phi)\cos(\alpha) + \cos(\omega)\cos(\phi)\sin(\alpha) \\
Ri_{00} &= -\sin(\omega)\cos(\phi) \\
Ri_{00} &= -\sin(\phi)\sin(\alpha) + \cos(\omega)\cos(\phi)\cos(\alpha)
\end{aligned}
$$

# APPENDIX II

*This appendix presents the partial derivatives of the observation equation with respect to unknown camera and block parameters as well as object point coordinates.*

**Observation equation**

$$\begin{cases} x = -c\,\dfrac{a_{11}(X_{obj} - r\cos\alpha_i \cdot \cos\theta_i) + a_{12}(Y_{obj} - r \cdot \sin\theta_i) + a_{13}(Z_{obj} + r\sin\alpha_i \cdot \cos\theta_i)}{a_{31}(X_{obj} - r\cos\alpha_i \cdot \cos\theta_i) + a_{32}(Y_{obj} - r \cdot \sin\theta_i) + a_{33}(Z_{obj} + r\sin\alpha_i \cdot \cos\theta_i)} \\ y = -c\,\dfrac{a_{21}(X_{obj} - r\cos\alpha_i \cdot \cos\theta_i) + a_{22}(Y_{obj} - r \cdot \sin\theta_i) + a_{23}(Z_{obj} + r\sin\alpha_i \cdot \cos\theta_i)}{a_{31}(X_{obj} - r\cos\alpha_i \cdot \cos\theta_i) + a_{32}(Y_{obj} - r \cdot \sin\theta_i) + a_{33}(Z_{obj} + r\sin\alpha_i \cdot \cos\theta_i)} \end{cases}$$

*where symbols $a_{jk}$ denote the rotation matrix elements of $R_{\omega_i,\phi_i,\kappa_i}$:*

$$R_{\omega_i,\phi_i,\kappa_i} = R_{\omega_0,\phi_0,\kappa_0} \cdot R_{\alpha_i,\nu_i,\theta_i}$$

*In following equations the observation equation is simplified into a form:*

$$\begin{cases} x = -c\,\dfrac{Zx}{N} \\ y = -c\,\dfrac{Zy}{N} \end{cases}$$

*where $Zx$ denotes the nominators of the fraction depicted in equations $x$, and $Zy$ of $y$ respectively. $N$ is the denominator of the fraction in both equations.*

*In following presentation only partial derivatives of $Zx$, $Zy$ and $N$ are depicted. The final derivatives of observation equation can be computed as*

$$\frac{\partial x}{\partial u} = -c\,\frac{DZxN - DNZx}{N^2}$$

$$\frac{\partial y}{\partial u} = -c\,\frac{DZyN - DNZy}{N^2}$$

*where $u$ denotes the unknown parameter and $DZx$, $DZy$ and $DN$ present equivalent partial derivatives of $Zx$, $Zy$ and $N$ with respect to $u$*

*It is to be noted that in case one would program the equations for the computer, parts of the equations can be substituted by elements of rotation matrices and consequently simplify the programming substantially. The presentation of rotation matrices is also included in this appendix.*

## Partial Derivates with respect to $X_{obj}$

$$\frac{\partial Zx}{\partial X_{obj}} = \cos(\phi)\cos(\kappa)(\cos(\theta)\cos(\alpha) + \sin(\nu)\sin(\alpha)\sin(\theta)) +$$
$$(\sin(\omega)\sin(\phi)\cos(\kappa) + \cos(\omega)\sin(\kappa))(-\sin(\theta)\cos(\alpha) + \sin(\nu)\sin(\alpha)\cos(\theta)) +$$
$$(-\cos(\omega)\sin(\phi)\cos(\kappa) + \sin(\omega)\sin(\kappa))\cos(\nu)\sin(\alpha)$$

$$\frac{\partial Zy}{\partial X_{obj}} = -\cos(\phi)\sin(\kappa)(\cos(\theta)\cos(\alpha) + \sin(\nu)\sin(\alpha)\sin(\theta)) +$$
$$(-\sin(\omega)\sin(\phi)\sin(\kappa) + \cos(\omega)\cos(\kappa))(-\sin(\theta)\cos(\alpha) + \sin(\nu)\sin(\alpha)\cos(\theta)) +$$
$$(\cos(\omega)\sin(\phi)\sin(\kappa) + \sin(\omega)\cos(\kappa))\cos(\nu)\sin(\alpha)$$

$$\frac{\partial N}{\partial X_{obj}} = \sin(\phi)(\cos(\theta)\cos(\alpha) + \sin(\nu)\sin(\alpha)\sin(\theta)) -$$
$$\sin(\omega)\cos(\phi)(-\sin(\theta)\cos(\alpha) + \sin(\nu)\sin(\alpha)\cos(\theta)) + \cos(\omega)\cos(\phi)\cos(\nu)\sin(\alpha)$$

## Partial Derivates with respect to $Y_{obj}$

$$\frac{\partial Zx}{\partial Y_{obj}} = \cos(\phi)\cos(\kappa)\sin(\theta)\cos(\nu) + (\sin(\omega)\sin(\phi)\cos(\kappa) + \cos(\omega)\sin(\kappa))\cos(\theta)\cos(\nu) - (-\cos(\omega)\sin(\phi)\cos(\kappa) + \sin(\omega)\sin(\kappa))\sin(\nu)$$

$$\frac{\partial Zy}{\partial Y_{obj}} = -\cos(\phi)\sin(\kappa)\sin(\theta)\cos(\nu) + (-\sin(\omega)\sin(\phi)\sin(\kappa) + \cos(\omega)\cos(\kappa))\cos(\theta)\cos(\nu) - (\cos(\omega)\sin(\phi)\sin(\kappa) + \sin(\omega)\cos(\kappa))\sin(\nu)$$

$$\frac{\partial N}{\partial Y_{obj}} = \sin(\phi)\sin(\theta)\cos(\nu) - \sin(\omega)\cos(\phi)\cos(\theta)\cos(\nu) - \cos(\omega)\cos(\phi)\sin(\nu)$$

## Partial Derivates with respect to $Z_{obj}$

$$\frac{\partial Zx}{\partial Z_{obj}} = \cos(\phi)\cos(\kappa)\left(-\cos(\theta)\sin(\alpha) + \sin(\theta)\sin(\nu)\cos(\alpha)\right) +$$
$$\left(\sin(\omega)\sin(\phi)\cos(\kappa) + \cos(\omega)\sin(\kappa)\right)\left(\sin(\theta)\sin(\alpha) + \cos(\theta)\sin(\nu)\cos(\alpha)\right) +$$
$$\left(-\cos(\omega)\sin(\phi)\cos(\kappa) + \sin(\omega)\sin(\kappa)\right)\cos(\nu)\cos(\alpha)$$

$$\frac{\partial Zy}{\partial Z_{obj}} = -\cos(\phi)\sin(\kappa)\left(-\cos(\theta)\sin(\alpha) + \sin(\theta)\sin(\nu)\cos(\alpha)\right) +$$
$$\left(-\sin(\omega)\sin(\phi)\sin(\kappa) + \cos(\omega)\cos(\kappa)\right)\left(\sin(\theta)\sin(\alpha) + \cos(\theta)\sin(\nu)\cos(\alpha)\right) +$$
$$\left(\cos(\omega)\sin(\phi)\sin(\kappa) + \sin(\omega)\cos(\kappa)\right)\cos(\nu)\cos(\alpha)$$

$$\frac{\partial N}{\partial Z_{obj}} = \sin(\phi)\left(-\cos(\theta)\sin(\alpha) + \sin(\theta)\sin(\nu)\cos(\alpha)\right) -$$
$$\sin(\omega)\cos(\phi)\left(\sin(\theta)\sin(\alpha) + \cos(\theta)\sin(\nu)\cos(\alpha)\right) + \cos(\omega)\cos(\phi)\cos(\nu)\cos(\alpha)$$

## Partial Derivates with respect to $\omega$

$$\begin{aligned}\frac{\partial Zx}{\partial \omega} =&((\cos(\omega)\sin(\phi)\cos(\kappa)-\sin(\omega)\sin(\kappa))(-\sin(\theta)\cos(\alpha)+\sin(\nu)\sin(\alpha)\cos(\theta))+\\&(\sin(\omega)\sin(\phi)\cos(\kappa)+\cos(\omega)\sin(\kappa))\cos(\nu)\sin(\alpha))(X_{obj}-r\ \cos(\alpha)\cos(\theta))+\\&((\cos(\omega)\sin(\phi)\cos(\kappa)-\sin(\omega)\sin(\kappa))\cos(\theta)\cos(\nu)-(\sin(\omega)\sin(\phi)\cos(\kappa)+\cos(\omega)\sin(\kappa))\sin(\nu))(Y_{obj}-r\ \sin(\theta))+\\&((\cos(\omega)\sin(\phi)\cos(\kappa)-\sin(\omega)\sin(\kappa))(\sin(\theta)\sin(\alpha)+\cos(\theta)\sin(\nu)\cos(\alpha))+\\&(\sin(\omega)\sin(\phi)\cos(\kappa)+\cos(\omega)\sin(\kappa))\cos(\nu)\cos(\alpha))(Z_{obj}+r\ \sin(\alpha)\cos(\theta))\end{aligned}$$

$$\begin{aligned}\frac{\partial Zy}{\partial \omega} =&((-\cos(\omega)\sin(\phi)\sin(\kappa)-\sin(\omega)\cos(\kappa))(-\sin(\theta)\cos(\alpha)+\sin(\nu)\sin(\alpha)\cos(\theta))+\\&(-\sin(\omega)\sin(\phi)\sin(\kappa)+\cos(\omega)\cos(\kappa))\cos(\nu)\sin(\alpha))(X_{obj}-r\ \cos(\alpha)\cos(\theta))+\\&((-\cos(\omega)\sin(\phi)\sin(\kappa)-\sin(\omega)\cos(\kappa))\cos(\theta)\cos(\nu)-(-\sin(\omega)\sin(\phi)\sin(\kappa)+\cos(\omega)\cos(\kappa))\sin(\nu))(Y_{obj}-r\ \sin(\theta))+\\&((-\cos(\omega)\sin(\phi)\sin(\kappa)-\sin(\omega)\cos(\kappa))(\sin(\theta)\sin(\alpha)+\cos(\theta)\sin(\nu)\cos(\alpha))+\\&(-\sin(\omega)\sin(\phi)\sin(\kappa)+\cos(\omega)\cos(\kappa))\cos(\nu)\cos(\alpha))(Z_{obj}+r\ \sin(\alpha)\cos(\theta))\end{aligned}$$

$$\begin{aligned}\frac{\partial N}{\partial \omega} =&(-\cos(\omega)\cos(\phi)(-\sin(\theta)\cos(\alpha)+\sin(\nu)\sin(\alpha)\cos(\theta))-\sin(\omega)\cos(\phi)\cos(\nu)\sin(\alpha))(X_{obj}-r\ \cos(\alpha)\cos(\theta))+\\&(-\cos(\omega)\cos(\phi)\cos(\theta)\cos(\nu)+\sin(\omega)\cos(\phi)\sin(\nu))(Y_{obj}-r\ \sin(\theta))+\\&(-\cos(\omega)\cos(\phi)(\sin(\theta)\sin(\alpha)+\cos(\theta)\sin(\nu)\cos(\alpha))-\sin(\omega)\cos(\phi)\cos(\nu)\cos(\alpha))(Z_{obj}+r\ \sin(\alpha)\cos(\theta))\end{aligned}$$

## Partial Derivates with respect to $\phi$

$$\begin{aligned}\frac{\partial Zx}{\partial \phi} =&(-\sin(\phi)\cos(\kappa)(\cos(\theta)\cos(\alpha)+\sin(\nu)\sin(\alpha)\sin(\theta))+\sin(\omega)\cos(\phi)\cos(\kappa)(-\sin(\theta)\cos(\alpha)+\sin(\nu)\sin(\alpha)\cos(\theta))\\&-\cos(\omega)\cos(\phi)\cos(\kappa)\cos(\nu)\sin(\alpha))(X_{obj}-r\ \cos(\alpha)\cos(\theta))+\\&(-\sin(\phi)\cos(\kappa)\sin(\theta)\cos(\nu)+\sin(\omega)\cos(\phi)\cos(\kappa)\cos(\theta)\cos(\nu)+\cos(\omega)\cos(\phi)\cos(\kappa)\sin(\nu))(Y_{obj}-r\ \sin(\theta))+\\&(-\sin(\phi)\cos(\kappa)(-\cos(\theta)\sin(\alpha)+\sin(\theta)\sin(\nu)\cos(\alpha))+\sin(\omega)\cos(\phi)\cos(\kappa)(\sin(\theta)\sin(\alpha)+\cos(\theta)\sin(\nu)\cos(\alpha))-\\&\cos(\omega)\cos(\phi)\cos(\kappa)\cos(\nu)\cos(\alpha))(Z_{obj}+r\ \sin(\alpha)\cos(\theta))\end{aligned}$$

$$\begin{aligned}\frac{\partial Zy}{\partial \phi} =&(\sin(\phi)\sin(\kappa)(\cos(\theta)\cos(\alpha)+\sin(\nu)\sin(\alpha)\sin(\theta))-\sin(\omega)\cos(\phi)\sin(\kappa)(-\sin(\theta)\cos(\alpha)+\sin(\nu)\sin(\alpha)\cos(\theta))+\\&\cos(\omega)\cos(\phi)\sin(\kappa)\cos(\nu)\sin(\alpha))(X_{obj}-r\ \cos(\alpha)\cos(\theta))+\\&(\sin(\phi)\sin(\kappa)\sin(\theta)\cos(\nu)-\sin(\omega)\cos(\phi)\sin(\kappa)\cos(\theta)\cos(\nu)-\cos(\omega)\cos(\phi)\sin(\kappa)\sin(\nu))(Y_{obj}-r\ \sin(\theta))+\\&(\sin(\phi)\sin(\kappa)(-\cos(\theta)\sin(\alpha)+\sin(\theta)\sin(\nu)\cos(\alpha))-\sin(\omega)\cos(\phi)\sin(\kappa)(\sin(\theta)\sin(\alpha)+\cos(\theta)\sin(\nu)\cos(\alpha))+\\&\cos(\omega)\cos(\phi)\sin(\kappa)\cos(\nu)\cos(\alpha))(Z_{obj}+r\ \sin(\alpha)\cos(\theta))\end{aligned}$$

$$\begin{aligned}\frac{\partial N}{\partial \phi} =&(\cos(\phi)(\cos(\theta)\cos(\alpha)+\sin(\nu)\sin(\alpha)\sin(\theta))+\sin(\omega)\sin(\phi)(-\sin(\theta)\cos(\alpha)+\sin(\nu)\sin(\alpha)\cos(\theta))-\\&\cos(\omega)\sin(\phi)\cos(\nu)\sin(\alpha))(X_{obj}-r\ \cos(\alpha)\cos(\theta))+\\&(\cos(\phi)\sin(\theta)\cos(\nu)+\sin(\omega)\sin(\phi)\cos(\theta)\cos(\nu)+\cos(\omega)\sin(\phi)\sin(\nu))(Y_{obj}-r\ \sin(\theta))+\\&(\cos(\phi)(-\cos(\theta)\sin(\alpha)+\sin(\theta)\sin(\nu)\cos(\alpha))+\sin(\omega)\sin(\phi)(\sin(\theta)\sin(\alpha)+\cos(\theta)\sin(\nu)\cos(\alpha))-\\&\cos(\omega)\sin(\phi)\cos(\nu)\cos(\alpha))(Z_{obj}+r\ \sin(\alpha)\cos(\theta))\end{aligned}$$

## Partial Derivates with respect to $\kappa$

$$
\begin{aligned}
\frac{\partial Zx}{\partial \kappa} =& (-\cos(\phi)\sin(\kappa)(\cos(\theta)\cos(\alpha)+\sin(\nu)\sin(\alpha)\sin(\theta))+(-\sin(\omega)\sin(\phi)\sin(\kappa)+\cos(\omega)\cos(\kappa)) \\
& (-\sin(\theta)\cos(\alpha)+\sin(\nu)\sin(\alpha)\cos(\theta))+(\cos(\omega)\sin(\phi)\sin(\kappa)+\sin(\omega)\cos(\kappa))\cos(\nu)\sin(\alpha))(X_{obj}-r\ \cos(\alpha)\cos(\theta))+ \\
& (-\cos(\phi)\sin(\kappa)\sin(\theta)\cos(\nu)+(-\sin(\omega)\sin(\phi)\sin(\kappa)+\cos(\omega)\cos(\kappa))\cos(\theta)\cos(\nu)- \\
& (\cos(\omega)\sin(\phi)\sin(\kappa)+\sin(\omega)\cos(\kappa))\sin(\nu))(\ Y_{obj}-r\ \sin(\theta))+ \\
& (-\cos(\phi)\sin(\kappa)(-\cos(\theta)\sin(\alpha)+\sin(\theta)\sin(\nu)\cos(\alpha))+(-\sin(\omega)\sin(\phi)\sin(\kappa)+\cos(\omega)\cos(\kappa)) \\
& (\sin(\theta)\sin(\alpha)+\cos(\theta)\sin(\nu)\cos(\alpha))+(\cos(\omega)\sin(\phi)\sin(\kappa)+\sin(\omega)\cos(\kappa))\cos(\nu)\cos(\alpha))(Z_{obj}+r\ \sin(\alpha)\cos(\theta))
\end{aligned}
$$

$$
\begin{aligned}
\frac{\partial Zy}{\partial \kappa} =& (-\cos(\phi)\cos(\kappa)(\cos(\theta)\cos(\alpha)+\sin(\nu)\sin(\alpha)\sin(\theta))+(-\sin(\omega)\sin(\phi)\cos(\kappa)-\cos(\omega)\sin(\kappa)) \\
& (-\sin(\theta)\cos(\alpha)+\sin(\nu)\sin(\alpha)\cos(\theta))+(\cos(\omega)\sin(\phi)\cos(\kappa)-\sin(\omega)\sin(\kappa))\cos(\nu)\sin(\alpha))(X_{obj}-r\ \cos(\alpha)\cos(\theta))+ \\
& (-\cos(\phi)\cos(\kappa)\sin(\theta)\cos(\nu)+(-\sin(\omega)\sin(\phi)\cos(\kappa)-\cos(\omega)\sin(\kappa))\cos(\theta)\cos(\nu)- \\
& (\cos(\omega)\sin(\phi)\cos(\kappa)-\sin(\omega)\sin(\kappa))\sin(\nu))(\ Y_{obj}-r\ \sin(\theta))+ \\
& (-\cos(\phi)\cos(\kappa)(-\cos(\theta)\sin(\alpha)+\sin(\theta)\sin(\nu)\cos(\alpha))+(-\sin(\omega)\sin(\phi)\cos(\kappa)-\cos(\omega)\sin(\kappa)) \\
& (\sin(\theta)\sin(\alpha)+\cos(\theta)\sin(\nu)\cos(\alpha))+(\cos(\omega)\sin(\phi)\cos(\kappa)-\sin(\omega)\sin(\kappa))\cos(\nu)\cos(\alpha))(Z_{obj}+r\ \sin(\alpha)\cos(\theta))
\end{aligned}
$$

$$
\frac{\partial N}{\partial \kappa} = 0
$$

## Partial Derivates with respect to radius $r$

$$\frac{\partial Zx}{\partial r} = -(\cos(\phi)\cos(\kappa)(\cos(\theta)\cos(\alpha)+\sin(\nu)\sin(\alpha)\sin(\theta))+(\sin(\omega)\sin(\phi)\cos(\kappa)+\cos(\omega)\sin(\kappa))$$
$$(-\sin(\theta)\cos(\alpha)+\sin(\nu)\sin(\alpha)\cos(\theta))+(-\cos(\omega)\sin(\phi)\cos(\kappa)+\sin(\omega)\sin(\kappa))\cos(\nu)\sin(\alpha))\cos(\theta)\cos(\alpha)-$$
$$(\cos(\phi)\cos(\kappa)\sin(\theta)\cos(\nu)+(\sin(\omega)\sin(\phi)\cos(\kappa)+\cos(\omega)\sin(\kappa))\cos(\theta)\cos(\nu)-$$
$$(-\cos(\omega)\sin(\phi)\cos(\kappa)+\sin(\omega)\sin(\kappa))\sin(\nu))\sin(\theta)+(\cos(\phi)\cos(\kappa)(-\cos(\theta)\sin(\alpha)+\sin(\theta)\sin(\nu)\cos(\alpha))+$$
$$(\sin(\omega)\sin(\phi)\cos(\kappa)+\cos(\omega)\sin(\kappa))(\sin(\theta)\sin(\alpha)+\cos(\theta)\sin(\nu)\cos(\alpha))+$$
$$(-\cos(\omega)\sin(\phi)\cos(\kappa)+\sin(\omega)\sin(\kappa))\cos(\nu)\cos(\alpha))\cos(\theta)\sin(\alpha)$$

$$\frac{\partial Zy}{\partial r} = -(-\cos(\phi)\sin(\kappa)(\cos(\theta)\cos(\alpha)+\sin(\nu)\sin(\alpha)\sin(\theta))+(-\sin(\omega)\sin(\phi)\sin(\kappa)+\cos(\omega)\cos(\kappa))$$
$$(-\sin(\theta)\cos(\alpha)+\sin(\nu)\sin(\alpha)\cos(\theta))+(\cos(\omega)\sin(\phi)\sin(\kappa)+\sin(\omega)\cos(\kappa))\cos(\nu)\sin(\alpha))\cos(\theta)\cos(\alpha)-$$
$$(-\cos(\phi)\sin(\kappa)\sin(\theta)\cos(\nu)+(-\sin(\omega)\sin(\phi)\sin(\kappa)+\cos(\omega)\cos(\kappa))\cos(\theta)\cos(\nu)-$$
$$(\cos(\omega)\sin(\phi)\sin(\kappa)+\sin(\omega)\cos(\kappa))\sin(\nu))\sin(\theta)+(-\cos(\phi)\sin(\kappa)(-\cos(\theta)\sin(\alpha)+\sin(\theta)\sin(\nu)\cos(\alpha))+$$
$$(-\sin(\omega)\sin(\phi)\sin(\kappa)+\cos(\omega)\cos(\kappa))(\sin(\theta)\sin(\alpha)+\cos(\theta)\sin(\nu)\cos(\alpha))+$$
$$(\cos(\omega)\sin(\phi)\sin(\kappa)+\sin(\omega)\cos(\kappa))\cos(\nu)\cos(\alpha))\cos(\theta)\sin(\alpha)$$

$$\frac{\partial N}{\partial r} = -(\sin(\phi)(\cos(\theta)\cos(\alpha)+\sin(\nu)\sin(\alpha)\sin(\theta))-\sin(\omega)\cos(\phi)(-\sin(\theta)\cos(\alpha)+\sin(\nu)\sin(\alpha)\cos(\theta))+$$
$$\cos(\omega)\cos(\phi)\cos(\nu)\sin(\alpha))\cos(\theta)\cos(\alpha)-(\sin(\phi)\sin(\theta)\cos(\nu)-\sin(\omega)\cos(\phi)\cos(\theta)\cos(\nu)-\cos(\omega)\cos(\phi)\sin(\nu))\sin(\theta)+$$
$$(\sin(\phi)(-\cos(\theta)\sin(\alpha)+\sin(\theta)\sin(\nu)\cos(\alpha))-\sin(\omega)\cos(\phi)(\sin(\theta)\sin(\alpha)+\cos(\theta)\sin(\nu)\cos(\alpha))+$$
$$\cos(\omega)\cos(\phi)\cos(\nu)\cos(\alpha))\cos(\theta)\sin(\alpha)$$

## Partial Derivates with respect to $\alpha$

$$
\begin{aligned}
\frac{\partial Zx}{\partial \alpha} =& (\cos(\phi)\cos(\kappa)(-\cos(\theta)\sin(\alpha)+\sin(\theta)\sin(\nu)\cos(\alpha))+(\sin(\omega)\sin(\phi)\cos(\kappa)+\cos(\omega)\sin(\kappa)) \\
& (\sin(\theta)\sin(\alpha)+\cos(\theta)\sin(\nu)\cos(\alpha))+(-\cos(\omega)\sin(\phi)\cos(\kappa)+\sin(\omega)\sin(\kappa))\cos(\nu)\cos(\alpha))(X_{obj}-r\ \cos(\alpha)\cos(\theta))+ \\
& (\cos(\phi)\cos(\kappa)(\cos(\theta)\cos(\alpha)+\sin(\nu)\sin(\alpha)\sin(\theta))+(\sin(\omega)\sin(\phi)\cos(\kappa)+\cos(\omega)\sin(\kappa)) \\
& (-\sin(\theta)\cos(\alpha)+\sin(\nu)\sin(\alpha)\cos(\theta))+(-\cos(\omega)\sin(\phi)\cos(\kappa)+\sin(\omega)\sin(\kappa))\cos(\nu)\sin(\alpha))r\ \sin(\alpha)\cos(\theta)+ \\
& (\cos(\phi)\cos(\kappa)(-\cos(\theta)\cos(\alpha)-\sin(\nu)\sin(\alpha)\sin(\theta))+(\sin(\omega)\sin(\phi)\cos(\kappa)+\cos(\omega)\sin(\kappa)) \\
& (\sin(\theta)\cos(\alpha)-\sin(\nu)\sin(\alpha)\cos(\theta))-(-\cos(\omega)\sin(\phi)\cos(\kappa)+\sin(\omega)\sin(\kappa))\cos(\nu)\sin(\alpha))(Z_{obj}+r\ \sin(\alpha)\cos(\theta))+ \\
& (\cos(\phi)\cos(\kappa)(-\cos(\theta)\sin(\alpha)+\sin(\theta)\sin(\nu)\cos(\alpha))+(\sin(\omega)\sin(\phi)\cos(\kappa)+\cos(\omega)\sin(\kappa)) \\
& (\sin(\theta)\sin(\alpha)+\cos(\theta)\sin(\nu)\cos(\alpha))+(-\cos(\omega)\sin(\phi)\cos(\kappa)+\sin(\omega)\sin(\kappa))\cos(\nu)\cos(\alpha))r\ \cos(\alpha)\cos(\theta)
\end{aligned}
$$

$$
\begin{aligned}
\frac{\partial Zy}{\partial \alpha} =& (-\cos(\phi)\sin(\kappa)(-\cos(\theta)\sin(\alpha)+\sin(\theta)\sin(\nu)\cos(\alpha))+(-\sin(\omega)\sin(\phi)\sin(\kappa)+\cos(\omega)\cos(\kappa)) \\
& (\sin(\theta)\sin(\alpha)+\cos(\theta)\sin(\nu)\cos(\alpha))+(\cos(\omega)\sin(\phi)\sin(\kappa)+\sin(\omega)\cos(\kappa))\cos(\nu)\cos(\alpha))(X_{obj}-r\ \cos(\alpha)\cos(\theta))+ \\
& (-\cos(\phi)\sin(\kappa)(\cos(\theta)\cos(\alpha)+\sin(\nu)\sin(\alpha)\sin(\theta))+(-\sin(\omega)\sin(\phi)\sin(\kappa)+\cos(\omega)\cos(\kappa)) \\
& (-\sin(\theta)\cos(\alpha)+\sin(\nu)\sin(\alpha)\cos(\theta))+(\cos(\omega)\sin(\phi)\sin(\kappa)+\sin(\omega)\cos(\kappa))\cos(\nu)\sin(\alpha))r\ \sin(\alpha)\cos(\theta)+ \\
& (-\cos(\phi)\sin(\kappa)(-\cos(\theta)\cos(\alpha)-\sin(\nu)\sin(\alpha)\sin(\theta))+(-\sin(\omega)\sin(\phi)\sin(\kappa)+\cos(\omega)\cos(\kappa)) \\
& (\sin(\theta)\cos(\alpha)-\sin(\nu)\sin(\alpha)\cos(\theta))-(\cos(\omega)\sin(\phi)\sin(\kappa)+\sin(\omega)\cos(\kappa))\cos(\nu)\sin(\alpha))(Z_{obj}+r\ \sin(\alpha)\cos(\theta))+ \\
& (-\cos(\phi)\sin(\kappa)(-\cos(\theta)\sin(\alpha)+\sin(\theta)\sin(\nu)\cos(\alpha))+(-\sin(\omega)\sin(\phi)\sin(\kappa)+\cos(\omega)\cos(\kappa)) \\
& (\sin(\theta)\sin(\alpha)+\cos(\theta)\sin(\nu)\cos(\alpha))+(\cos(\omega)\sin(\phi)\sin(\kappa)+\sin(\omega)\cos(\kappa))\cos(\nu)\cos(\alpha))r\ \cos(\alpha)\cos(\theta)
\end{aligned}
$$

$$
\begin{aligned}
\frac{\partial N}{\partial \alpha} =& (\sin(\phi)(-\cos(\theta)\sin(\alpha) + \sin(\theta)\sin(\nu)\cos(\alpha)) - \sin(\omega)\cos(\phi)(\sin(\theta)\sin(\alpha) + \cos(\theta)\sin(\nu)\cos(\alpha)) \\
& + \cos(\omega)\cos(\phi)\cos(\nu)\cos(\alpha))(X_{obj} - r\ \cos(\alpha)\cos(\theta)) + \\
& (\sin(\phi)(\cos(\theta)\cos(\alpha) + \sin(\nu)\sin(\alpha)\sin(\theta)) - \sin(\omega)\cos(\phi)(-\sin(\theta)\cos(\alpha) + \sin(\nu)\sin(\alpha)\cos(\theta)) + \\
& \cos(\omega)\cos(\phi)\cos(\nu)\sin(\alpha))r\ \sin(\alpha)\cos(\theta) + \\
& (\sin(\phi)(-\cos(\theta)\cos(\alpha) - \sin(\nu)\sin(\alpha)\sin(\theta)) - \sin(\omega)\cos(\phi)(\sin(\theta)\cos(\alpha) - \sin(\nu)\sin(\alpha)\cos(\theta)) - \\
& \cos(\omega)\cos(\phi)\cos(\nu)\sin(\alpha))(Z_{obj} + r\ \sin(\alpha)\cos(\theta)) + \\
& (\sin(\phi)(-\cos(\theta)\sin(\alpha) + \sin(\theta)\sin(\nu)\cos(\alpha)) - \sin(\omega)\cos(\phi)(\sin(\theta)\sin(\alpha) + \cos(\theta)\sin(\nu)\cos(\alpha)) + \\
& \cos(\omega)\cos(\phi)\cos(\nu)\cos(\alpha))r\ \cos(\alpha)\cos(\theta)
\end{aligned}
$$

## Partial Derivates with respect to $\theta$

$$
\begin{aligned}
\frac{\partial Zx}{\partial \theta} =&(\cos(\phi)\cos(\kappa)(-\sin(\theta)\cos(\alpha)+\sin(\nu)\sin(\alpha)\cos(\theta))+(\sin(\omega)\sin(\phi)\cos(\kappa)+\cos(\omega)\sin(\kappa))\\
&(-\cos(\theta)\cos(\alpha)-\sin(\nu)\sin(\alpha)\sin(\theta)))(X_{obj}-r\ \cos(\alpha)\cos(\theta))+\\
&(\cos(\phi)\cos(\kappa)(\cos(\theta)\cos(\alpha)+\sin(\nu)\sin(\alpha)\sin(\theta))+(\sin(\omega)\sin(\phi)\cos(\kappa)+\cos(\omega)\sin(\kappa))\\
&(-\sin(\theta)\cos(\alpha)+\sin(\nu)\sin(\alpha)\cos(\theta))+(-\cos(\omega)\sin(\phi)\cos(\kappa)+\sin(\omega)\sin(\kappa))\cos(\nu)\sin(\alpha))r\ \cos(\alpha)\sin(\theta)+\\
&(\cos(\phi)\cos(\kappa)\cos(\theta)\cos(\nu)-(\sin(\omega)\sin(\phi)\cos(\kappa)+\cos(\omega)\sin(\kappa))\sin(\theta)\cos(\nu))(Y_{obj}-r\ \sin(\theta))-\\
&(\cos(\phi)\cos(\kappa)\sin(\theta)\cos(\nu)+(\sin(\omega)\sin(\phi)\cos(\kappa)+\cos(\omega)\sin(\kappa))\cos(\theta)\cos(\nu)-\\
&(-\cos(\omega)\sin(\phi)\cos(\kappa)+\sin(\omega)\sin(\kappa))\sin(\nu))r\ \cos(\theta)+(\cos(\phi)\cos(\kappa)(\sin(\theta)\sin(\alpha)+\cos(\theta)\sin(\nu)\cos(\alpha))+\\
&(\sin(\omega)\sin(\phi)\cos(\kappa)+\cos(\omega)\sin(\kappa))(\cos(\theta)\sin(\alpha)-\sin(\theta)\sin(\nu)\cos(\alpha)))(Z_{obj}+r\ \sin(\alpha)\cos(\theta))-\\
&(\cos(\phi)\cos(\kappa)(-\cos(\theta)\sin(\alpha)+\sin(\theta)\sin(\nu)\cos(\alpha))+(\sin(\omega)\sin(\phi)\cos(\kappa)+\\
&\cos(\omega)\sin(\kappa))(\sin(\theta)\sin(\alpha)+\cos(\theta)\sin(\nu)\cos(\alpha))+(-\cos(\omega)\sin(\phi)\cos(\kappa)+\sin(\omega)\sin(\kappa))\cos(\nu)\cos(\alpha))r\ \sin(\alpha)\sin(\theta)\\
\frac{\partial Zy}{\partial \theta} =&(-\cos(\phi)\sin(\kappa)(-\sin(\theta)\cos(\alpha)+\sin(\nu)\sin(\alpha)\cos(\theta))+(-\sin(\omega)\sin(\phi)\sin(\kappa)+\cos(\omega)\cos(\kappa))\\
&(-\cos(\theta)\cos(\alpha)-\sin(\nu)\sin(\alpha)\sin(\theta)))(X_{obj}-r\ \cos(\alpha)\cos(\theta))+\\
&(-\cos(\phi)\sin(\kappa)(\cos(\theta)\cos(\alpha)+\sin(\nu)\sin(\alpha)\sin(\theta))+(-\sin(\omega)\sin(\phi)\sin(\kappa)+\cos(\omega)\cos(\kappa))\\
&(-\sin(\theta)\cos(\alpha)+\sin(\nu)\sin(\alpha)\cos(\theta))+(\cos(\omega)\sin(\phi)\sin(\kappa)+\sin(\omega)\cos(\kappa))\cos(\nu)\sin(\alpha))r\ \cos(\alpha)\sin(\theta)+\\
&(-\cos(\phi)\sin(\kappa)\cos(\theta)\cos(\nu)-(-\sin(\omega)\sin(\phi)\sin(\kappa)+\cos(\omega)\cos(\kappa))\sin(\theta)\cos(\nu))(Y_{obj}-r\ \sin(\theta))-\\
&(-\cos(\phi)\sin(\kappa)\sin(\theta)\cos(\nu)+(-\sin(\omega)\sin(\phi)\sin(\kappa)+\cos(\omega)\cos(\kappa))\cos(\theta)\cos(\nu)-\\
&(\cos(\omega)\sin(\phi)\sin(\kappa)+\sin(\omega)\cos(\kappa))\sin(\nu))r\ \cos(\theta)+(-\cos(\phi)\sin(\kappa)(\sin(\theta)\sin(\alpha)+\cos(\theta)\sin(\nu)\cos(\alpha))+\\
&(-\sin(\omega)\sin(\phi)\sin(\kappa)+\cos(\omega)\cos(\kappa))(\cos(\theta)\sin(\alpha)-\sin(\theta)\sin(\nu)\cos(\alpha)))(Z_{obj}+r\ \sin(\alpha)\cos(\theta))-\\
&(-\cos(\phi)\sin(\kappa)(-\cos(\theta)\sin(\alpha)+\sin(\theta)\sin(\nu)\cos(\alpha))+(-\sin(\omega)\sin(\phi)\sin(\kappa)+\\
&\cos(\omega)\cos(\kappa))(\sin(\theta)\sin(\alpha)+\cos(\theta)\sin(\nu)\cos(\alpha))+(\cos(\omega)\sin(\phi)\sin(\kappa)+\sin(\omega)\cos(\kappa))\cos(\nu)\cos(\alpha))r\ \sin(\alpha)\sin(\theta)
\end{aligned}
$$

$$
\begin{aligned}
\frac{\partial N}{\partial \theta} =& (\sin(\phi)(-\sin(\theta)\cos(\alpha) + \sin(\nu)\sin(\alpha)\cos(\theta)) - \\
& \sin(\omega)\cos(\phi)(-\cos(\theta)\cos(\alpha) - \sin(\nu)\sin(\alpha)\sin(\theta)))(X_{obj} - r\ \cos(\alpha)\cos(\theta)) + \\
& (\sin(\phi)(\cos(\theta)\cos(\alpha) + \sin(\nu)\sin(\alpha)\sin(\theta)) - \sin(\omega)\cos(\phi)(-\sin(\theta)\cos(\alpha) + \sin(\nu)\sin(\alpha)\cos(\theta)) + \\
& \cos(\omega)\cos(\phi)\cos(\nu)\sin(\alpha))r\ \cos(\alpha)\sin(\theta) + (\sin(\phi)\cos(\theta)\cos(\nu) + \sin(\omega)\cos(\phi)\sin(\theta)\cos(\nu))(Y_{obj} - r\ \sin(\theta)) - \\
& (\sin(\phi)\sin(\theta)\cos(\nu) - \sin(\omega)\cos(\phi)\cos(\theta)\cos(\nu) - \cos(\omega)\cos(\phi)\sin(\nu))r\ \cos(\theta) + \\
& (\sin(\phi)(\sin(\theta)\sin(\alpha) + \cos(\theta)\sin(\nu)\cos(\alpha)) - \sin(\omega)\cos(\phi)(\cos(\theta)\sin(\alpha) - \sin(\theta)\sin(\nu)\cos(\alpha)))(Z_{obj} + r\ \sin(\alpha)\cos(\theta)) - \\
& (\sin(\phi)(-\cos(\theta)\sin(\alpha) + \sin(\theta)\sin(\nu)\cos(\alpha)) - \sin(\omega)\cos(\phi)(\sin(\theta)\sin(\alpha) + \cos(\theta)\sin(\nu)\cos(\alpha)) + \\
& \cos(\omega)\cos(\phi)\cos(\nu)\cos(\alpha))r\ \sin(\alpha)\sin(\theta)
\end{aligned}
$$

## Partial Derivates with respect to $\nu$

$$\begin{aligned}\frac{\partial Zx}{\partial \nu} =&(\cos(\phi)\cos(\kappa)\cos(\nu)\sin(\alpha)\sin(\theta) + (\sin(\omega)\sin(\phi)\cos(\kappa) + \cos(\omega)\sin(\kappa))\cos(\nu)\sin(\alpha)\cos(\theta) - \\ &(-\cos(\omega)\sin(\phi)\cos(\kappa) + \sin(\omega)\sin(\kappa))\sin(\nu)\sin(\alpha))(X_{obj} - r\ \cos(\alpha)\cos(\theta)) + \\ &(-\cos(\phi)\cos(\kappa)\sin(\theta)\sin(\nu) - (\sin(\omega)\sin(\phi)\cos(\kappa) + \cos(\omega)\sin(\kappa))\cos(\theta)\sin(\nu) - \\ &(-\cos(\omega)\sin(\phi)\cos(\kappa) + \sin(\omega)\sin(\kappa))\cos(\nu))(Y_{obj} - r\ \sin(\theta)) + \\ &(\cos(\phi)\cos(\kappa)\sin(\theta)\cos(\nu)\cos(\alpha) + (\sin(\omega)\sin(\phi)\cos(\kappa) + \cos(\omega)\sin(\kappa))\cos(\theta)\cos(\nu)\cos(\alpha) - \\ &(-\cos(\omega)\sin(\phi)\cos(\kappa) + \sin(\omega)\sin(\kappa))\sin(\nu)\cos(\alpha))(Z_{obj} + r\ \sin(\alpha)\cos(\theta))\end{aligned}$$

$$\begin{aligned}\frac{\partial Zy}{\partial \nu} =&(-\cos(\phi)\sin(\kappa)\cos(\nu)\sin(\alpha)\sin(\theta) + (-\sin(\omega)\sin(\phi)\sin(\kappa) + \cos(\omega)\cos(\kappa))\cos(\nu)\sin(\alpha)\cos(\theta) - \\ &(\cos(\omega)\sin(\phi)\sin(\kappa) + \sin(\omega)\cos(\kappa))\sin(\nu)\sin(\alpha))(X_{obj} - r\ \cos(\alpha)\cos(\theta)) + \\ &(\cos(\phi)\sin(\kappa)\sin(\theta)\sin(\nu) - (-\sin(\omega)\sin(\phi)\sin(\kappa) + \cos(\omega)\cos(\kappa))\cos(\theta)\sin(\nu) - \\ &(\cos(\omega)\sin(\phi)\sin(\kappa) + \sin(\omega)\cos(\kappa))\cos(\nu))(Y_{obj} - r\ \sin(\theta)) + \\ &(-\cos(\phi)\sin(\kappa)\sin(\theta)\cos(\nu)\cos(\alpha) + (-\sin(\omega)\sin(\phi)\sin(\kappa) + \cos(\omega)\cos(\kappa))\cos(\theta)\cos(\nu)\cos(\alpha) - \\ &(\cos(\omega)\sin(\phi)\sin(\kappa) + \sin(\omega)\cos(\kappa))\sin(\nu)\cos(\alpha))(Z_{obj} + r\ \sin(\alpha)\cos(\theta))\end{aligned}$$

$$\begin{aligned}\frac{\partial N}{\partial \nu} =&(\sin(\phi)\cos(\nu)\sin(\alpha)\sin(\theta) - \sin(\omega)\cos(\phi)\cos(\nu)\sin(\alpha)\cos(\theta) - \cos(\omega)\cos(\phi)\sin(\nu)\sin(\alpha))(X_{obj} - r\ \cos(\alpha)\cos(\theta)) + \\ &(-\sin(\phi)\sin(\theta)\sin(\nu) + \sin(\omega)\cos(\phi)\cos(\theta)\sin(\nu) - \cos(\omega)\cos(\phi)\cos(\nu))(Y_{obj} - r\ \sin(\theta)) + \\ &(\sin(\phi)\sin(\theta)\cos(\nu)\cos(\alpha) - \sin(\omega)\cos(\phi)\cos(\theta)\cos(\nu)\cos(\alpha) - \cos(\omega)\cos(\phi)\sin(\nu)\cos(\alpha))(Z_{obj} + r\ \sin(\alpha)\cos(\theta))\end{aligned}$$

## Rotation matrix $R_{\omega,\phi,\kappa}$

$$
\begin{aligned}
r_{00} &= \cos(\phi)\cos(\kappa) \\
r_{01} &= \sin(\omega)\sin(\phi)\cos(\kappa) + \cos(\omega)\sin(\kappa) \\
r_{02} &= -\cos(\omega)\sin(\phi)\cos(\kappa) + \sin(\omega)\sin(\kappa) \\
r_{10} &= -\cos(\phi)\sin(\kappa) \\
r_{11} &= -\sin(\omega)\sin(\phi)\sin(\kappa) + \cos(\omega)\cos(\kappa) \\
r_{12} &= \cos(\omega)\sin(\phi)\sin(\kappa) + \sin(\omega)\cos(\kappa) \\
r_{20} &= \sin(\phi) \\
r_{21} &= -\sin(\omega)\cos(\phi) \\
r_{22} &= \cos(\omega)\cos(\phi)
\end{aligned}
$$

## Rotation matrix $R_{\alpha,\nu,\theta}$

$$
\begin{aligned}
a_{00} &= \cos(\theta)\cos(\alpha) + \sin(\nu)\sin(\alpha)\sin(\theta) \\
a_{01} &= \sin(\theta)\cos(\nu) \\
a_{02} &= -\cos(\theta)\sin(\alpha) + \sin(\theta)\sin(\nu)\cos(\alpha) \\
a_{10} &= -\sin(\theta)\cos(\alpha) + \sin(\nu)\sin(\alpha)\cos(\theta) \\
a_{11} &= \cos(\theta)\cos(\nu) \\
a_{12} &= \sin(\theta)\sin(\alpha) + \cos(\theta)\sin(\nu)\cos(\alpha) \\
a_{20} &= \cos(\nu)\sin(\alpha) \\
a_{21} &= -\sin(\nu) \\
a_{22} &= \cos(\nu)\cos(\alpha)
\end{aligned}
$$

## Rotation matrix $R_i = R_{\omega,\phi,\kappa} \cdot R_{\alpha,\nu,\theta}$

$$
\begin{aligned}
Ri_{00} &= \cos(\phi)\cos(\kappa)\left(\cos(\theta)\cos(\alpha) + \sin(\theta)\sin(\nu)\sin(\alpha)\right) + \left(\sin(\omega)\sin(\phi)\cos(\kappa) + \cos(\omega)\sin(\kappa)\right) \\
&\quad \left(-\sin(\theta)\cos(\alpha) + \cos(\theta)\sin(\nu)\sin(\alpha)\right) + \left(-\cos(\omega)\sin(\phi)\cos(\kappa) + \sin(\omega)\sin(\kappa)\right)\cos(\nu)\sin(\alpha) \\
Ri_{01} &= \cos(\phi)\cos(\kappa)\sin(\theta)\cos(\nu) + \left(\sin(\omega)\sin(\phi)\cos(\kappa) + \cos(\omega)\sin(\kappa)\right)\cos(\theta)\cos(\nu) - \\
&\quad \left(-\cos(\omega)\sin(\phi)\cos(\kappa) + \sin(\omega)\sin(\kappa)\right)\sin(\nu) \\
Ri_{02} &= \cos(\phi)\cos(\kappa)\left(-\cos(\theta)\sin(\alpha) + \sin(\theta)\sin(\nu)\cos(\alpha)\right) + \left(\sin(\omega)\sin(\phi)\cos(\kappa) + \cos(\omega)\sin(\kappa)\right) \\
&\quad \left(\sin(\theta)\sin(\alpha) + \cos(\theta)\sin(\nu)\cos(\alpha)\right) + \left(-\cos(\omega)\sin(\phi)\cos(\kappa) + \sin(\omega)\sin(\kappa)\right)\cos(\nu)\cos(\alpha) \\
Ri_{10} &= -\cos(\phi)\sin(\kappa)\left(\cos(\theta)\cos(\alpha) + \sin(\theta)\sin(\nu)\sin(\alpha)\right) + \left(-\sin(\omega)\sin(\phi)\sin(\kappa) + \cos(\omega)\cos(\kappa)\right) \\
&\quad \left(-\sin(\theta)\cos(\alpha) + \cos(\theta)\sin(\nu)\sin(\alpha)\right) + \left(\cos(\omega)\sin(\phi)\sin(\kappa) + \sin(\omega)\cos(\kappa)\right)\cos(\nu)\sin(\alpha) \\
Ri_{11} &= -\cos(\phi)\sin(\kappa)\sin(\theta)\cos(\nu) + \left(-\sin(\omega)\sin(\phi)\sin(\kappa) + \cos(\omega)\cos(\kappa)\right)\cos(\theta)\cos(\nu) - \\
&\quad \left(\cos(\omega)\sin(\phi)\sin(\kappa) + \sin(\omega)\cos(\kappa)\right)\sin(\nu) \\
Ri_{12} &= -\cos(\phi)\sin(\kappa)\left(-\cos(\theta)\sin(\alpha) + \sin(\theta)\sin(\nu)\cos(\alpha)\right) + \left(-\sin(\omega)\sin(\phi)\sin(\kappa) + \cos(\omega)\cos(\kappa)\right) \\
&\quad \left(\sin(\theta)\sin(\alpha) + \cos(\theta)\sin(\nu)\cos(\alpha)\right) + \left(\cos(\omega)\sin(\phi)\sin(\kappa) + \sin(\omega)\cos(\kappa)\right)\cos(\nu)\cos(\alpha) \\
Ri_{20} &= \sin(\phi)\left(\cos(\theta)\cos(\alpha) + \sin(\theta)\sin(\nu)\sin(\alpha)\right) - \sin(\omega)\cos(\phi)\left(-\sin(\theta)\cos(\alpha) + \cos(\theta)\sin(\nu)\sin(\alpha)\right) + \\
&\quad \cos(\omega)\cos(\phi)\cos(\nu)\sin(\alpha) \\
Ri_{21} &= \sin(\phi)\sin(\theta)\cos(\nu) - \sin(\omega)\cos(\phi)\cos(\theta)\cos(\nu) - \cos(\omega)\cos(\phi)\sin(\nu) \\
Ri_{22} &= \sin(\phi)\left(-\cos(\theta)\sin(\alpha) + \sin(\theta)\sin(\nu)\cos(\alpha)\right) - \sin(\omega)\cos(\phi)\left(\sin(\theta)\sin(\alpha) + \cos(\theta)\sin(\nu)\cos(\alpha)\right) + \\
&\quad \cos(\omega)\cos(\phi)\cos(\nu)\cos(\alpha)
\end{aligned}
$$